ACARP

ACARP Project C17029

Towards 3D, Integrated P+PS Seismic Imaging of Coal Targets

Final Report
June 2011

Shaun Strong
Steve Hearn

Velseis Pty Ltd
ABN 56 009 809 544

83 Jijaws Street (PO Box 118),
Sumner Park,
Queensland 4074

Ph: (617) 3376 5544
Fax: (617) 3376 6939
Email: velseis@velseis.com.au

Velseis

Integrated Seismic Technologies

DISCLAIMER

No person, corporation or other organisation (“person”) should rely on the contents of this report and each should obtain independent advice from a qualified person with respect to the information contained in this report. Australian Coal Research Limited, its directors, servants and agents (collectively “ACR”) is not responsible for the consequences of any action taken by any person in reliance upon the information set out in this report, for the accuracy or veracity of any information contained in this report or for any error or omission in this report. ACR expressly disclaims any and all liability and responsibility to any person in respect of anything done or omitted to be done in respect of the information set out in this report, any inaccuracy in this report or the consequences of any action by any person in reliance, whether wholly or partly, upon the whole or any part of the contents of this report.

Executive Summary

Compressional-wave (P-wave) seismic reflection is a valuable tool used throughout the coal industry, for exploration (mainly 2D reflection) and mine planning (3D). Shear-wave (S-wave) reflection presents interesting theoretical potential, but is more difficult to implement. Previous ACARP projects (C10020, C13029) have successfully demonstrated the 2D implementation of converted-wave (PS-wave) reflection at the coal scale. Those projects demonstrate that a more complete geological interpretation can be obtained by integrated interpretation of the P-wave and PS-wave information.

A full 3D implementation of PS reflection is highly desirable, but presents additional challenges, including the anticipated problem of azimuthal variation in the transmission properties of PS-waves. This ACARP project (C17029) examines the feasibility and potential of integrated 3D P+PS reflection at the coal scale. The project includes the first known 3D field trial of this technology in the Australian coal industry.

The PS reflection path is asymmetrical, and the horizontal reflection point varies with target depth and rock properties. Hence, ray-path modelling has been used to design the optimal layout of sources and receivers for the C17029 field trial. In addition, far-offset PS reflections from coal seams suffer greater phase distortion than standard P reflections. These phase variations can be effectively modelled using reflectivity and finite-difference modelling. Based on the expected target seam depth (70-120m) from prior 2D work, phase distortion needs to be monitored on the longest offset PS reflections. Following comprehensive survey modelling, a small, high-fold 3D grid was successfully recorded using an Envirovibe source and 3C receivers. A 20-person crew took approximately 3 days to record two full passes over the grid (using different Vibroseis sweep parameters). Total receiver line length was 9.75 km (15m intervals) and total source line length was 18.5 km (30m intervals). The 3D volume was designed to have extremely high fold (maximum > 500), to allow subdivision of the data for azimuth-limited analysis. The field trial proceeded very efficiently. As expected the raw horizontal-component data (from which the PS images are obtained) were relatively noisy compared to the standard P-wave recordings.

The processing of the 3D-PS volume has required considerable effort, and the implementation of various 3D extensions to our existing 2D-PS software. A critical aspect is the identification of spurious time errors (statics) caused by near-surface geological variations. These effects are most

obvious where the reflected S-wave reaches the surface near the receiver. Comparison of the P and PS data demonstrates that failure to account for such near-surface anomalies can result in serious misinterpretation of true geology at depth. Four different statics algorithms have been trialled, and our preference is for a solution based on the analysis of PPS refraction data. This is an S-wave extension of the popular refraction-statics algorithm used in standard processing.

We have demonstrated that a viable PS-wave volume can be obtained, and have extracted a set of target attributes from this volume. We have shown that an enhanced structural interpretation is obtained by integrating the P and PS volumes. The high fold of the volume has permitted a detailed investigation of apparent azimuthal variations in wave behaviour. Although we are still wary of static contamination, we believe that the PS volume exhibits significant evidence for azimuthal anisotropy. There is some evidence that the variation of the S-wave velocity with azimuth may relate to geology. These effects seem more pronounced in the vicinity of the faulted zone.

This project has defined a number of core technical problems which demand more robust solutions, and we have identified specific avenues for ongoing research to address these problems. Nevertheless, the project has clearly indicated the significant potential of integrated 3D P+PS seismic reflection as an emerging tool for the coal industry.

Acknowledgements

Velseis Pty Ltd would like to acknowledge the following organisations for their support of this research:

- Australian Coal Association Research Program (ACARP)
- Xstrata Coal Australia Pty Ltd
- Anglo Coal Australia Pty Ltd
- Bowen Basin Geologists Group (BBGG)

Thanks must also go to the ACARP industry mentors – Todd Harrington and Andrea Rutley (Xstrata) and Andrew Willson (Anglo Coal) for their support of this project. Thanks also to Keith Smith of ACARP for his professional supervision of the project.

Velseis also acknowledges the Centre for Wave Phenomena, Colorado School of Mines for the development and distribution of Seismic Unix – an open source research and seismic processing package. Much of our code is developed around the framework provided by Seismic Unix.

The authors wish to sincerely thank the many Velseis staff members who have contributed to the success of this project.

Table of Contents

List of Figures

List of Tables

1 Introduction

1.1 Introduction

Over the past three decades, coal seismic reflection has evolved from an experimental concept to an essential industry tool. Initially, coal reflection was run along 2D lines, often during the exploration phase of a project. Driven by the reality that geology is three dimensional, coal reflection technology has evolved into a full 3D technique, yielding a detailed 3D image of subsurface structures. This is now seen as a cost-effective tool for coal mine planning.

Almost all of the production coal seismic surveys run in the past 3 decades have utilised P-waves, because these waves are easy to generate and record. As part of the natural drive to improve seismic technologies, two recent ACARP projects (C10020, C13029) have explored a novel extension, referred to as PS (or converted-wave) seismic reflection. This concept has the potential to take advantage of the unique properties of S-waves, although practical implementation of PS reflection is non-trivial. The previous ACARP projects have demonstrated that PS coal seismic reflection can be successfully applied in a 2D mode. Following the historical development of P-wave seismology, it is natural to seek to extend PS technology to allow full 3D imaging of coal environments. The present project explores this possibility.

Since its invention in 1923, seismic reflection has been vigorously researched, with much of the impetus coming from the petroleum industry. The scale of the coal-seismic problem is quite different, and this necessitates a different technical approach. In the following section we provide a summary of developments in the seismic method which have led to this attempt to apply 3D-PS recording in the coal industry. The aims of this review are to clarify the relationships between the different modes of seismic recording applied to petroleum and coal-scale seismology, and to give a broad perspective to the technical significance of the current project.

1.2 Technical Background to the Project

1.2.1 Seismic Reflection and Seismic Wave Types

The seismic method relies on reflection of sound waves from any subsurface interface which provides a contrast in acoustic impedance (the product of density and seismic velocity).

Fortuitously, coal exhibits extremely low density and velocity, meaning that it presents an excellent contrast for seismic reflection. The method is now an essential tool in the coal industry, used for both exploration for new deposits, and in mine-planning and exploitation.

The typical approach utilises a source at or near the surface, and a series of sensors (geophones) positioned on the surface nearby. There are a number of different seismic waves that can be recorded using this technique. Compressional (P) waves and shear (S) waves, are referred to as *body waves*, since they travel down into the earth and hence have potential for imaging subsurface features. In addition, various *surface waves* (Rayleigh, Love) are also recorded. In the context of reflection imagery these surface waves are considered as undesirable noise.

1.2.2 Coal-Scale P-wave Reflection in 2D and 3D

P-waves are much easier to generate and record than S-waves. Hence, throughout the petroleum and coal sectors, seismic reflection has almost exclusively used P-waves, generated and recorded at or near the surface (Figure 1.1a). The P-wave seismic reflection method became commercially viable as an exploration technique in the late 1920's (e.g. Allen, 1980). Since its inception the technology has developed significantly, driven largely by the demands of the petroleum sector. For its first 50 years, seismic reflection was applied along 2D lines. However, it was accepted that because geology is rarely 2D, reflections were also arriving from out of the plane of the seismic line. This realisation drove the development of 3D P-wave reflection, which is more able to cope with real 3D geologies.

In Australia, the use of conventional 2D seismic surveys for coal exploration was started in the late 1950s but was rare until the 1970s (Packham and Emerson, 1975; Rutter and Harman, 1979). The first Australian experimental 3D seismic surveys over coal targets were acquired in 1988 (Lambourne et al., 1989). These surveys were conducted in areas where previous 2D data had been acquired. The results indicated that 3D seismic data can provide a better interpretation of structures in coal seams, where the 2D results are ambiguous. The first production 3D coal survey was acquired for BHP at the Appin Colliery in 1997 (Hatherly et al., 1998). Useful results were demonstrated and this encouraged further surveys. Since that time the Australian Coal industry has increasingly used P-wave 3D seismic-surveying methods for exploration and planning. The major Australian coal producers now consider 3D seismic reflection as an essential and cost-effective element in mine planning.

1.2.3 The Potential of S-wave Seismic Reflection

The conventional P-wave seismic method is highly developed and has been very successful. However, theory suggests that S-waves should respond differently to subsurface variations, and hence could provide extra information about rock properties. There are several interesting theoretical differences between P-waves and S-waves.

Velocity Differences between P- and S-waves

Firstly, S-waves travel with velocities which are lower than P-waves . The velocity ratio Vp/Vs is often around 2, although much higher values can be observed in unconsolidated material near the surface. This means that provided the frequency content is similar, S-waves should exhibit shorter wavelengths, and hence better resolution, than P-waves. Unfortunately, S-waves are also more susceptible to frictional attenuation. This means that in practice the recorded frequencies are often lower than for P-waves. Recorded S-waves often do not exhibit any wavelength reduction, and hence the theoretical resolution advantage may not be realised.

The fact that S-waves travel slower than P-waves can, however, lead to a simple geometric advantage in the case of shallow targets. S-wave reflections will arrive later than P-wave reflections, and this means that they may be better separated from distorting surface noise (e.g. Rayleigh Waves). This simple geometric advantage has provided strong impetus for the application of S-waves in exploration for opencut coal targets (e.g. Velseis 2003, 2007).

Response of P- and S-waves to Fluids

P- and S-waves respond very differently to liquid hydrocarbons in rocks. P-wave velocities are reduced by the presence of gas or liquids within the earth. Hence, in certain situations, included hydrocarbons can result in reduced impedance contrasts at boundaries, and degraded P-wave imagery. On the other hand, S-waves do not travel in fluids, and hence they respond only to the lithological matrix. In the petroleum industry, a number of major fields have exploited S-wave surveys to successfully image structures where petroleum related gas clouds have degraded the P-wave image (e.g. Macleod et al, 1999; Berteussen et al, 1999; Garotta, 1999).

In fact, P-waves and S-waves have different responses not just to fluids, but to all geological units. It is then possible to determine lithological characteristics by integrated interpretation of the P-wave and S-wave imagery (Helbig and Mesdag, 1982). In the context of coal exploration, this approach has been used to estimate Poisson's ratio using integrated P-wave / S-wave reflection data (Hearn,

2004), and refraction data (Meulenbroek and Hearn, 2010).

Interaction of S-waves with Fractures

One of the most heavily researched aspects of S-wave seismology is the phenomenon of S-wave splitting, first observed in earthquake recordings. S waves travelling through a fractured medium split into two separate waves, a faster wave that vibrates in the direction of the fracturing, and a slower one that vibrates in the orthogonal direction (e.g. Crampin et al, 1980 , Crampin and Lovell, 1991). In theory, therefore, an idea of the amount of fracturing can be determined by measuring the time delay between the two waves. The orientation of fracturing can be derived by measuring the polarisation direction of the faster S wave.

In the exploration context, the technique has commonly been applied in boreholes. Turner and Hearn (1995) give an example of shear-wave splitting analysis applied in an Otway Basin petroleum project, while Suthers and Hearn (1997) applied the technique to coal borehole data from the Bowen Basin.

It is more difficult to observe the phenomenon in surface reflection data, partly because of surface interactions. At the coal scale, in particular, reflection appears not to lend itself to S-wave splitting analysis (Velseis, 2007). However, it is feasible that the same azimuthal anisotropy that yields shear-wave splitting may also contribute to observable azimuthal variations in reflected S-wave images. This is a relatively unexplored concept, which will form a core component of the present investigation.

1.2.4 Pure S-Wave Seismic Reflection

The intuitive approach to acquiring S-wave seismic reflection data is to generate an S-wave signal at the surface and record the reflection using horizontally orientated geophones (Figure 1.1b). Early investigations centred around trying to develop a suitable S-wave source. A range of exotic devices emerged, including swing pendulum-mounted weights (White et al., 1956) and complex patterns of explosives (White and Sengbush, 1963). These were often cumbersome to deploy or expensive to use, and not viable for commercial scale seismic exploration. The 1960's saw the introduction of Vibroseis units capable of generating S-waves (e.g. Cherry and Waters, 1968).

Pure S-wave reflection is theoretically intuitive, and has found specialised applications in very shallow reflection (<50m). However, it has ultimately not emerged as a viable practical tool for

petroleum or coal exploration. Firstly, the necessity for a specialised source has meant that an S-wave survey is essentially standalone, effectively doubling the cost of a conventional P-wave survey. Secondly, because both the downgoing and upgoing reflection rays are S-waves, the returned signal is often subject to severe attenuation, yielding very poor resolution.

Over the past two decades, PS reflection has emerged as a more cost effective, and geophysically superior approach to obtaining S-wave information.

1.2.5 Converted-Wave (PS) Seismic Reflection

When a seismic wave comes in contact with an impedance contrast, some of the energy is reflected and some transmitted. It is possible that, upon reflection, some energy may be converted from P-wave to S-wave, and vice verse. The amount of mode conversion which occurs depends on the seismic velocities and densities in the two media, and on the angle of incidence. Of particular practical interest is the case where a P-wave converts to an S-wave upon reflection (Figure 1.1 c). This style of reflection is often referred to as converted-wave (or more specifically PS-wave) reflection.

As seen in Figure 1.1c, the PS reflection is asymmetrical, and this introduces some data handling challenges. On the other hand, a standard P-wave source is used, meaning that PS data can be acquired at the same time as conventional P-wave data, provided the standard vertical geophone is replaced with a multi-component phone, capable of recording both vertical and horizontal ground motion. The makes PS recording much more cost effective than pure S recording. In addition, because only the reflected leg is an S-wave, the PS recording is less heavily attenuated than the pure-S event. Hence, PS surveys are more competitive in terms of resolution (e.g. Gaiser and Strudley, 2005).

In 1985 one of the first commercial surface PS-wave surveys was conducted by Garrotta (Stewart et. al., 2002). This was a 2D2C survey (i.e. using only the vertical and radial-horizontal sensor components). Since then, 2D converted wave exploration has been used sporadically in the petroleum industry, generally as an experimental method (Hoffe et al., 1998) or for region specific problems (e.g. gas clouds) which render P-wave imagery ineffective (eg. Macleod et al, 1999; Berteussen et al, 1999; Li et. al. 2001).

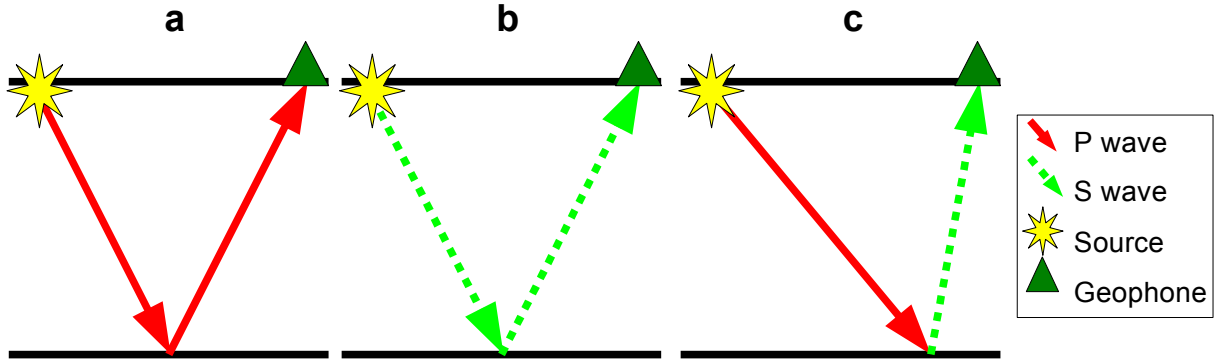

Figure 1.1: Different approaches to seismic reflection. Seismic waves are generated near the surface, reflect off a subsurface target, and are recorded at the surface. (a) Conventional seismic reflection uses a P-wave source and vertical-component sensor. (b) S-wave reflection uses a specialised S-wave source and requires a horizontal-component sensor. (c) Converted- wave reflection uses a standard P-wave source. Some of the downgoing P-wave energy converts into an upgoing S-wave upon reflection. A multicomponent geophone is used to capture both P-wave and converted-wave energy.

As noted above, the reality of 3D geology forced the transition from 2D to 3D P-wave reflection. Similarly, it was inevitable that PS reflection should eventually move from a 2D to 3D mode. In 1988 the first documented petroleum 3D3C (vertical, radial, transverse components) land seismic survey was conducted at Silo Field Wyoming (Garrotta and Granger, 1988). In the mid 1990s the recording technology had advanced to the point where it was economical to acquire large-scale 3D PS surveys for petroleum targets. For example, starting in 1995 a number of 3D PS experiments were conducted by the CREWES project at the Blackfoot field in Alberta, Canada (Simin et al., 1996; Lu, 1998; Dufour et al., 2002). These experiments demonstrated that good PS-wave images can be generated for petroleum-scale land targets and PS data can contribute to the overall geological interpretation of the area. Another important set of surveys for the petroleum industry were those acquired at the Alba (Hanson et al., 1999; Gaiser and Strudley, 2005) and Valhall (Brzostowski et al., 1999; Olofsson et al., 2003; Gaiser and Strudley, 2005) fields in the North Sea. These surveys were pivotal in demonstrating the use of 3D3C PS surveys in the marine petroleum industry as they greatly contributed to the life of both fields.

1.2.6 Coal-Scale PS-wave Reflection

Most of the converted-wave data acquired globally to date has been designed to image deep petroleum targets (greater than 800m). It was noted above that at that scale, pure S-wave surveys and PS-wave surveys did not tend to exhibit any resolution advantages, since dominant frequencies are reduced by anelastic attenuation. It had been suggested (Garotta, 1999) that there might be

greater chance of achieving S-wave resolution advantages for shallower targets, since the S-wave travels a shorter distance.

To date, there has been relatively little published work on converted-wave reflection at the coal scale. (Guy, 2004) reported on a shallow 2D multicomponent survey in Ohio. The section included a coal seam at 80m but this was not the main focus of the investigation. The paper includes source records for each of the components. Pure P-wave and S-wave reflections were identified and good stacks obtained for these. It appears that strong PS converted reflections occurred at far offsets, but these were not considered in the paper.

Driven initially by the prospect of improved resolution of coal targets, a number of shallow 2D integrated P and PS surveys were conducted in Australia's Bowen Basin between 2001 and 2005, with support from the Australian Coal Association Research Program (Hearn, 2004; Velseis, 2003 and 2007). These experiments (ACARP projects C10020, C13029) were over shallow coal targets with depths ranging from 30-200m. These studies demonstrated that even at these relatively shallow depths, PS waves exhibit reduced dominant frequency compared with P-waves, such that resolution is typically only comparable. However, other advantages were demonstrated. Firstly, the time delay associated with PS reflections means that they potentially arrive after some of the surface-wave noise, meaning that PS imagery is capable of imaging shallower targets than P-waves. This is of particular relevance to open-cut coal mining. Additionally, the PS-wave imagery sometimes indicated structural features that were not clearly visible on the normal P-wave image.

On the other hand, shallow coal reflection by nature requires far-offset, and broad-bandwidth data. These factors tend to emphasise some of the complexities associated with the converted-wave technique. In brief, PS-wave processing is more challenging for shallow onshore coal data than for petroleum-scale marine data. The preceding ACARP 2D converted-wave experiments have also indicated that, as with P-wave reflection, the earth cannot be accurately imaged unless three-dimensional variations are allowed for. At the coal scale, however, 3D-PS imaging presents particular challenges.

1.2.7 Azimuthal Anisotropy - a Challenge for Coal-Scale 3D-PS Reflection

One particular problem observed in our previous 2D-PS research is that a 2D image constructed using only rays travelling in the positive direction can exhibit significant timing differences compared to the image constructed using only negative-offset rays. This problem has been identified

at the petroleum scale where the term *diodic illumination* has been coined. Figure 1.2 illustrates that the fundamental cause is that PS reflection rays are asymmetric. Hence the geologies traversed by the P and S ray segments can be very different for the positive and negative offset rays. Time and amplitude differences can be expected because P-waves and S-waves will often exhibit different sensitivities to anomalous zones.

Figure 1.3 gives a real data example of this problem, taken from our earlier 2D PS work. It is clear that the time differences introduced between the images built using the positive and negative offset rays can introduce significant smearing in a composite image. The problem observed here with respect to a 2D image will be further complicated in 3D recording, where the rays can travel at any azimuth. Such *azimuthal imaging* effects are expected to provide a major challenge in the 3D-PS concept being evaluated in this project.

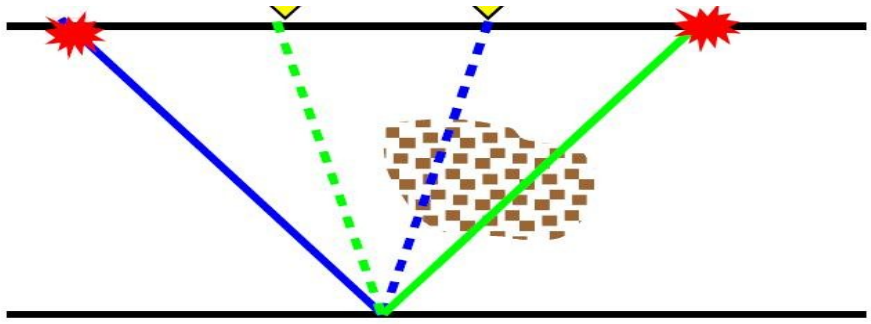

Figure 1.2: Example of diodic (directional) illumination in 2D PS reflection. Positive-offset (blue) and negative-offset (green) rays having the same reflection point are shown. An anomalous zone (hatched) is transited by the S-wave segment of the positive-offset ray, and the P-wave segment of the negative-offset ray.

1.3 Aims of ACARP Project C17029

The overall aim of this project is to extend recent coal-scale 2D converted-wave investigations from a 2D methodology to a full 3D technique. Knowledge developed in petroleum scale PS-wave exploration will be integrated with conventional coal-scale P-wave methodology. It will also be important to rigorously analyse how the shallow, coal-scale PS technique differs from the petroleum-scale technique. New data analysis methods will need to be developed to accommodate these differences.

More specific objectives of this study include identifying and interpreting azimuthal and ray-path

effects that are observed in petroleum scale data, which are expected to be magnified in the shallow environment. A comparative examination of the corresponding P-wave and PS-wave sections will clarify the degree to which each image is affected by such anisotropic problems. A desirable outcome is to demonstrate the degree to which anisotropy is dependent on the rock types and conditions within the survey area.

At present there are few demonstrated processing algorithms for shallow 3D PS-wave data. An important outcome of this project is to deliver an improved processing flow, which enables more meaningful interpretation of coal PS data, both 2D and3D. This will yield enhanced geological knowledge of the shallow coal environment. The work flow will examine advanced preprocessing and noise removal techniques, iterative refraction and residual-statics corrections, and anisotropic velocity analysis. Some of these processes are based on those currently used at the 3D petroleum-scale. However, the higher resolution requirements and greater raypath asymmetry associated with the shallow environment has necessitated additional algorithmic development.

The over-riding practical aim is that this research should contribute to the development of the 3D-3C seismic method as a cost-effective tool for the coal industry.

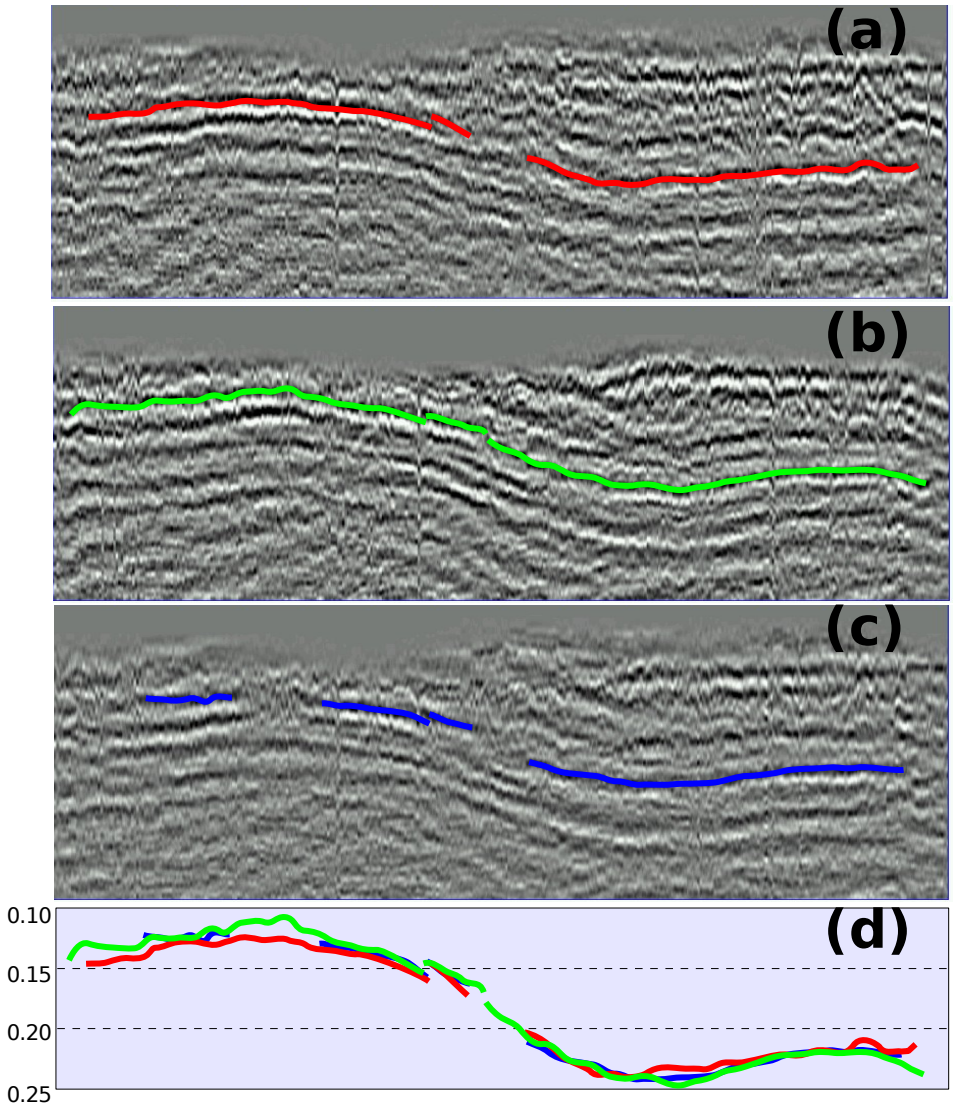

Figure 1.3: Example of diodic illumination in 2D coal-scale PS imaging. On the three seismic images, the horizontal extent is 1.75 km, and the time extent is 0.4s. (a) Image constructed using only positive-offset traces; (b) Image constructed using only negative-offset traces; (c) Image constructed using all traces; (d) Relative time positioning of the target coal seam horizon, as picked on the three images (time scale in seconds). From Strong and Hearn (2009).

1.4 Approach and Methodology

As described above, there has been minimal prior use of 3D-PS seismic-reflection in the shallow environment, and we are not aware of any over shallow coal targets. Therefore, an essential part of this project has been to acquire a dataset for testing. It was decided to acquire a small (400mx1200m) 3D swath with multi-component geophones and a Vibroseis source. The location chosen has been previously surveyed with 2D P-wave techniques. This showed that the geology

consists of a single coal seam dipping from 60m in the north to 130m in the south. A large fault (~10m) occurs near the middle of the line, with possible minor faulting to the north. A 2D-PS survey had also been acquired nearby. This suggested that reasonable converted-wave images could be generated at this location.

In the past, common midpoint fold plots were the primary tool for P-wave 3D survey design . This approach can result in reduced image quality when the geology is complicated (Galbraith, 1994). Therefore, there has been a move toward raypath design techniques. For PS surveys, these raypath techniques are essential due to the depth dependence of the reflection point and have been used in many of the 3D surveys conducted over petroleum targets (Hoffmann, 2001). The source and receiver geometry for this survey have been designed using raypath fold modelling based on borehole information and the earlier 2D P-wave dataset.

Statics associated with variations in the near surface have been found to have a significant effect on the data quality of 2D coal-scale PS data (Velseis, 2003). A 2D receiver domain residual statics method has given reasonable statics solutions on a number of datasets (Velseis, 2007). As a first step, it is logical to extend this approach to our new 3D data. For conventional P-wave surveys a combination of refraction and residual statics is used. Recent work by Meulenbroek and Hearn (2010) demonstrates a coal-scale refraction statics approach for 2D PS-wave data that shows promising results. An investigation of a 3D extension of this method is included as part of this research.

As noted above, a core component of this research is to explore the problem of azimuthal imaging variations, expected to be particularly severe in the context of 3D coal-scale PS imaging. The field data acquired for this project have been designed to have a very high fold. This allows the data to be divided into separate subsets based on source-receiver azimuth while maintaining reasonable final stack fold for each subset. The purpose of this is to be able to compare the azimuthal variations in the data at every stage of processing.

1.5 Overview of this Report

Chapter 1 has included a detailed technical background to the project, aimed at clarifying the current state of the art in coal reflection seismology. The chapter introduces the aims of the project, and methods to be used.

Chapter 2 describes the logic used to design the parameters for the field trial. The emphasis is on the way in which PS survey design is complicated (compared to P-wave) because of the asymmetry of PS ray paths.

Chapter 3 describes in detail the data acquisition phase of the 3D-PS field trial. It includes discussion of field logistics and methods, and also discusses the quality of the recorded raw data.

Chapter 4 gives an overview of the computer processing for the conventional P-wave data and the PS-wave data. It gives particular emphasis to specific extensions required for 3D-PS processing compared with 2D-PS.

Chapter 5 presents a more detailed examination of one particular challenge in the data processing, namely the problem of spurious time errors (statics) introduced by near surface geological variations. If not accounted for, such errors can be misinterpreted as being due to structures or lithology occurring at depth. In the case of the PS data, static errors are more severe for the upward travelling S-wave. Hence the focus is on the solution of receiver S-wave statics. Several approaches to the problem are examined and compared.

Chapter 6 presents stacked volumes derived from the P-wave and PS data, and presents an integrated geological interpretation. This chapter also demonstrates various attribute analyses, derived from the P and PS volumes.

The PS volume interpreted in Chapter 6 incorporates rays travelling in all azimuthal directions, as is the standard approach for conventional 3D P-wave volumes. Whilst the resultant PS volume is quite interpretable, one of the fundamental questions for this project is to examine whether azimuthal variations exist which could potentially cause smearing in such an 'averaged' volume.

Chapter 7 presents this detailed examination of azimuthal anisotropy, particularly in respect of the PS data volume. The chapter examines whether azimuthal variation exists, and whether obvious geological or logistical causes can be identified.

Chapter 8 summarises the main conclusions from the project, and suggests future directions for research into coal-scale 3C PS reflection.

2 Design of 3D-PS Field Trial

2.1 Introduction

A key stage in any seismic acquisition program is the survey design. The primary technical aim is to ensure that the source and receiver spacings are positioned such that the target will be imaged at the highest possible fold and resolution. In production situations this must be balanced against logistical and economic constraints.

Common-midpoint fold-plots are often the primary tool for P-wave 3D survey design . When the geology is complicated, this simple approach can result in reduced image quality. In such situations, ray-path design techniques are preferred.

For converted (PS) waves, the survey design is more complex than for P-waves, since the reflection point is asymmetric and is dependent on the depth of the target, the ratio of P-wave velocity to S-wave velocity (γ), and the source-to-receiver offset. Figure 2.1 shows a section of the earth with reflectors at varying depths. The image compares ray-paths for P waves and PS waves and demonstrates that the P-wave reflection point is the same for all depths, whereas the PS reflection point is closer to the receiver for shallower reflectors. In Figure 2.2 a map view is given of a single source positioned off line from a receiver line. The reflection point is given for γ (Vp/Vs) values varying from 1.0 (corresponding to P-wave data) to 2.5 (PS γ values are often in the range 1.5 - 2.5). This plot indicates that for P waves the reflection point is always halfway between the source and the receiver. However, for PS data, the reflection point is closer to the receiver for greater offsets and higher γ values. These results imply that survey parameters optimised for one location may not be appropriate for another. Therefore, even for simple geologies, ray-path techniques are essential for PS survey design.

In this project, the complexities of P and PS survey design have been investigated using 3D ray-path modelling and 2D visco-elastic finite-difference wave-equation modelling . The ray-path modelling examines the azimuth and offset distribution of the rays contributing to each reflection bin. The finite-difference modelling investigates the offset limitations imposed by phase variations in the seismic data.

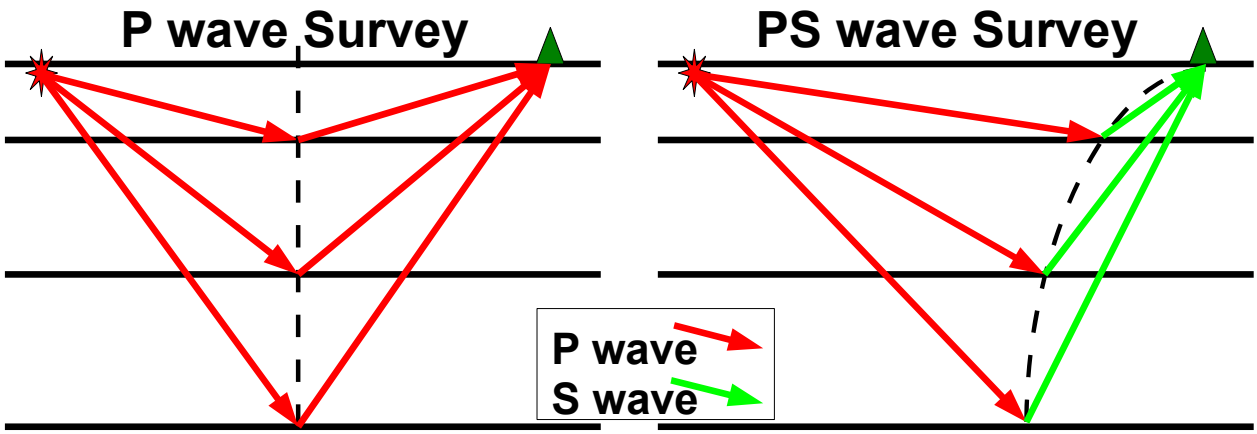

Figure 2.1: Comparison of the reflection point with depth for P and PS surveys. The asymmetric and depth-varying nature of PS waves increases the complexity of PS survey design.

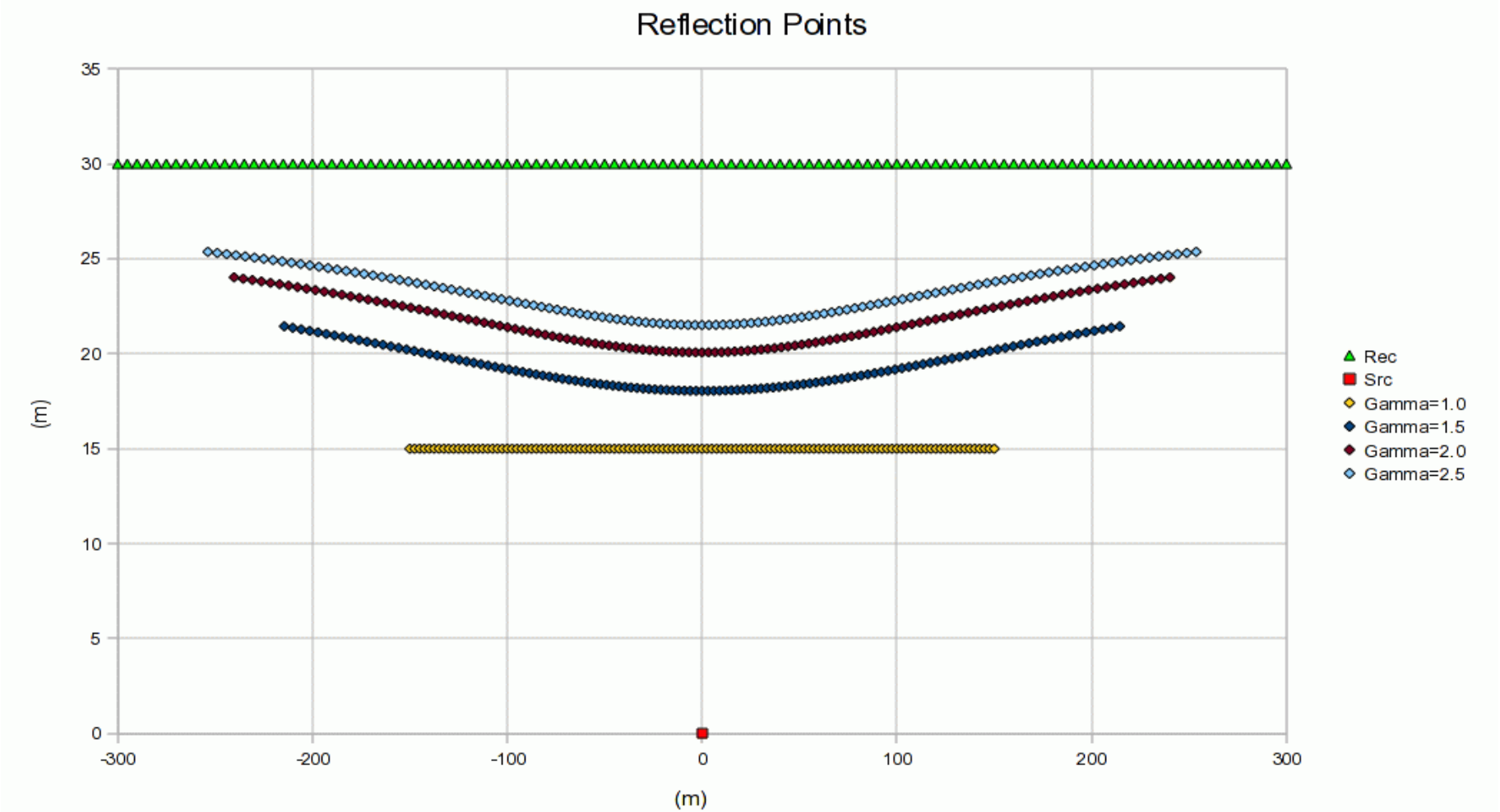

Figure 2.2: Map view of reflection points from a source point (red) to a receiver line (green). For P-waves (γ=1) the reflection point is always midway between source and receiver. PS ray-paths are asymmetric, with the reflection point dependent on target offset and γ. The PS reflection points shown here correspond to a target depth of 100m.

2.2 Simple survey design model

In order to design the layout of source and receiver points for the 3D3C seismic trial, a variety of ray-path models have been examined. The parameters have been chosen based on typical P-wave surveys with similar targets and resolution requirements.

For the initial tests we have created a shallow coal-scale model with a single reflector at 100m (the average depth of the real target). The simplest survey design consists of an orthogonal grid where the source lines are perpendicular to the receiver lines. To emphasise the effects of varying the survey design parameters, consider a very high-fold orthogonal grid consisting of inline and crossline spacings of 15m for both the sources and receivers. Figure 2.3 shows a map view of a 600x600m segment of such a simple model.

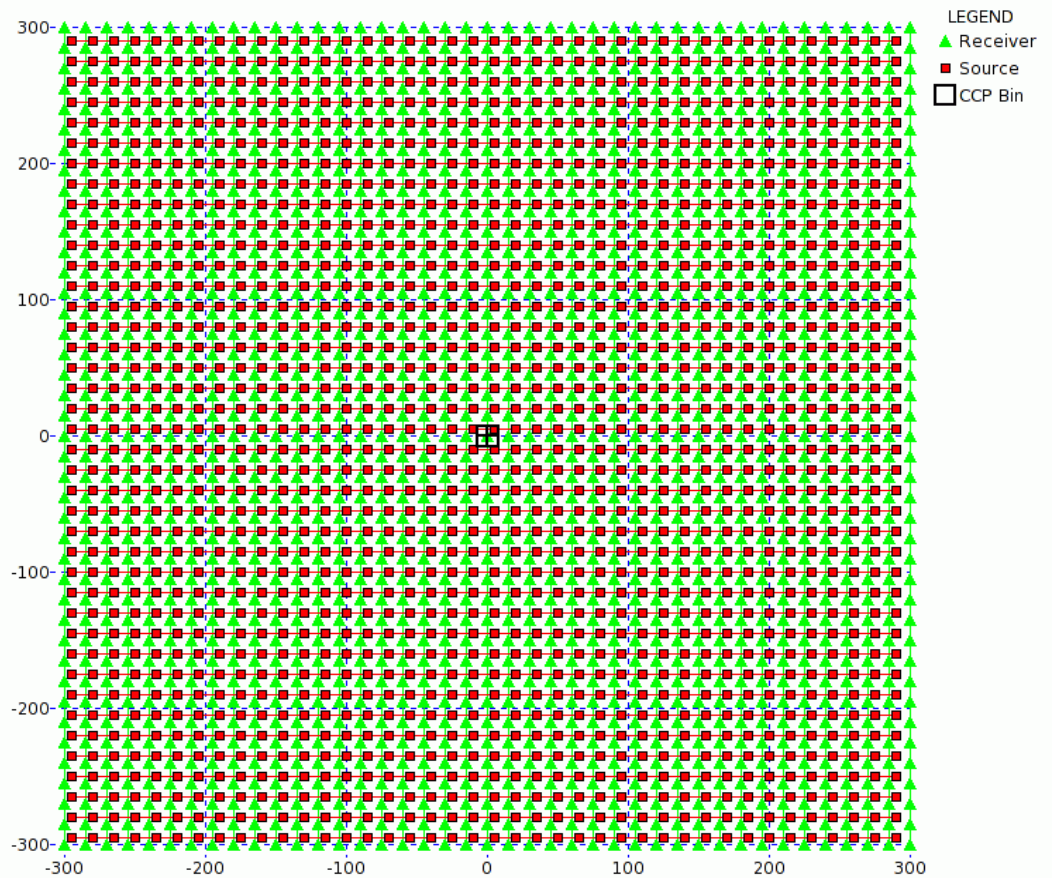

Figure 2.3: Segment of simple orthogonal grid. Sources and receivers are spaced on a regular 15m x 15m grid.

One of the key objective of the ray-path modelling is to determine optimal source and receiver locations such that a regular and continuous distribution of ray azimuths and offsets is achieved for

each reflection bin. When this is not achieved, a spurious *acquisition footprint* may be visible in the final stacked volume. In addition, such irregularities would also complicate any azimuthal anisotropy investigation, such as that proposed in the present study. *Spider plots* are commonly used in 3D design to summarise azimuth and offset distributions. In Figure 2.4, P and PS spider plots are given for a sample 7.5 x 7.5m reflection bin from the centre of the grid represented in Figure 2.3. This is the natural bin size for the P-wave data as is indicated by the good coverage. Note, however, that the orthogonal grid gives rise to a very ordered distribution, which can lead to an acquisition footprint in the final 3D images.

The PS spider plot shows a similar ordered pattern. However, coverage is much poorer than for P, with reduced fold and much poorer azimuth/offset distribution. Furthermore, unlike P-wave data, if the same reflection bin is considered for a target at a different depth, the azimuth/offset coverage will be different (Figure 2.5). This is a side effect of the asymmetric nature of PS waves.

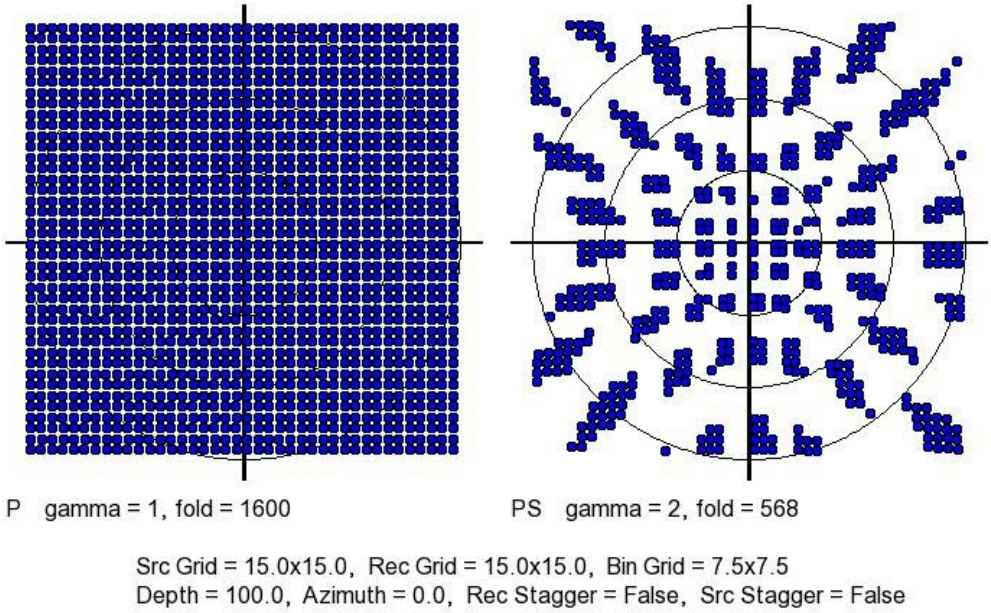

Figure 2.4: Azimuth and offset distributions for rays contributing to a 7.5mx7.5m bin at the centre of the grid shown in Figure 2.3. The target reflector is at a depth of 100m. Distributions are shown for P (left) and PS (right) surveys.

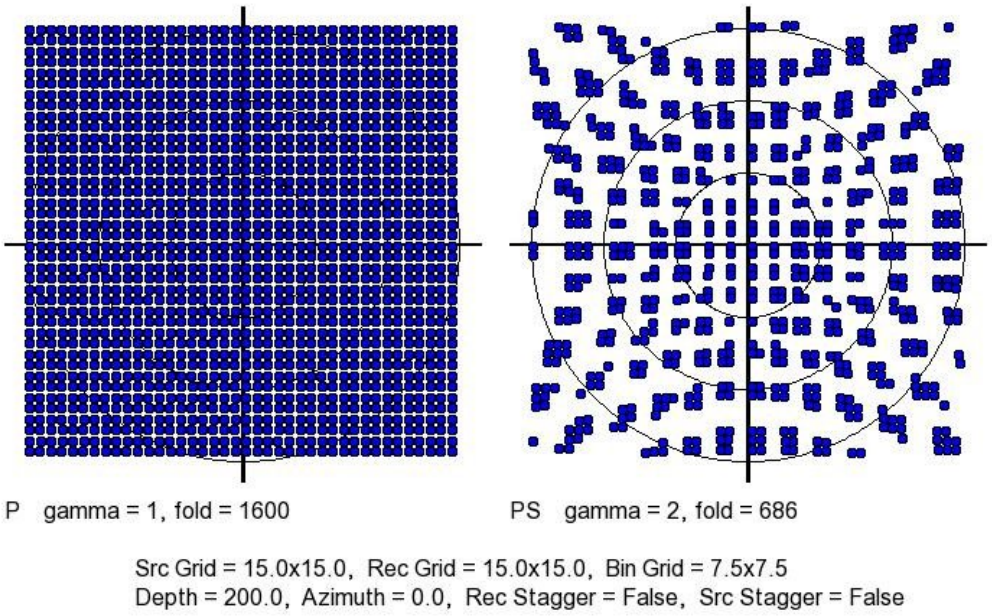

Figure 2.5: Azimuth and offset distributions for rays contributing to a 7.5mx7.5m bin at the centre of the grid shown in Figure 2.3. The target reflector is at a depth of 200m. Distributions are shown for P (left) and PS (right) surveys. Compared with Figure 2.4, the P-wave plot is unchanged whereas the PS plot a different offset/azimuth distribution.

In order to obtain a continuous distribution of azimuths/offsets for PS data the bin size must be increased. Figure 2.6 shows the PS spider plot for a target at 100m with the bin size increased to 15x15m. This results in a significant increase in fold and a continuous distribution of azimuths and offsets. The trade-off is a decrease in lateral resolution.

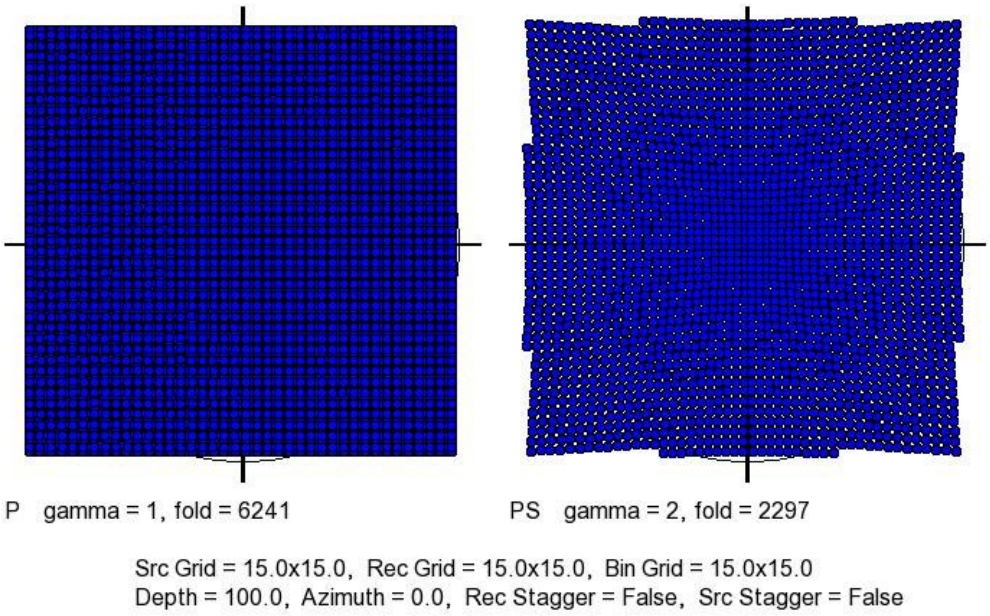

Figure 2.6: Azimuth and offset distributions for rays contributing to a 15m x 15m bin at the centre of the grid shown in Figure 2.3. The target reflector is at a depth of 100m. Distributions are shown for P (left) and PS (right) surveys. Compare with Figure 2.4.

Generally in 3D surveys it is not economically feasible to acquire data with fold as high as in these models. Either the receiver or the source spacing must be increased. The choice is dependent on factors such as equipment availability, speed of acquisition, and type of source. For example, Vibroseis surveys tend to favour higher source density, whereas in dynamite surveys increased receiver density would typically be more cost effective. The preceding example has shown that if the CCP bins are too small relative to the design parameters, a continuous distribution of azimuths and offsets is not possible for PS-wave data. However, what is not clear is whether this is a function of the receiver spacing or source spacing.

This matter will be examined with reference to two tests. In the first, the bin size and the receiver spacing is kept at 15x15m but the source spacing is increased to 30x30m (Figure 2.7). In the second test the bin size and the source spacing is kept at 15x15m but the receiver spacing is increased to 30x30m (Figure 2.8). These tests show that increasing the receiver spacing leads to discontinuities in the azimuth/offset distribution. On the other hand, changing the the source spacing only affects the fold and not the distribution. This suggest that the 'natural' CCP bin size for converted waves is the receiver spacing.

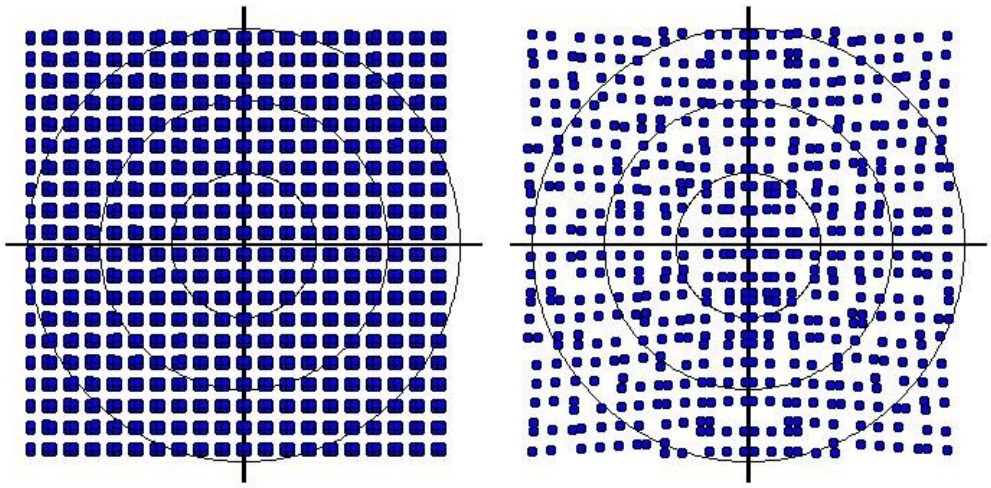

Figure 2.7: Azimuth and offset distributions for rays contributing to a 15m x 15m bin at the centre of an orthogonal grid. Receivers are located on a 15m x 15m grid. Sources are located on a 30mx 30m grid. The target reflector is at a depth of 100m. Distributions are shown for P (left) and PS (right) surveys. Compare with Figure 2.8.

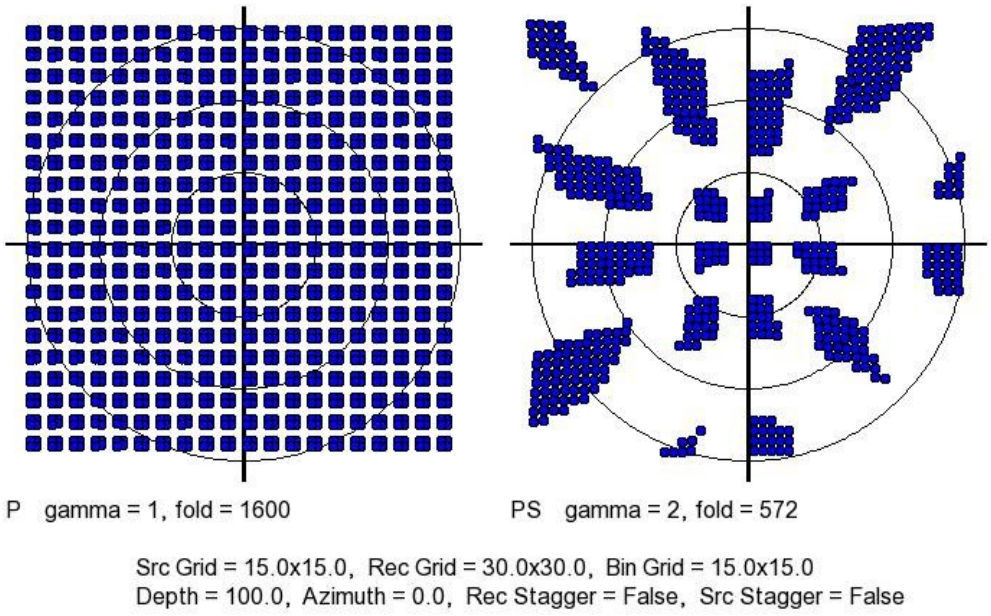

Figure 2.8: Azimuth and offset distributions for rays contributing to a 15m x 15m bin at the centre of an orthogonal grid. Receivers are located on a 30m x 30m grid. Sources are located on a 15m x 15m grid. The target reflector is at a depth of 100m. Distributions are shown for P (left) and PS (right) surveys. Compare with Figure 2.7

2.3 Improving the survey design.

For this project a it has been decided that a source spacing of 30x30m and a receiver spacing of 15x30m will give a very high fold dataset, suitable for azimuthal analysis while maintaining economic and resolution requirements. Figure 2.9 shows the the spider plots corresponding to an orthogonal grid for a representative CCP bin of size 15x30m (natural PS bin size). This figure shows that the azimuth/offset distribution has a gridded nature, especially for the P-wave data. As noted above, this can result in fold in adjacent bins varying in a systematic manner, which can cause amplitude variations in the final stacked data (acquisition footprint).

In conventional P-wave 3D surveys, acquisition footprints are reduced by angling or staggering the location of the source lines. Figure 2.10 shows the spider plots for a grid where the source lines are rotated by 30 degrees from orthogonal. All other parameters are the same as Figure 2.9. The P-wave spider plot is more scattered than for the orthogonal case. It is expected that this would reduce the acquisition footprint. The PS distribution is also less regular than before.

In Figure 2.11 a 'stagger' has been applied to the angled source lines. This means that the position of sources, relative to receiver lines, changes from one source line to the next. (See Figure 2.17 for detail.) This provides a further degree of 'randomness' and yields a further minor improvement in the scatter of the azimuth/offset distribution of the spider plots.

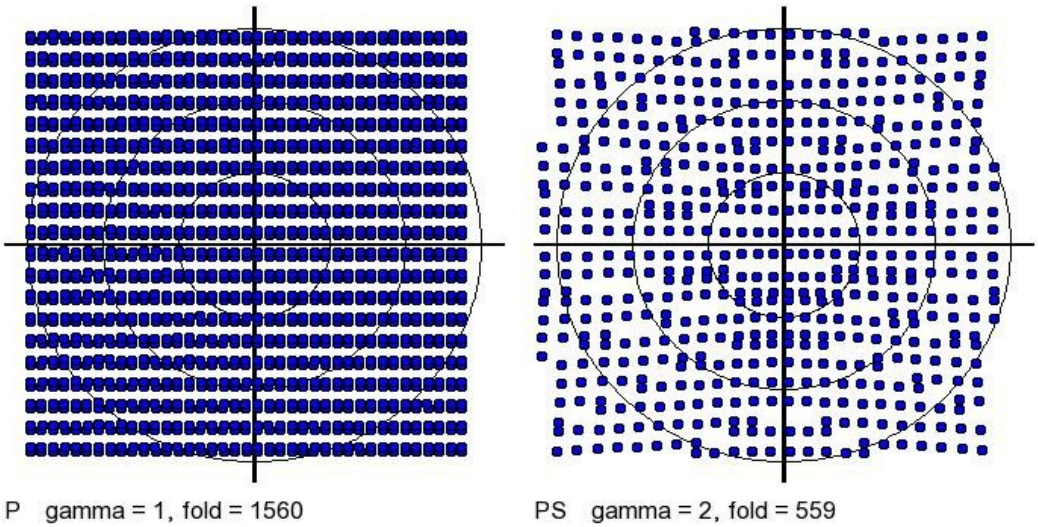

Figure 2.9: Azimuth and offset distributions for rays contributing to a 15m x 30m bin at the centre of an orthogonal grid. Receivers are located on a 15m x 30m grid. Sources are located on a 30mx 30m grid. The target reflector is at a depth of 100m. Distributions are shown for P (left) and PS (right) surveys. Compare with Figure 2.10.

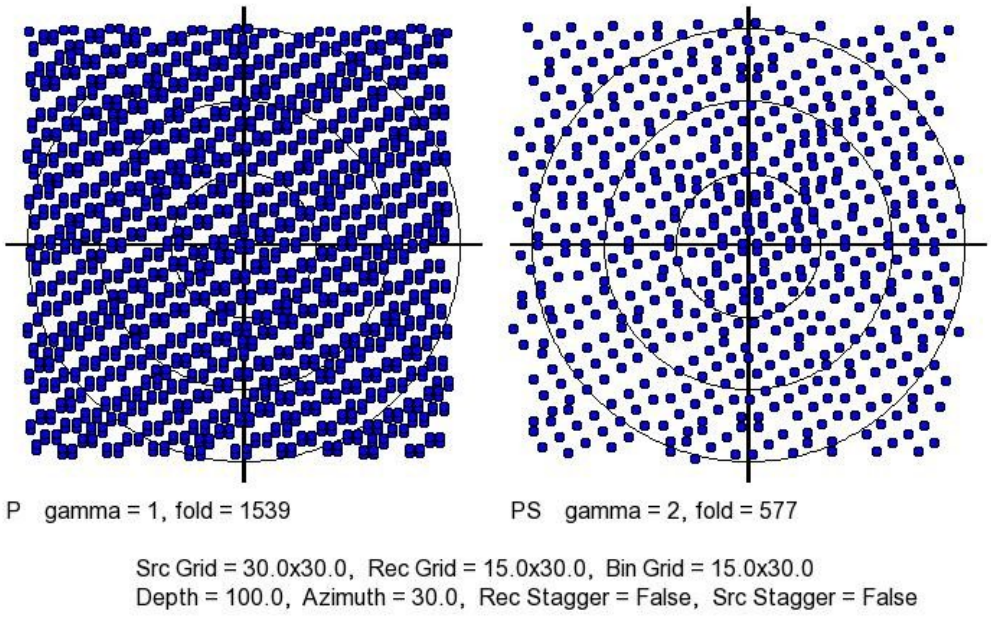

Figure 2.10: Azimuth and offset distributions for a survey design identical to that in Figure 2.9, except that the source lines are at an angle of 30 ° to the receiver lines. The azimuth/offset distribution is less regular (particularly for the P-wave data (left).

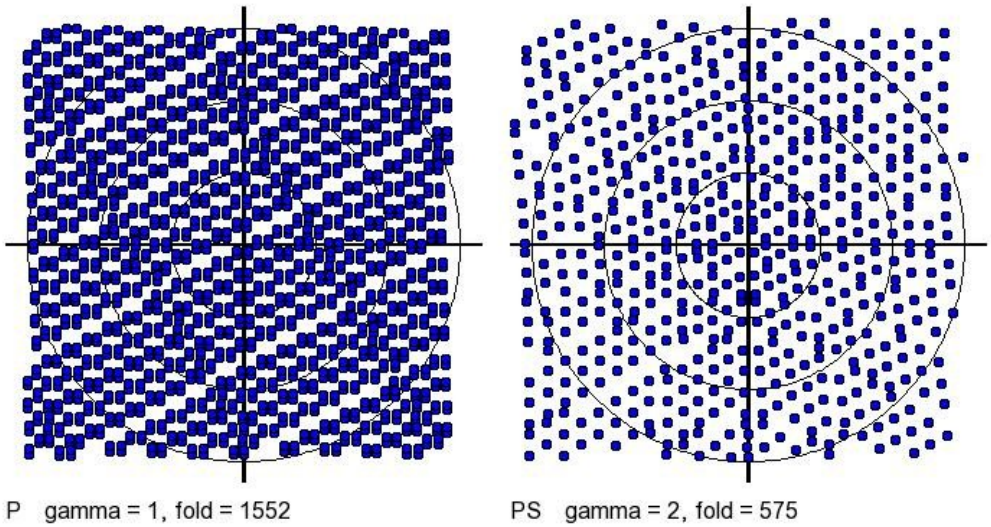

Figure 2.11: Azimuth and offset distributions for a survey design identical to that in Figure 2.10, except that the source 'stagger' has been applied. This provides a slight improvement in the randomness of the distribution, compared to Figure 2.10.

2.4 Phase verse offset effects

Another important concept to consider is the variation of the phase of the recorded seismic wave with offset. At some seismic reflection boundaries, seismic rays having an angle of incidence greater than the critical angle will produce wavelets with a phase variation. The practical effect is that the shape of the wavelet changes, and smearing is introduced in subsequent stacks. If this change is significant it must be either accounted for in processing, often a difficult task, or offsets beyond this point must be discarded.

To examine this effect we will consider a single-seam coal model (Figure 2.12). The parameters of this model are based on likely parameters for the real survey.

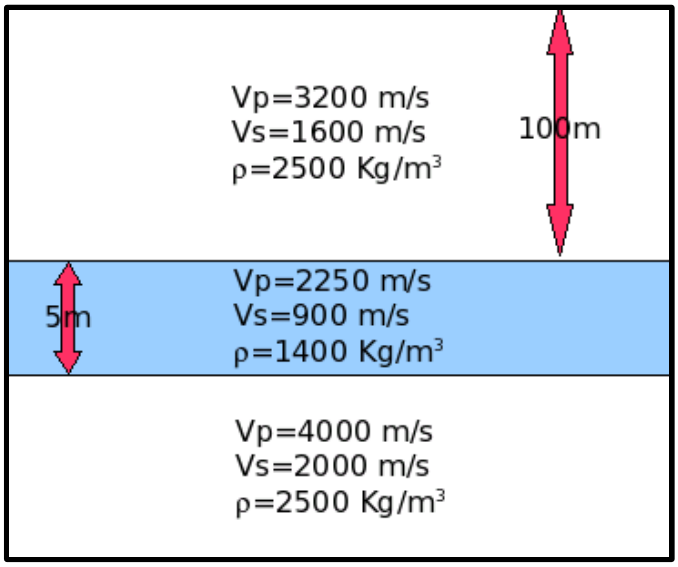

Figure 2.12: Coal seam model used in analysis of phase vs. offset. The parameters shown in the figure are indicative of those expected in the real field trial.

In general, the reflection package from a coal seam is an interference package, incorporating both the top-of-coal and base-of-coal reflections. Firstly, consider the reflection from the top of the target coal seam. Figure 2.13 shows a graph of the magnitude (solid lines) and phase (dashed lines) versus incident angle for the P (red) and PS (green) reflections. Note that the P reflection has good reflection coefficients (around 0.4) at low incident angles. Comparable PS reflection strengths require greater incident angles, i.e. greater offsets. The phase responses are well behaved. The PS reflection from top-of-coal does not produce any phase change, while the P-wave exhibits a constant 180 degree shift (i.e. a polarity reversal). These results imply that reflections from the top of the coal seam only have amplitude variations with offset and are not subject to phase changes.

At the base of a coal seam there is an impedance increase, and hence we see a much more complicated reflection coefficient behaviour. In Figure 2.14 there is a phase discontinuity for both P and PS reflections at the critical angle.

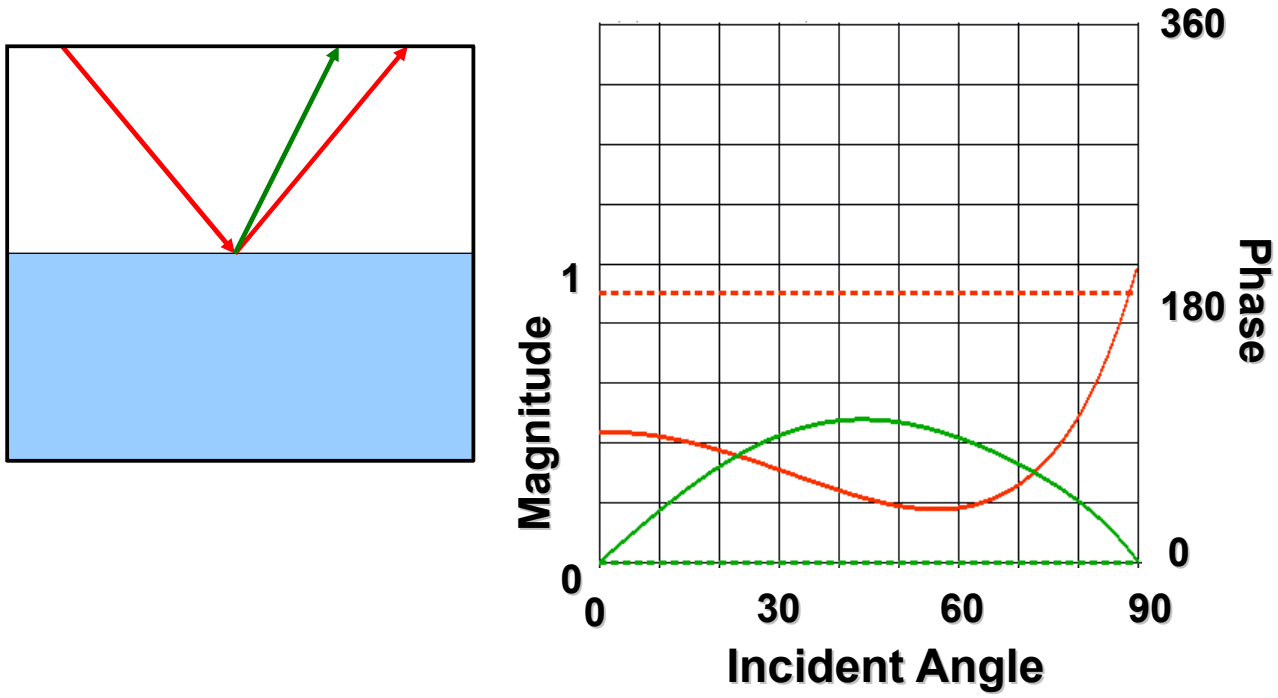

Figure 2.13: Phase vs offset analysis for top-of-coal reflections for P (red) and PS (green) reflections. Magnitude (solid curves) and Phase (dashed) variations are shown as a function of incident angle (and hence offset). Magnitude varies with offset for both reflection types. Phase response does not change with offset.

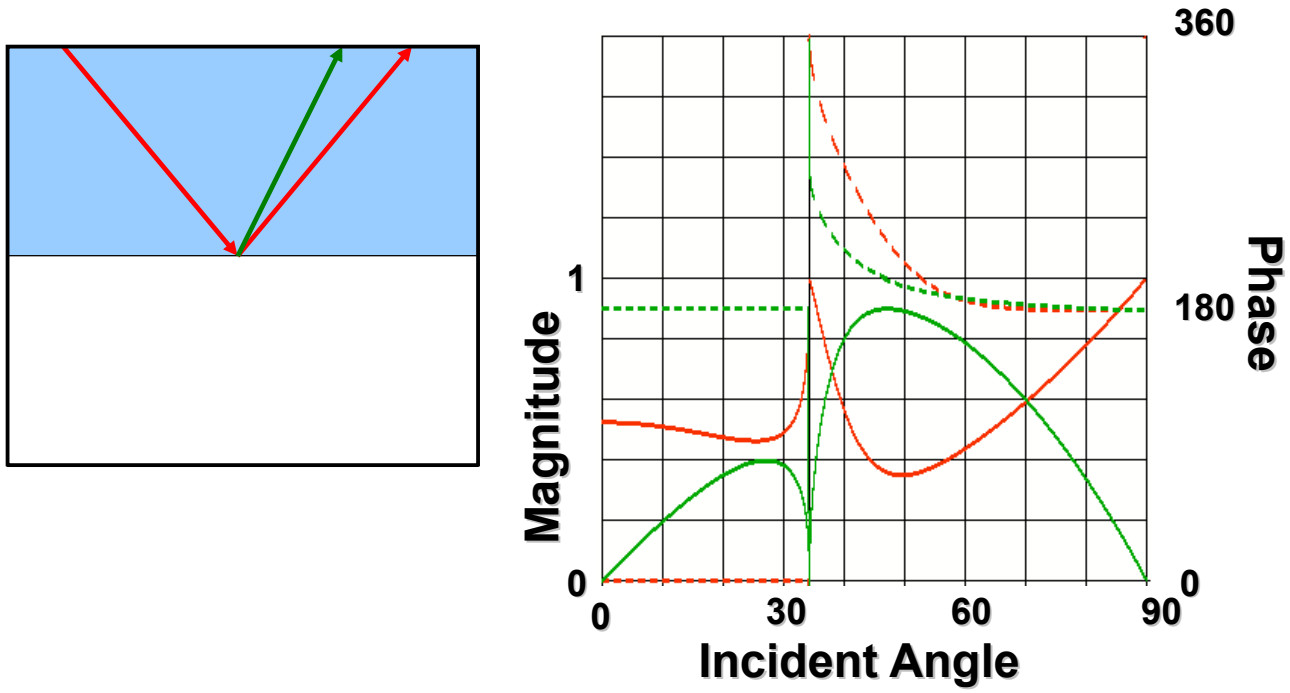

Figure 2.14: Phase vs offset analysis for base-of-coal reflections for P (red) and PS (green) reflections. Magnitude (solid curves) and Phase (dashed) variations are shown as a function of incident angle (offset). Magnitude varies with offset for both reflection types. Phase response for both wave types changes significantly at the critical angle (~ 34°).

If we wish to completely avoid such phase changes, we would need to restrict our base-coal incident angles to be less than this critical angle. With ray trace modelling we can predict the offset at which these phase distortions occur, for P and PS reflections, and for coal seams of different thicknesses (Figure 2.15). For example, for a 5m seam thick at a depth of 100m the phase distortion occurs at an offset of about 270m for P, but only 185m for PS. The ray-path modelling in Figure 2.15 suggests that the problem is in theory worse for PS than for P and for the given model parameters reduces the usable offset of PS data by approximately one third (compared to P data).

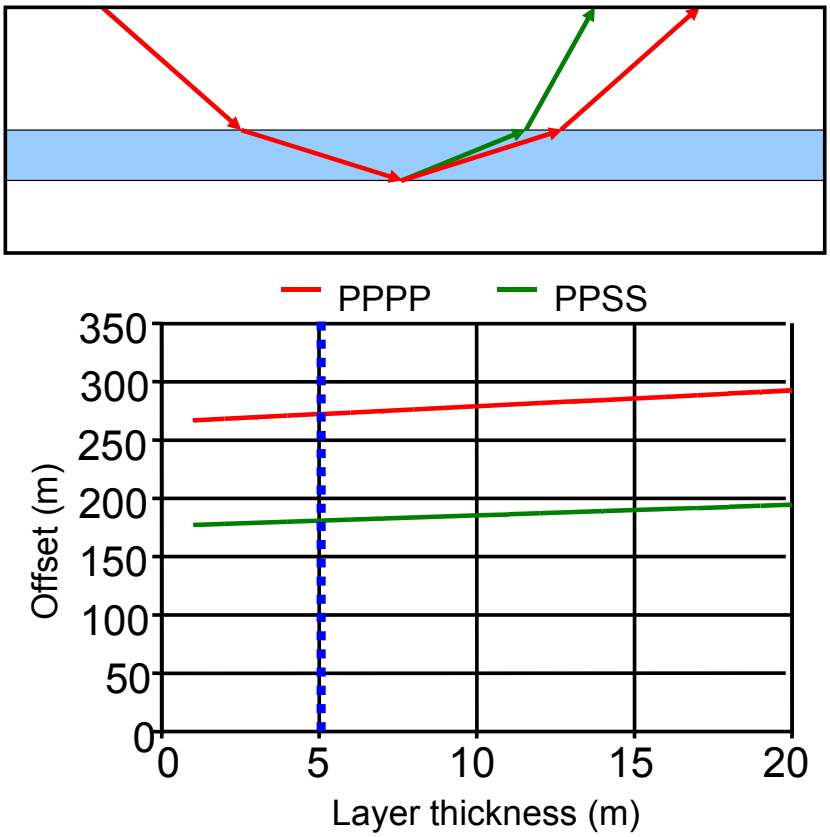

Figure 2.15: Ray-path modelling to estimate offset at which critical-angle phase distortion is expected, for coal seams of various thicknesses. For a 5m seam, P (red) and PS (green) offsets should be restricted to 185m and 270m respectively.

The preceding reflectivity modelling approach provides a simple first-order indication of the offsets at which phase problems should be anticipated. It does not really indicate how severe the distortion will be on the actual recorded data. In addition, coal targets often involve a number of thin seams grouped closely together. The seismic wavelet associated with these is an interference pattern of the individual wavelets from each interface. Reflectivity modelling is less appropriate to these more realistic situations

A more powerful approach to understanding the practical real-data impact of base-of-seam phase distortions is via wave-equation modelling. This can provide an image of the expected seismic recording from a seam configuration of any complexity.

Figure 2.16 shows a vertical shot record simulated using viscoelastic finite-difference modelling, for the case of the 5m target seam in Figure 2.12. The P-wave image is shown at the top, with target reflections from the top and base of seam marked in purple. Based on the preceding reflectivity modelling, any phase distortion would be expected beyond 270m offset (red box). However, in this case it appears that the base-of-coal reflection is swamped by energy from the top-of-coal reflection. We would not expect this distortion to present serious practical problems in conventional processing.

The corresponding inline horizontal record is shown at the bottom of Figure 2.16. The top and base of coal PS reflections again occur close together, resulting in an interference wavelet. Closer examination of the wavelet, indicates that it changes significantly with offset. This is the combined effect of the changing strength on the coal reflections with offset, and phase distortions. Beyond the critical angle (corresponding to offset 200m) there is certainly a distinct change in character of the reflection package due to phase variations (green box). The most obvious effect is the progressive shift of energy from the start to the rear of the wavelet.

While these phase concerns have been introduced in the 2D context it is obvious that they will also apply to 3D work. The implications of this to our preferred design and processing of the 3D trial is that we would not expect serious phase complexities on the P-wave data. However in the case of the PS recordings our offset distribution may be further restricted by potential distortion in far-offset traces.

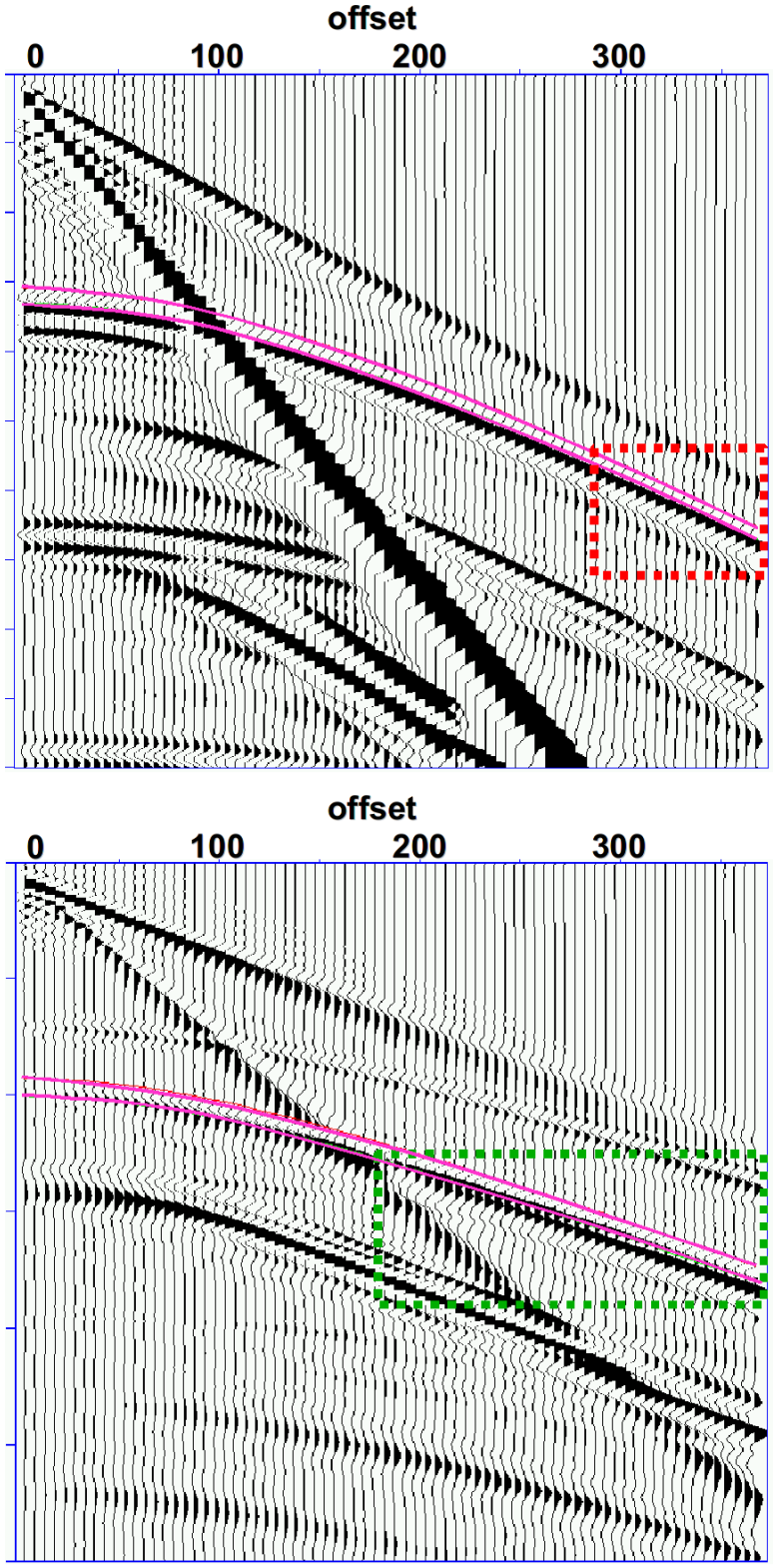

Figure 2.16: Finite-difference modelling of phase vs offset distortion for the model in Figure 2.12. On the vertical component record (top) P-wave distortion is much less pronounced (red box) than for the PS reflection on the inline horizontal record (bottom, green box).

2.5 Final 3D design parameters.

The preceding analysis has summarised the primary technical considerations for the real data survey design. In addition, the survey design had to be optimised to allow for a range of target depths (~70-120m), overall survey area (400x1200m), resolution requirements, and logistical / economic factors such as availability of equipment and personnel. Table 2.1 shows the statistics for the source and receiver locations plus some of the associated geometric parameters. Figure 2.17 provides a graphical representation of the basic survey geometry. Figure 2.18 shows the full layout of the source (red) and receiver (green) lines. To reduce the environmental impact of the survey some of these points were shifted slightly during acquisition.

Table 2.1: Source and Receiver Statistics

Number of receiver locations	660
Receiver spacing	15 m
Number of receiver lines	10
Receiver line spacing	30m
Total Length of receiver lines	9750m
Number of source locations	594
Source spacing	30m (34.64m in source line direction)
Number of source lines	44
Source line spacing	30m
Source line orientation	60 deg from receivers staggered (± 7.5m)
Total Length of source lines	18448m
Total line length	28198m

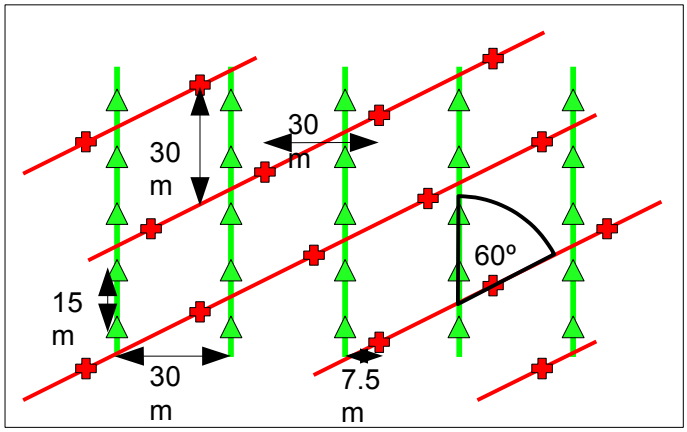

Figure 2.17: Sample of the Acquisition Geometry. Includes 5 source lines (red), 15 source locations (crosses), 5 receiver lines (green) and 25 receiver locations (triangles)

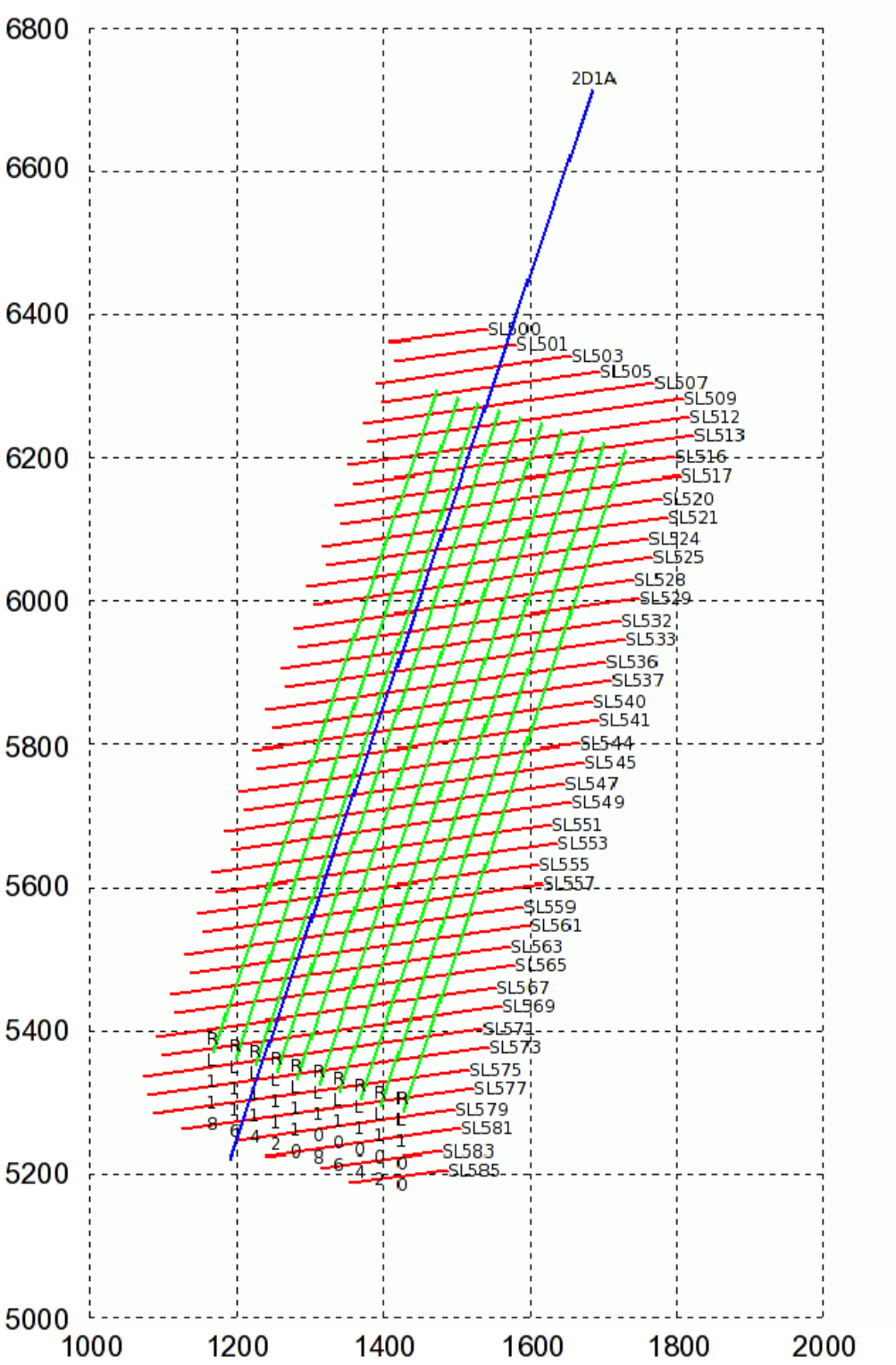

Figure 2.18: 3D/3C seismic survey grid. Includes 10 receiver lines (green), 44 source lines (red), and the coordinates of a conventional (P-wave) 2D-line (blue) that intersects the survey.

2.6 Conclusion

This research has demonstrated that survey design is more complicated for PS-wave (converted-wave) surveys than for conventional P-wave surveys. Modelling of ray-paths, reflectivity and phase distortion should be included in the survey design. This is especially so for coal-scale PS data because of the higher offset/target-depth ratios.

Ray-path modelling illustrates that azimuth/offset distributions are always likely to be less satisfactory for PS waves if the size of the reflection bins are chosen based on the natural size of P-wave data. This is intrinsically related to the asymmetric nature of the PS ray-paths, with consequent asymmetric binning patterns. This suggests that integrated P and PS acquisition programs should be designed with closer receiver spacing than standalone P-wave surveys to give optimal lateral-resolution for both datasets. Staggered and angled grids give a more random azimuth/offset distribution for 3D datasets. This is likely to lead to a reduction in the acquisition footprint.

Wave-equation and reflectivity modelling have demonstrated that phase variations with offset may be more problematic for PS data and could lead to a reduction of usable offsets and a further reduction in the fold of PS data.

The survey design arrived at for the ACARP 3D field trial is based on rigorous technical considerations, aimed at providing an optimum assessment of the feasibility of shallow 3D-PS reflection.

3 Acquisition of 3D-PS Test Dataset

3.1 Introduction

Velseis Pty Ltd, with support from ACARP has designed and acquired a 3D multi-component (3C) survey. The aim of this trial has been to asses the feasibility of acquiring and processing coal-scale converted (PS) wave data in conjunction with conventional (P) wave data in a 3D sense. We believe this to be the first coal-scale 3D/3C survey acquired in Australia. Additionally, the survey was designed to assist in the resolution of geological structures relevant to ongoing coal exploration.

The survey was conducted using a Vibroseis (IVI Envirovibe) source and was located at a host mine site within the Bowen Basin. This site was chosen based on geological constraints (simple coal seam, known faulting), accessibility, and good seismic results from a previous 2D P-wave dataset.

A Sercel 428 recording system was employed to record the data.

The host company was responsible for line clearing, permitting and de-permitting councils and property owners whilst Velseis sub-contracted and managed surveying, traffic control and general rehabilitation of the seismic lines.

The grid covered 0.5km^2 with 594 shot points on 44 shot lines and 660 receiver positions on 10 receiver lines. The total length was 9.75km, and the total length of source lines was 18.5km. Details of the survey design were given in Chapter 2.

Recording operations commenced on 06/11/2009 and were completed on 13/11/2009.

No lost time or restricted work injuries were recorded during the program.

3.2 Terrain

The terrain was generally flat to gently undulating (Figure 3.1). A creek cutting across the northern section of the survey had, in places, steep banks up to 3m in height (Figure 3.2). At the very southern end of the survey there was a washed out zone of up to 2m deep and extending for a length on the order of 100m.

Figure 3.1: Terrain at the test site was generally flat to undulating.

Figure 3.2: Larger elevation variations were associated with the creek in the north of the survey (shown here) and the washout at the south of the survey area.

The surface soil layers consisted of a brown clayish layer for most of the survey area. The southern third of the survey area consisted of a black soil terrain. This layer had many large cracks (Figure

3.3) and tended to crumble when dug up for geophone placement. An examination of a cutting in the washed out area suggested that the black soil overlays the brown soil layer having a thickness of 1-2m at the southern end and thinning with the decrease in elevation toward the north.

Some areas of the survey were lightly vegetated especially in the vicinity of the creek.

Figure 3.3: Cracked black soil terrain toward the southern part of the grid

3.3 Weather

The weather during the layout and the start of acquisition was dry. However, the last day and a half of acquisition was slowed by intermittent showers. These resulted in standby periods of up to 15min in a given hour. Analysis of the sub-surface showed that the moisture had a very limited depth of penetration (1-3cm) and was unlikely to cause significant variations in source coupling or receiver statics.

The wind conditions were quite variable. At times it was very still, especially during the morning. At other times it was gusty, usually during rain events. This contributed to slowing production, although the wind noise was reduced by burying the geophones.

3.4 Surveying/Line Preparation

Surveying services were provided by Conics Positioning and the lines were slashed by Mark Hodgeson Services. Geophone stations were marked by wooden stakes and paint marks. The

recording crew removed survey markers after completion of recording. Figure 2.15 shows the layout of the source and receiver lines.

3.5 Recording Parameters

Recording parameters were developed with due regard to both geological targets and survey costs. The survey was designed such that 4 separate azimuthal volumes can be created, each having a nominal CCP coverage of 25 or higher for most of the survey area. This fold was proposed to ensure that data quality was maintained despite possible changes in geological conditions and target depth.

The recording system parameters for the survey are shown in Table 3.1 and the source and receiver parameters are given in Table 3.2.

Table 3.1: Recording System

Recording system	Sercel 428XT
Recording	24 bit
Number of channels	1980
Sample rate	1.0 ms
High cut (anti alias) filter	0.8 Nyquist
Low cut filter	Nil
Recording media/format	1 Tb mirrored NAS hard-drive (SEG-D)
Archive/format	External USB hard-drive (SEG-D, SEG-Y)
Auxiliary channel 1	Time-break
Auxiliary channel 2	True Reference Sweep
Auxiliary channel 3	Ground Force Sweep
Auxiliary channel 4	Sweep Auto-correlation

Table 3.2: Source and Receiver Parameters

Source	Vibroseis	
Vibrator	Envirovibe	
Number of units	1	
Number of sweeps	1	
Sweep Type	Linear; 0.25s taper	
Force	70% (10,500lbs)	
	Test 1	Test 2
Sweep frequency	10 to 140Hz	7-80Hz
Sweep length	8s	5s
Record length (listen time)	2s	1.5s
Geophone array	Single 3 component phone; buried	
Orientation	Inline element pointing in the direction of increasing station number; levelled	
Element	3 x GS-30CT, 10 Hz, 390Ω	

3.6 Seismic Acquisition & Data Quality

3.6.1 In-field QC

The care and attention that is taken when laying out the receiver stations is very important in 3C seismic surveys. If errors are made at this stage it can have large effects on the data quality and can be difficult or impossible to accommodate in the processing stage. To ensure that the best data could be obtained the following procedures were put in place:

- Geophones levelled and pointing in the direction of increasing station number.
- Geophones buried to reduce wind noise (Figure 3.4).
- Geophone connectors colour coded for ease of identification (vertical – blue; inline – red; crossline – yellow).
- Geophone elements connected to the receiver lines in series (i.e. vertical followed by inline then crossline). On previous 2D/3C surveys, receiver lines were set-up for each geophone element, which resulted in a large number of cables on the ground. The change in procedure was implemented to increase speed of production and reduce possible errors associated with connecting geophones.

- The Sercel 428 system has the ability to list the serial number and order of the FDU's for any receiver line. These lists were printed and used by line checkers to ensure that FDU's were positioned correctly on the ground and that the correct geophone element was plugged into the correct channel. All FDU's were found to be connected in the correct order and only 6 geophones were found to be connected to the wrong channels. These were reconnected to the right channels prior to commencement of acquisition.
- The seismic records were monitored for irregularities (including reverse polarity, noisy and dead traces) during testing and production. The recorded data were separated based on component and each was analysed individually. From these we were able to identify that the geophone at station 258 line 118 was wired incorrectly (reverse polarity) and the connection for the inline component of station 330 Line 118 was damaged. These problems have been accounted for in the processing.
- The seismic records were also monitored, in conjunction with graphical noise analysis software, to determine when the acquisition had to be put on standby until noisy weather conditions passed.

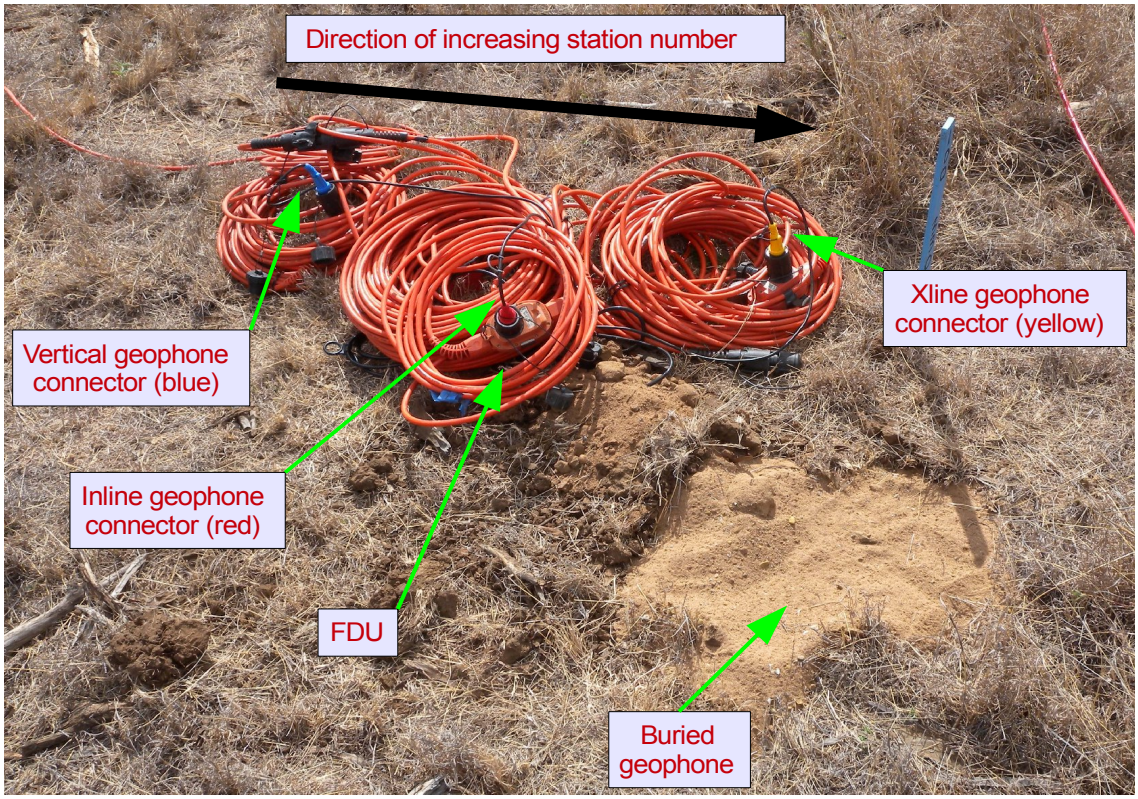

Figure 3.4: Geophone setup at one receiver station

3.6.2 Envirovibe Sweep Tests

An extensive suite of sweep tests were conducted as this was the first time that Velseis had acquired converted-wave data using using an Envirovibe source in this area (see Figure 3.5and refer to Appendix 11.1 for details on the Envirovibe source). These tests included a range of start and end frequencies; various sweep lengths and listen times; and different sweep types (linear, multi-sweep, non-linear, Vari-sweep). These tests were analysed in the field with the aim of producing the best conventional (P) and and converted (PS) wave results. An 8s linear sweep of 10-140Hz with a 2s listen time was chosen for the production sweep.

The main acquisition proceeded quite quickly (1.25 days). For this reason we decided that we would acquire another pass of the data. A number of further sweep tests were conducted and these, in conjunction with the original tests, were examined with the aim of designing a sweep to specifically target converted wave data. A 5s linear sweep of 7-80Hz with a 1.5s listen time was chosen for the second pass.

In total 144 test sweeps were acquired over 5 separate locations and this constitutes a very significant dataset. It is recommended that this be used at some future date for further quantitative assessment of the Envirovibe source.

Figure 3.5: Envirovibe moving along a source line at an angle to a receiver line. Communication cable is visible running along the receiver line.

3.6.3 Data Quality

Figure 3.6 shows the vertical component record generated by Source Point (567,100) i.e. located in the vicinity of receiver line 100. This record is representative of the data quality throughout the survey. The data have very good first breaks (P-wave refraction event) and have none of the feathering that is sometimes associated with Vibroseis sources. The majority of the energy from the conventional P-wave reflections is found on the vertical component and can be seen as the hyperbolic events that come after the first breaks. We can see that these have a quite good signal-to-noise ratio.

Figures 3.7 and 3.8 show horizontal component records generated by Source Point (567,100) and correspond to the inline and crossline components respectively. These records primarily consist of converted (PS) wave energy. There is an intermittent refraction-like event arround the time that the converted-wave refraction event is expected. However, based on shot-record analysis it is difficult to determine if this energy is associated with the converted waves or if it is cross-contamination of the P-wave refraction. This question is addressed in more detail in the statics analysis of Chapter 5. As is expected the signal-to-noise ratio of the horizontal components is poorer than the vertical. However, there appear to be converted-wave reflections on both components, especially on the mid to far offsets. For this example the inline component has a slightly better signal-to-noise ratio then the crossline component. This is probably due to the rectangular shape of the acquisition patch, with larger offsets in the inline direction.

The near offsets of all components are affected by significant amounts of coherent noise, such as ground roll. This noise should be considered during processing and where possible removed to ensure improved stack results.

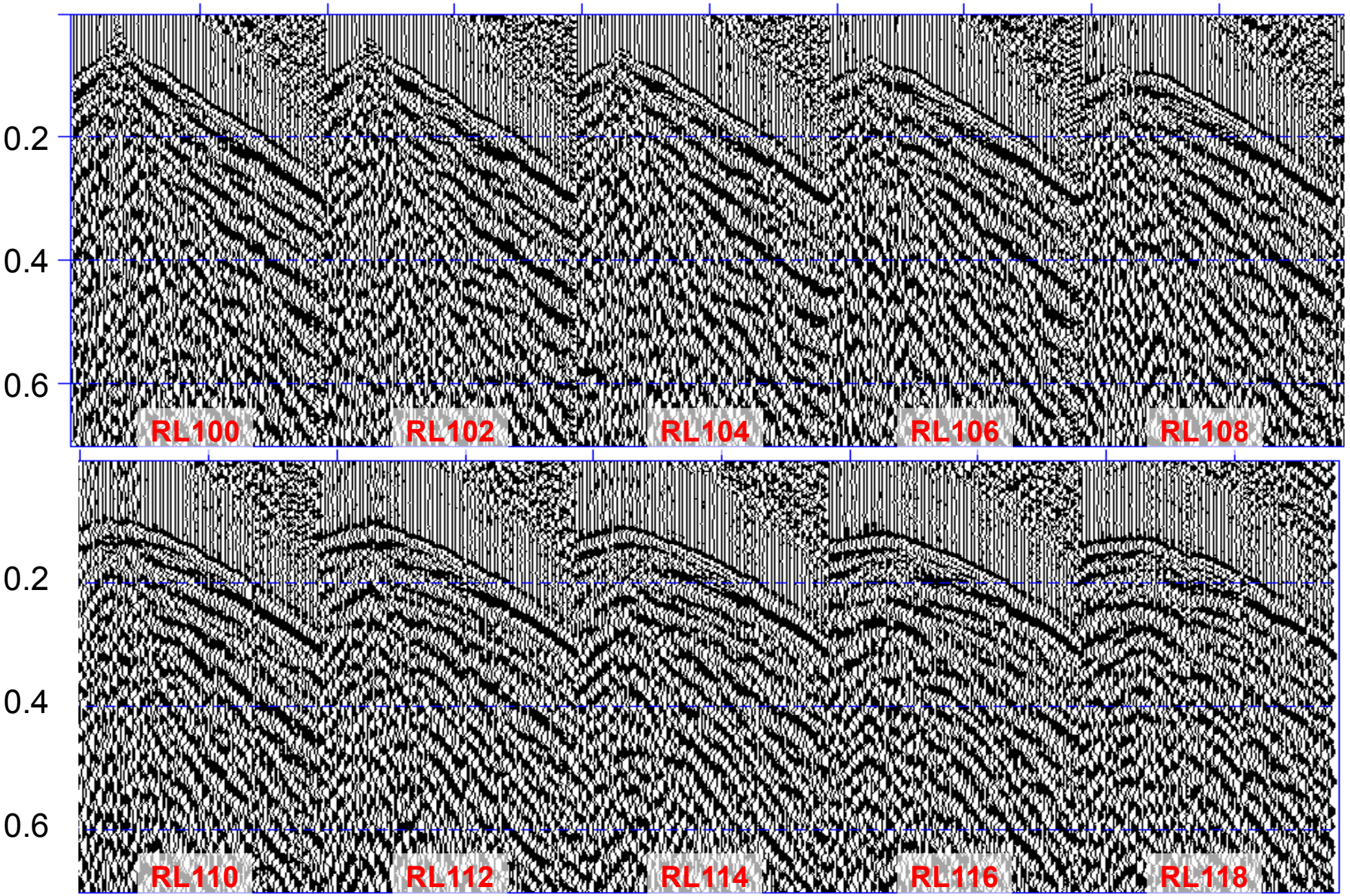

Figure 3.6: Vertical Component of the seismic record for Source Point (567,100) into Receiver Lines 100-118.

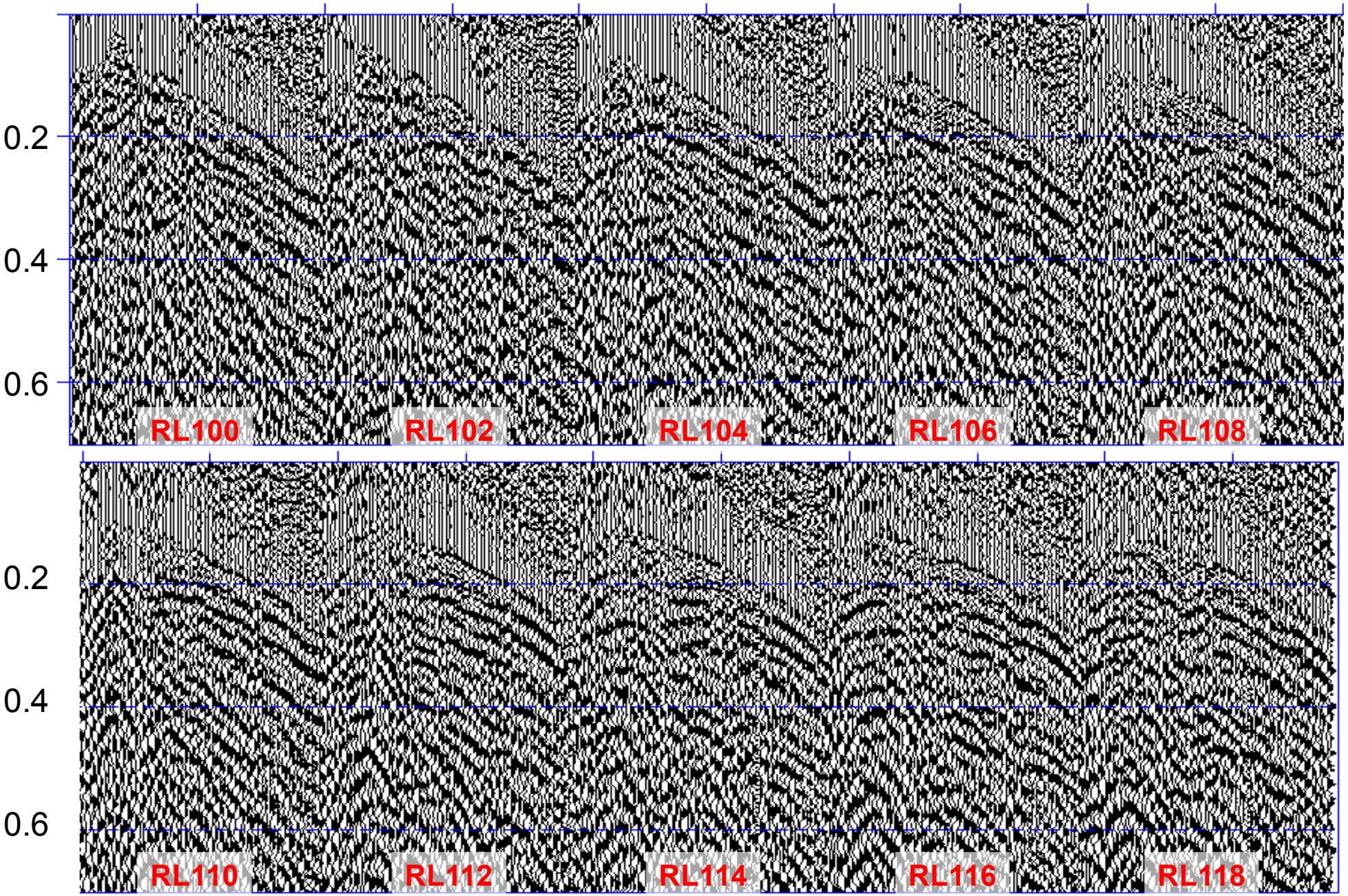

Figure 3.7: In-line Component of the seismic record for Source Point (567,100) into Receiver Lines 100-118.

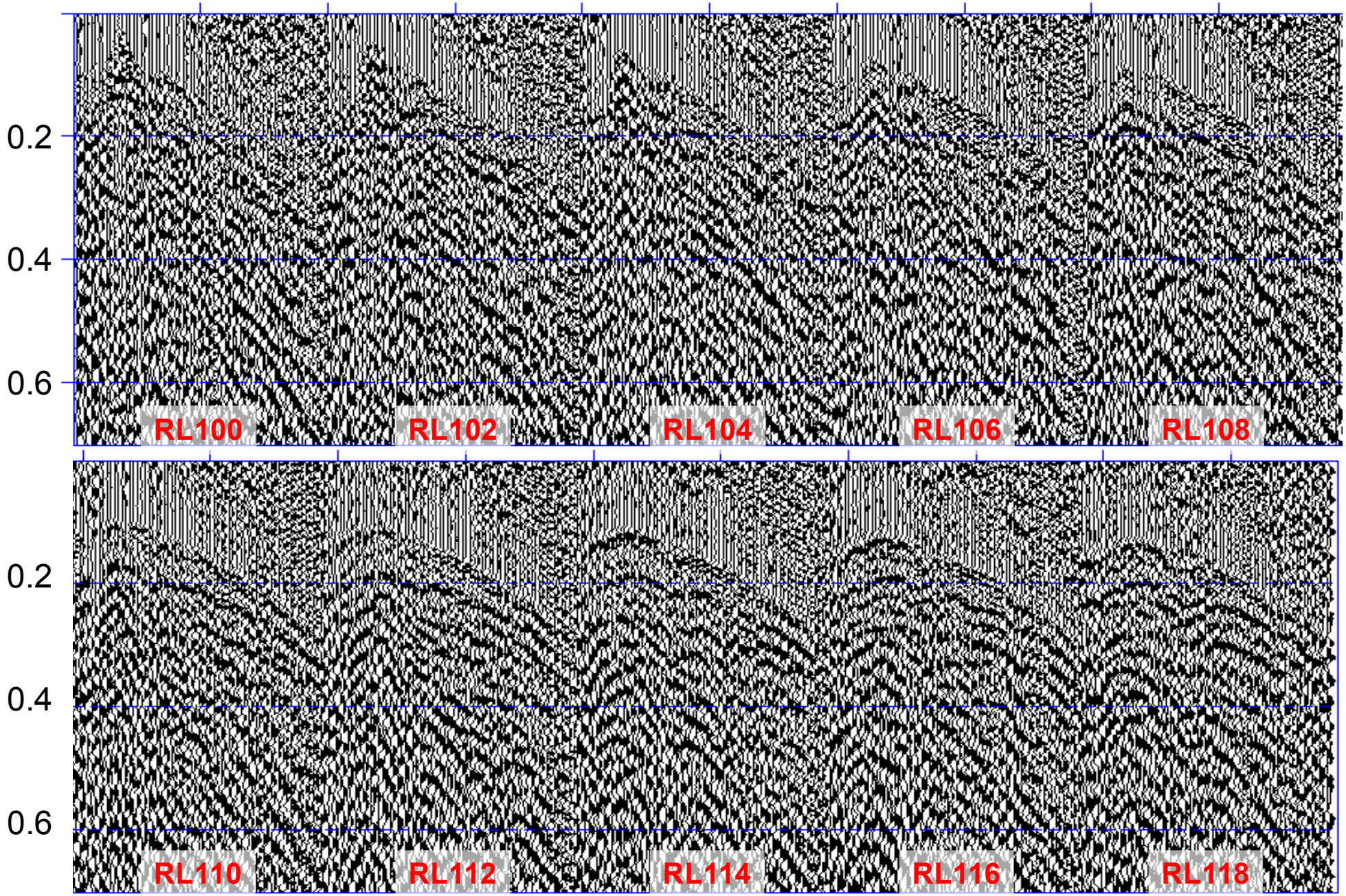

Figure 3.8: Cross-line Component of the seismic record for Source Point (567,100) into Receiver Lines 100-118.

3.7 Summary

This survey has demonstrated that 3D-PS coal-scale seismic data can be acquired economically with minimal variation to the standard field equipment and techniques.

The quality of the P-wave data was excellent. The PS data quality was poorer but was quite reasonable compared to the previous 2D coal-scale PS surveys acquired by Velseis. Quite strong coherent noise was present in the data due to the use of low-frequency geophones. It may be necessary to filter out this in processing to obtain an optimally processed stack.

As part of the investigation a significant number of Envirovibe sweep tests were acquired. It is recommended that a more rigorous examination of these be conducted at some future date and from this a Vibroseis sweep test procedure be developed.

4 Processing Overview

4.1 Introduction

Converted-wave processing is quite complex and is the most time consuming stage in obtaining a PS dataset. Difficulties arise from the asymmetric nature of the PS ray-path, larger PS surface statics, azimuthally varying geological environments, and low signal-to-noise ratio. Nevertheless, ACARP projects C10020 and C13024 have demonstrated that these issues are not insurmountable and as a result of these projects a reasonable processing sequence has been developed for the 2D case.

The 2D processing sequence provides a good basis for processing the trial 3D-PS dataset. However, some modifications and extensions are required. This includes relatively straightforward methodological extensions (e.g. coordinate rotation, 3D binning, 3D statics inversion, etc.). The dataset acquired for this survey has also allowed us to examine whether ray-path azimuth variations affect the data and a specialised processing sequence has been developed to allow this to be investigated.

The flowcharts in Figures 4.1-4.3 show the primary processing flow used for the final stacked volumes. The conventional, P-wave processing (Figure 4.2) has been largely performed using the industry-standard Promax package. The PS processing (Figure 4.3) has been performed using in-house software built around the data-handling framework provided by Seismic Unix from the Colorado School of Mines.

This chapter will discuss some of the non-standard processing stages and testing that has been conducted.

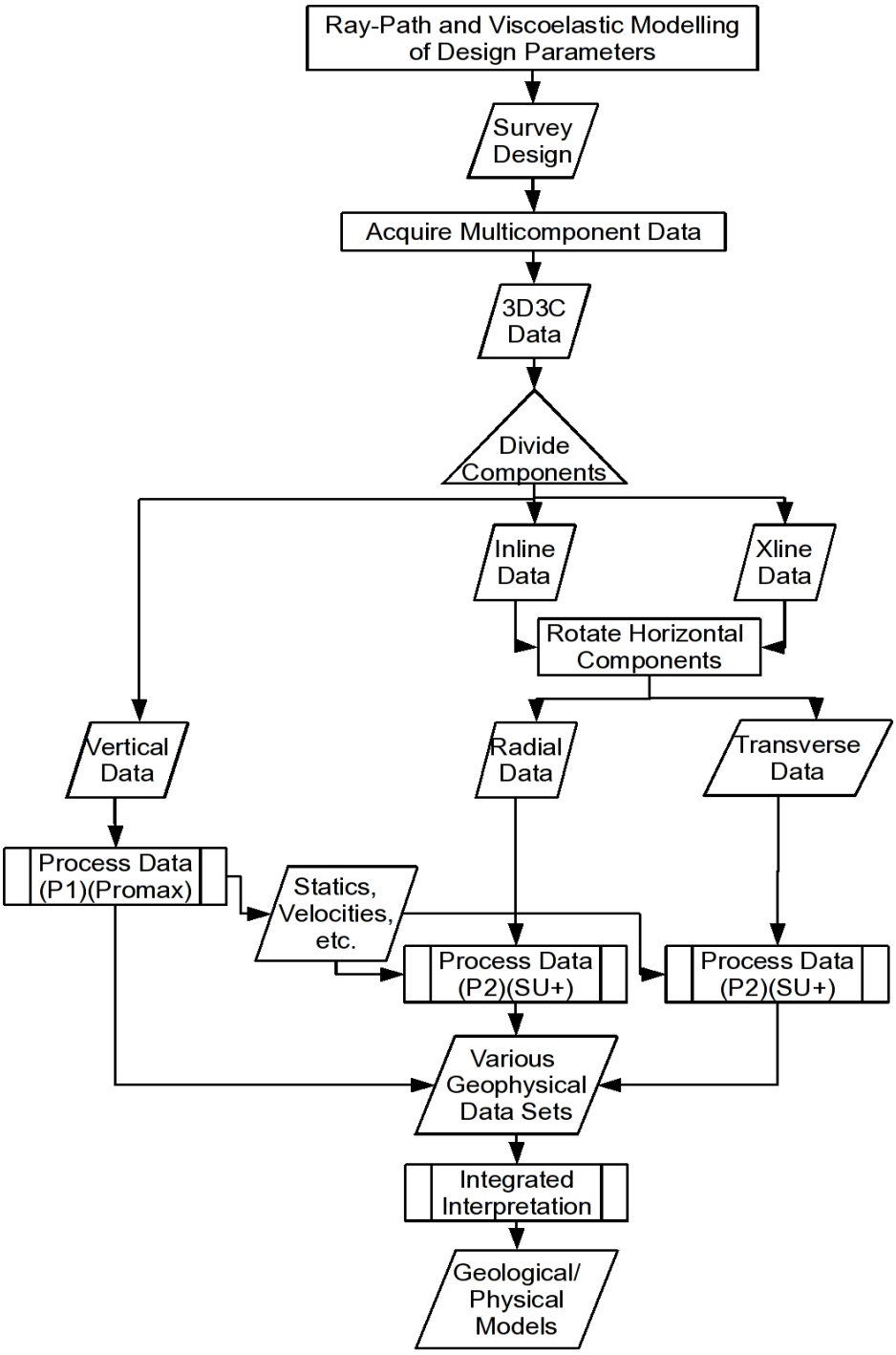

Figure 4.1: Flowchart showing the general outline of the acquisition and processing sequence for a 3D integrated P+PS survey. Note that the PS processing requires information from the P processing flow. This implies that the P processing must be completed first.

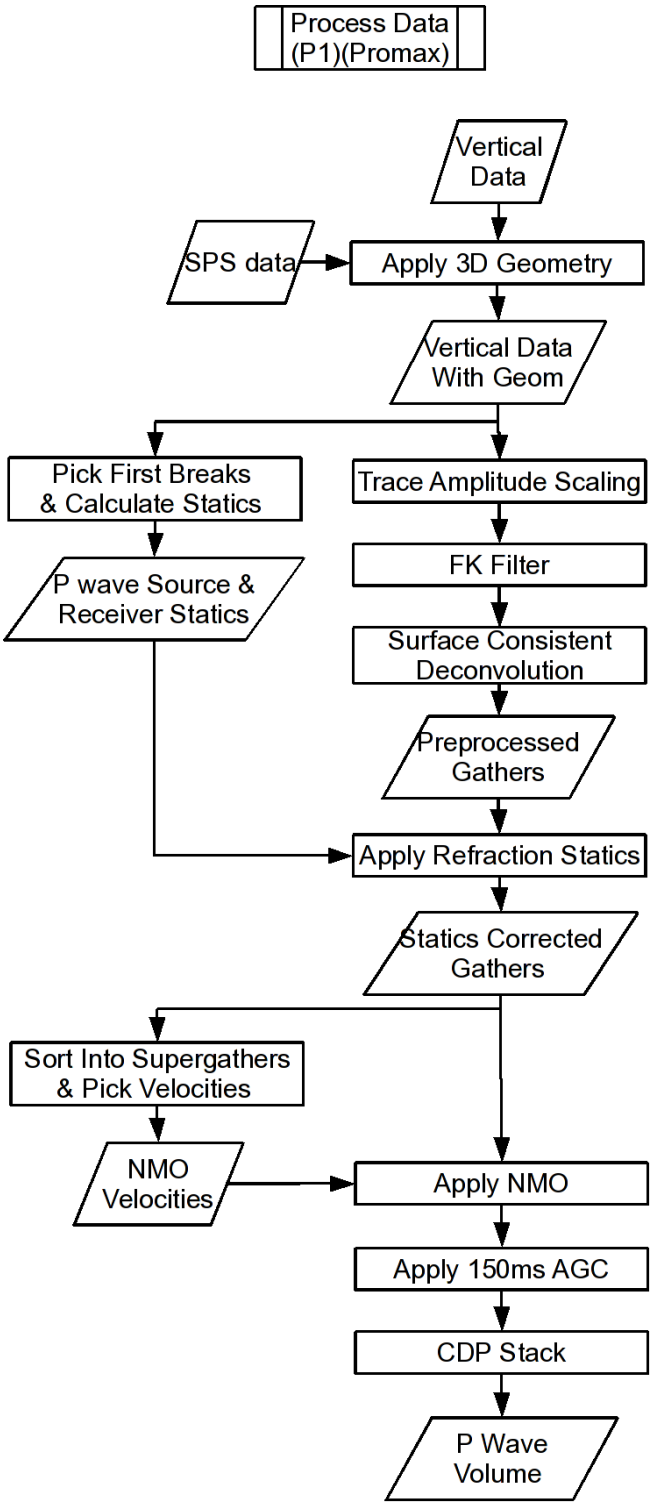

Figure 4.2: P-wave processing flow used in this investigation. This is a fairly standard processing flow for coal-scale data. The only variation is the inclusion of the FK-filter for groundroll suppression. Generally, higher frequency geophones are used to remove most of the groundroll during acquisition. The P-wave data were processed using the Promax commercial software suite.

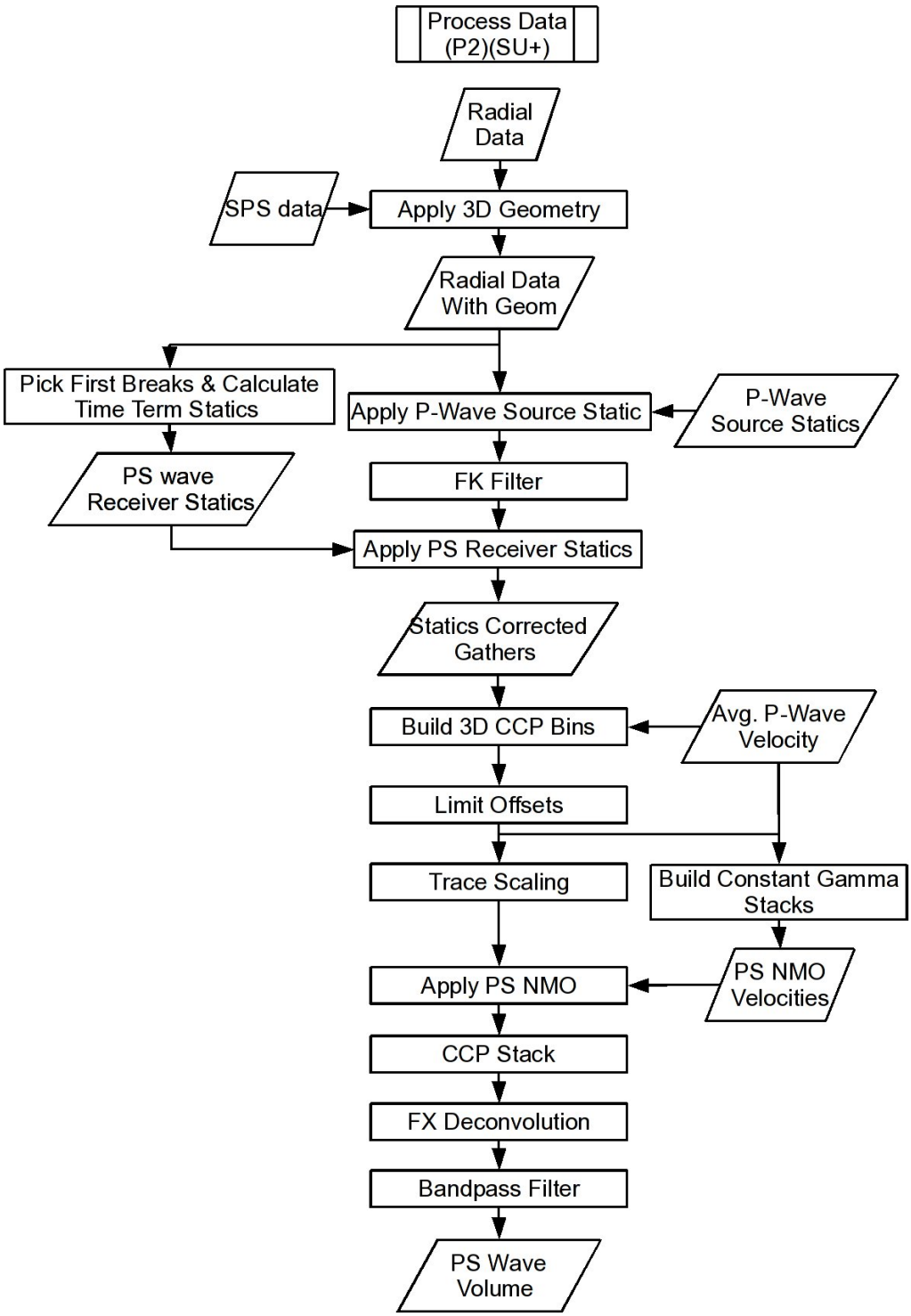

Figure 4.3: Processing flow for the radial PS dataset. This is based on the 2D-PS processing flow. Variations include PS refraction statics and 3D binning. For the transverse component the statics and velocities from the radial component have been applied. The PS data have been processed using Seismic Unix software and specifically designed Velseis software.

4.2 Coordinate rotation

In 2D seismic acquisition the source locations are generally on the receiver line. For 2D-PS acquisition the horizontal geophones are positioned such that one component points in the direction of the line and one is perpendicular. For relatively straight lines most of the PS energy will appear on the inline horizontal component, if there is no fracturing. If there is fracturing the PS wave will split into a fast and a slow wave. The direction of the fracturing can be determined by rotating the coordinate system until all of the slow wave is on one component and all of the fast on the other. For 3D-PS acquisition the horizontal components of the geophones are still positioned in the direction of, and perpendicular to, the receiver line. However, the source points are no longer on the receiver line. This leads to the PS seismic energy being recorded on both components even in environments with no fracturing (Figure 4.4). To account for this, coordinate rotation must be applied to all horizontal traces such that the data are transformed from inline and cross-line sets into radial (the source to receiver direction) and transverse (perpendicular to the radial) datasets (Figure 4.5). The 3D rotated-radial component is analogous to the 2D inline component. Therefore, in a non-fractured environment, most of the PS energy will be recorded on the radial component.

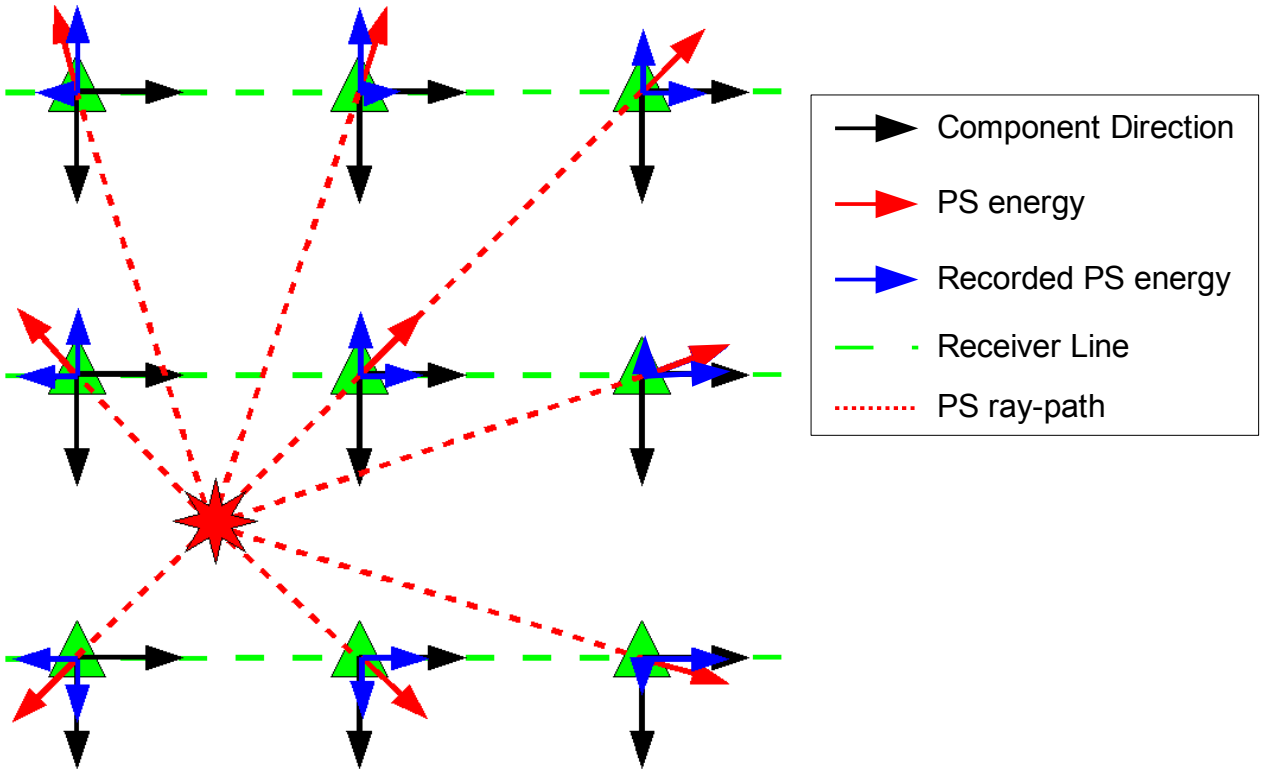

Figure 4.4:Map view of a source and 9 receivers with inline/crossline orientation. The red arrows indicate the direction of the horizontal PS energy. The blue lines show the amount of energy recorded on each component.

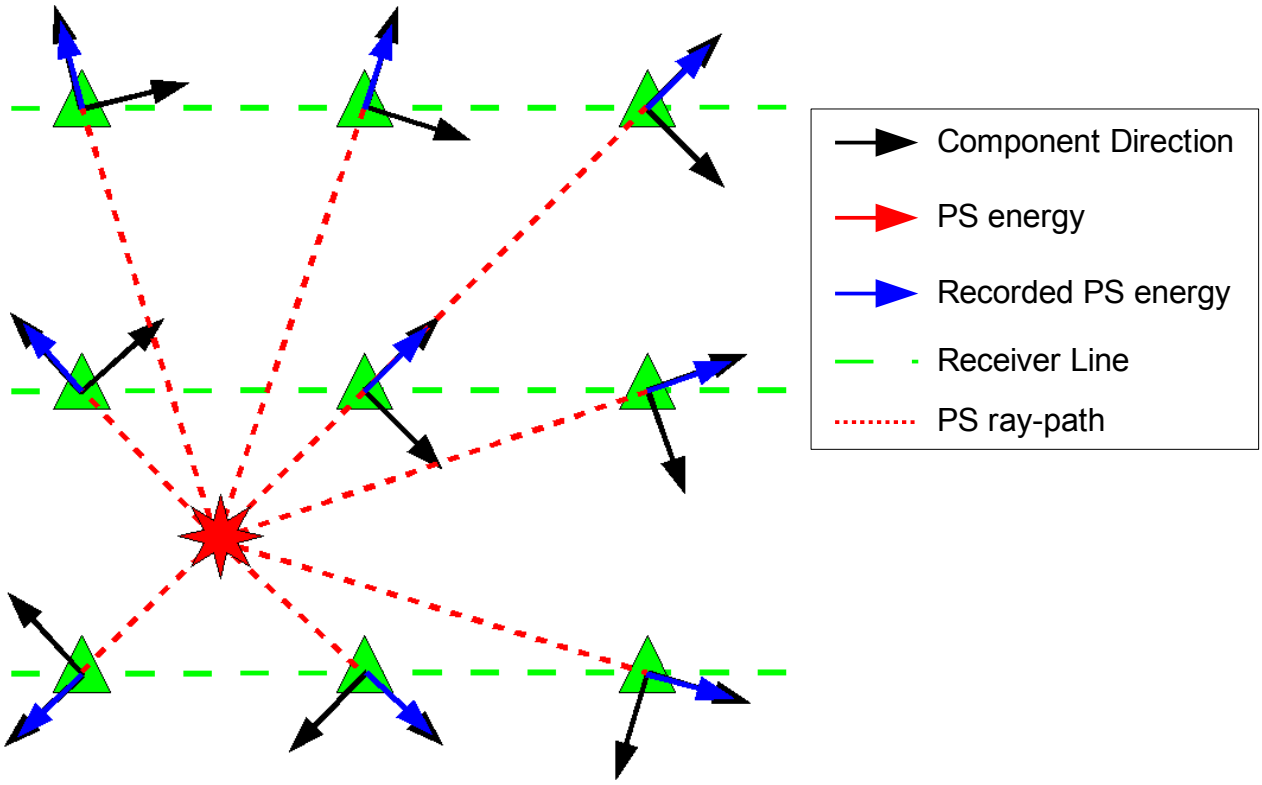

Figure 4.5:After radial/transverse coordinate rotation has been applied to the data from Figure 4.4, all the PS energy is on the radial component. This will be the case for real data if the reflection layer is flat and there is no fracturing along the ray path.

4.3 Groundroll attenuation

As noted in Chapter 3, the ACARP dataset has quite strong coherent groundroll noise. This noise appears as strong linear events on the near traces (Figure 4.6). Ground roll is often created by surface sources and most of the groundroll energy has frequencies less than 30Hz. For conventional P-wave coal-scale data these low frequencies are removed, either at acquisition by using 30Hz geophones or in processing using high-pass filters. It has been demonstrated in the previous 2D ACARP projects that PS waves often have lower frequency content and reduced bandwidth than P waves. This results in a significant part of the PS signal having frequencies less than 30Hz. Therefore, using a simple filter limiting process to remove the groundroll will also damage the desired signal. An alternative is to transform the data to FK space. If the receiver spacing is small enough this separates the groundroll from the signal and allows it to be filtered out. Figure 4.7 shows a representative source record before and after FK filtering. Some noise still remains in the FK filtered record due to the sparse receiver spacing. However, there has been an overall reduction in noise and there is improved continuity of the reflection events.

Figure 4.8 shows preliminary 2D stacked sections from the trial dataset for the filtered and unfiltered cases. The FK filter provides significant improvement in places, but in general the stack exhibits less improvement than was seen on the source records. This is mainly because the PS reflections are stronger on the far offsets which are emphasised in the PS stack. The groundroll noise is primarily on nearer offsets, and tends to be excluded by the prestack offset windowing. Therefore, the primary advantage of using FK filtering is to improve the analysis of the source record in the prestack stages of the processing.

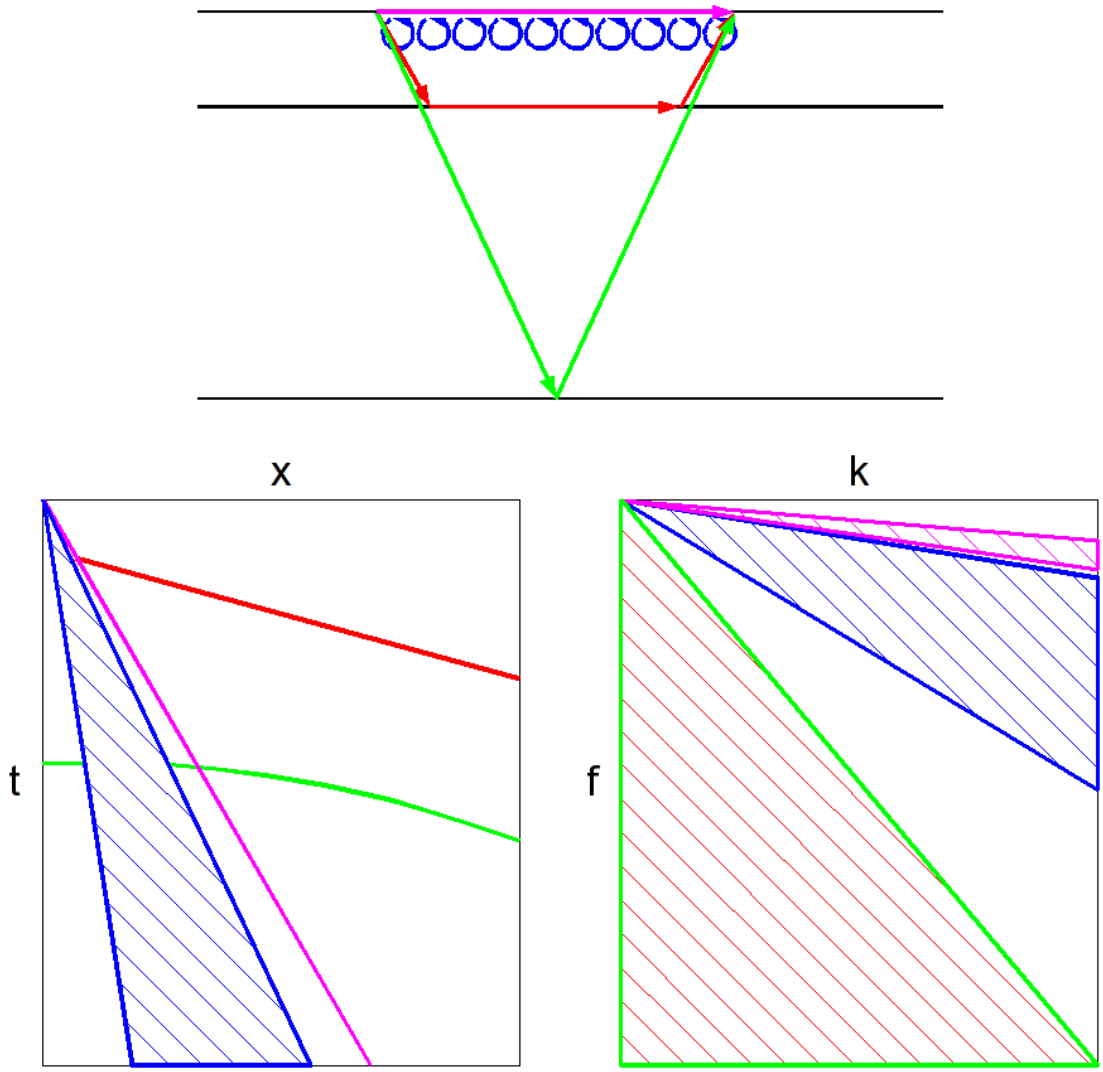

Figure 4.6:Diagrammatic representation of different wave types in seismic data. The top figure shows an earth model with a weathering layer and a single reflector. This image includes a reflected wave (green), a refracted wave (red), a direct wave (magenta) and groundroll(blue). At the bottom left a corresponding seismic gather is displayed. Notice that the groundroll and direct waves interfere with the reflection event at near offsets. Separating these can be difficult. At the bottom right the same record is shown in the FK domain. Here the groundroll and the direct arrivals are separated from the refraction and reflection events (which occur within the green triangle). Therefore, it is possible to filter out a lot of the ground roll energy without degrading the reflection energy.

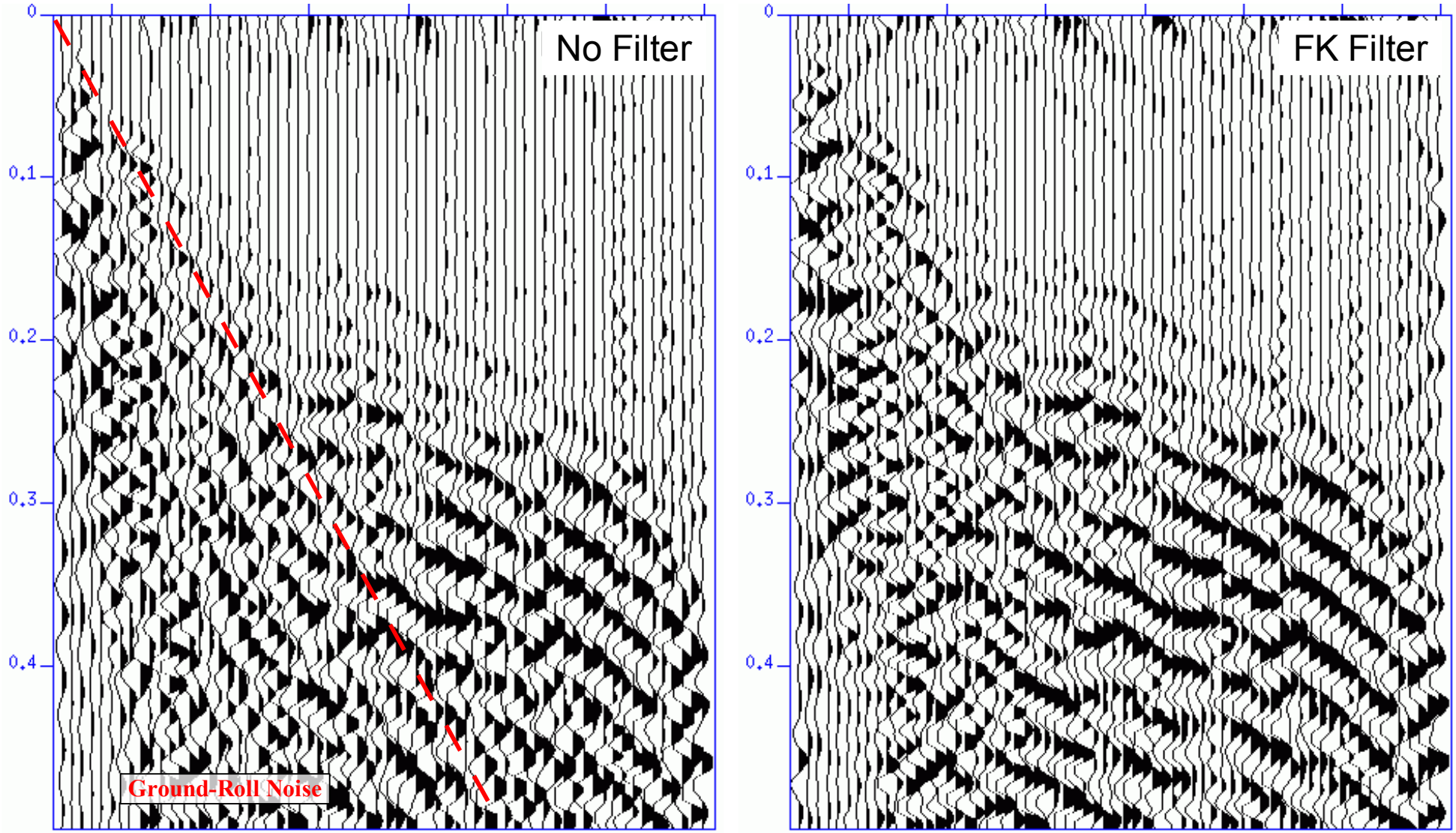

Figure 4.7:Comparison of the PS data with and without FK filtering. For the unfiltered case there is a lot of noise on the near offsets. For the filtered data the noise is reduced and the reflection events on the mid to far offsets are stronger and more coherent.

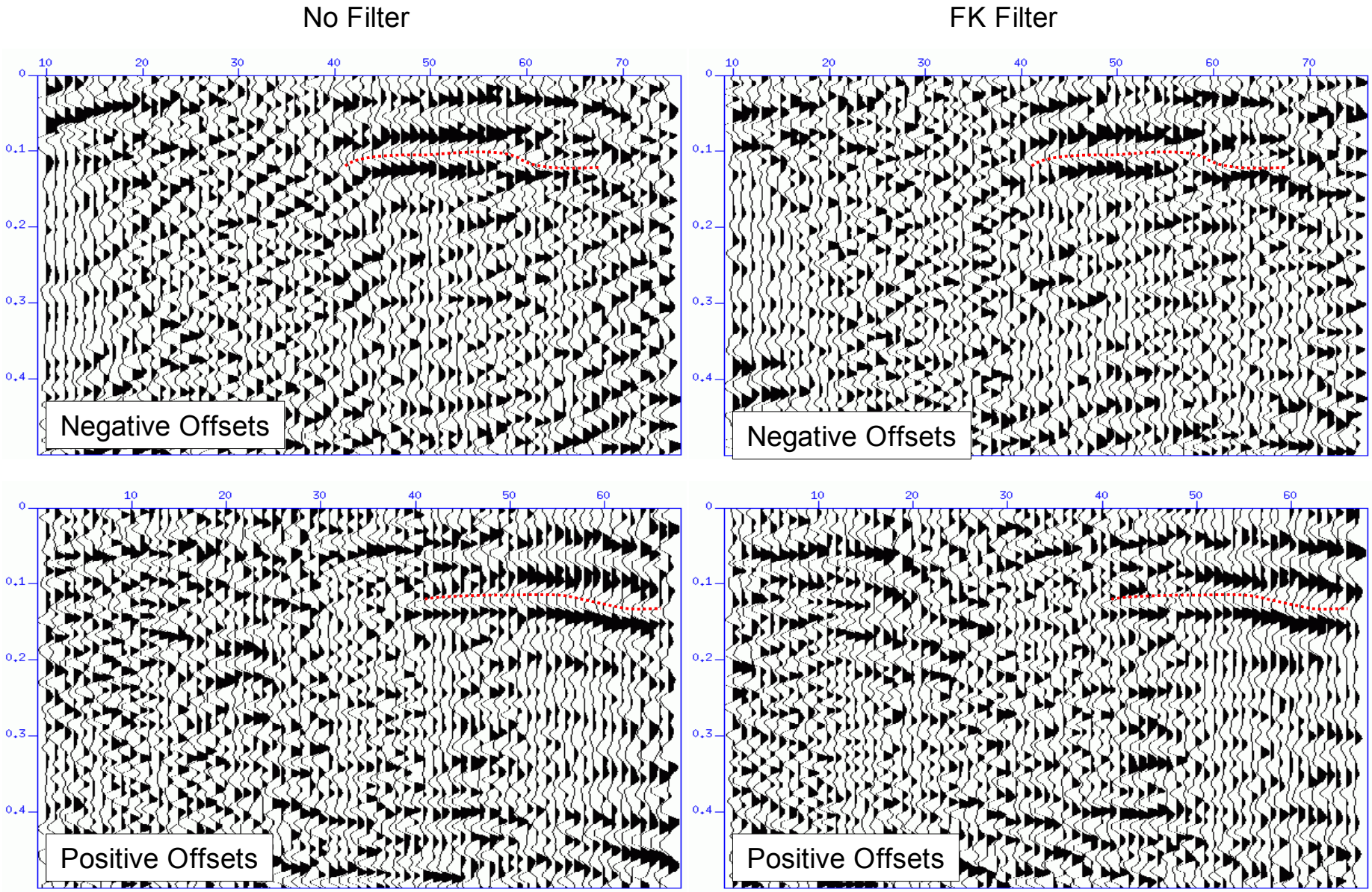

Figure 4.8:Comparison of preliminary 2D stacks from the 3D PS dataset, built from unfiltered and FK filtered gathers. Overall there is very little difference between these images. The FK filtered image may be slightly sharper at the left end of the line where surface conditions were poor.

4.4 Binning

Assuming flat horizons the CDP binning for conventional P-wave data is relatively simple with the reflection point occurring half-way between the source and receiver point. For PS data, the situation is a little more complicated with the position of the reflection point being dependent on the ratio of the P and S-wave velocities, and the depth to the reflection point. There are a number of approaches for approximating this point. These range in complexity from asymptotic binning (depth independent) to dynamic binning (each time sample in a trace may be binned into a different CCP trace). In this trial a horizon-based binning technique has been used. For each source and receiver combination the CCP point corresponding to the depth of the target horizon is calculated. This is the next most complicated approach after asymptotic binning. It is depth dependent on a trace by trace level, but not at the sample level. This is only appropriate for single (or closely spaced) target reflection, as it tends to optimally focuses the image at a nominated target depth.

Based on the design stage of this project (Chapter 2) CCP bins each having a dimension of 15x30m have been constructed. The grid has been orientated in the same direction as the receiver lines.

4.5 PS Velocity Analysis and NMO

For the initial velocity analysis we have assumed that there are no variation of the velocities with azimuth. The viability of this will be discussed in Chapter 7. Given this assumption, the standard 2D-PS NMO algorithm can be applied to the binned 3D-PS data. Good stacked images have been generated by using the average P-wave rms-velocity at the target (approximately 3200m/s) and a Vp/Vs ratio (γ) of 2.0.

4.6 Conclusion

Seismic processing is the most time consuming and difficult stage of a converted-wave project. While 3D PS processing is generally more difficult than in the equivalent 2D case, this chapter has demonstrated that many of the 2D PS processing algorithms can be modified to achieve good results.

5 Receiver Statics

5.1 Introduction

One of the most difficult steps in the PS processing sequence is determining the S-wave receiver statics. This has been an important component of both of the previous 2D ACARP investigations and continues to be for the 3D investigation.

Statics are time delays caused by variations in the weathering layer and changes in source and receiver elevation. These time errors cause traces that are to be combined in the stacking process to be misaligned. This introduces smearing, and hence loss of continuity and resolution on the stacked images. For PS data the general approach for removing these statics is to first apply the P-wave source static correction to the data, and then calculate and apply the S-wave receiver static correction.

The importance of this processing step can be demonstrated by looking at the conventional P-wave data. A key part of this investigation is to examine the affect of azimuthal variations in the earth. One method of investigating this is to stack the data into a number of azimuthally limited volumes, and compare the picks from a target horizon. Figure 5.1 shows the horizon picks from Inline 112 for five azimuthally limited P-wave volumes. These are for data generated using an optimal refraction based receiver statics solution (Figure 5.1a), and a simple elevation statics method (Figure 5.1b). For the case where a good statics correction has been applied (as in the refraction case) it can be seen that there is very little difference between the different azimuths for most of the length of the line. This suggest that there is unlikely to be any real P-wave azimuthal variations in the data. If the simpler elevation statics solution is applied there is some apparent variation of the seismic image with azimuth on the left half of the image. This is to the south of the survey area and corresponds to the region of the black soil weathering layer where the elevation statics solution would be expected to be poorer than the refraction solution. These results demonstrate that small errors in the statics solution can lead to misinterpretation in the later stages of the processing.

In the example given here the surface-related errors could easily be misinterpreted as real azimuthal variations in the properties of rocks at depth.

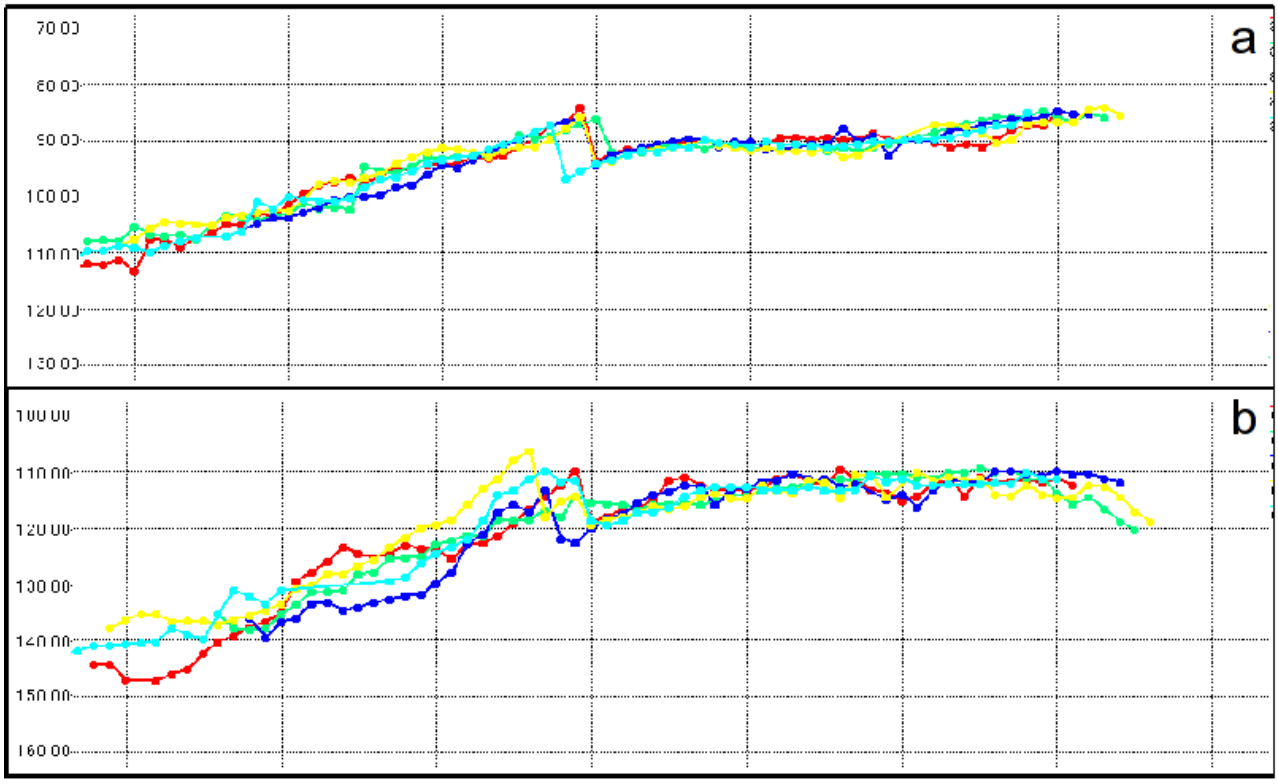

Figure 5.1:Target horizon picks for 5 azimuth limited P-wave stacks (Line 112). (a) displays the case where a good refraction statics solution has been applied. This suggests that there is no variation of the P-wave based on ray-azimuth direction. However if an incorrect statics solution is applied such as elevation statics (b) a pseudo-azimuthal effect is apparent, particularly where the the weathering conditions are poor (left end of line).

5.2 PS Residual Statics

The standard method that has been developed to calculate the receiver statics in our 2D-PS work is based on the P-wave residual statics approach. For the conventional P-wave method static error is assumed to be a linear function of time errors associated with the sources, receivers, structure (cdp location) and normal moveout. For this technique reflection horizons are picked on CDP gathers. This is usually done automatically by using correlation algorithms to compare the gathers with brute stacks. Once the horizons are picked, a mathematical technique called least-squares inversion can be used to separate the error into its individual parameters. To perform the inversion we use the Singular Value Decomposition (SVD) algorithm.

For PS data the conventional technique is difficult to implement since CCP binning requires a good understanding of velocities. However, velocities are more difficult to determine for PS data due to a lower signal-to-noise ratio and larger statics. Therefore, a modified residual statics method has been developed.

The first big difference is that the reflection horizons are manually picked in the receiver domain. For the 2D case, limited-offset receiver-domain stacks are picked. This allows the general RMS velocity to be calculated during the process and removes the need for the application of an accurate NMO solution before statics calculation.

Since PS processing is usually conducted in conjunction with conventional P-wave surveys, the P-wave source static correction is applied to PS data before statics calculation. Therefore, the PS static error can be parameterised into receiver, structural, and offset contributions. Further technical detail is given in the Appendix (Section 11.2)

As introduced in Chapter 1, in 2D-PS surveying it it common to separate the positive and negative offsets and process these separately. Sometimes this includes calculating separate statics solutions. For the 3D case this corresponds to grouping traces according to source-to-receiver azimuth direction. In keeping with this idea, for the 3D PS data, the reflection horizons have been picked on offset and azimuth limited receiver stacks. Figure 5.2 shows the calculated receiver statics for two representative azimuth directions. This figure suggests that receiver statics are dependent on azimuth angle and can be quite variable. However, theory suggests that this is unlikely to be the case. For low-velocity weathering layers the seismic rays are travelling near vertically in the vicinity of the receiver. This is likely to result in rays from different azimuths travelling through similar paths and therefore having similar receiver statics solutions. This leads us to question if the method is working as expected.

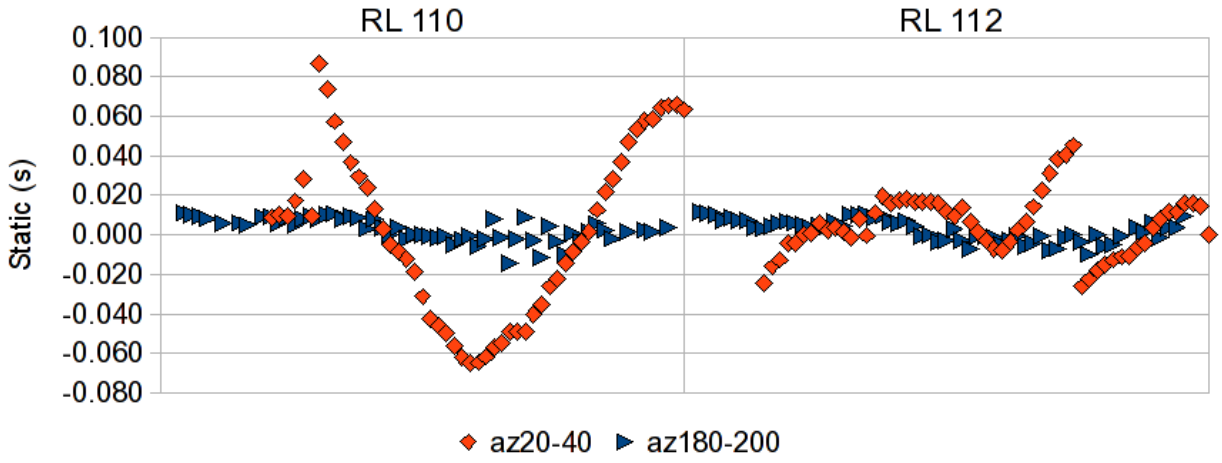

Figure 5.2: Example of the variation in the residual statics solution for different azimuth limited datasets.

To determine if the method is working correctly let us consider only the azimuths that give similar

receiver statics solutions (Figure 5.3). If a receiver statics solution was derived using the horizon picks from all these azimuths we would expect the solution to have a similar trend to the average of the individual solutions. However, as is demonstrated in Figure 5.4 the combined receiver statics solution is very different. This is an example of non-uniqueness in the least-squares inversion. In this case it is caused by parameter leakage between the structure and receiver components where some of the error associated with the structure of the reflection is interpreted as a receiver static. These problems are significant and suggest that another method needs to be investigated to calculate the statics for this 3D PS dataset.

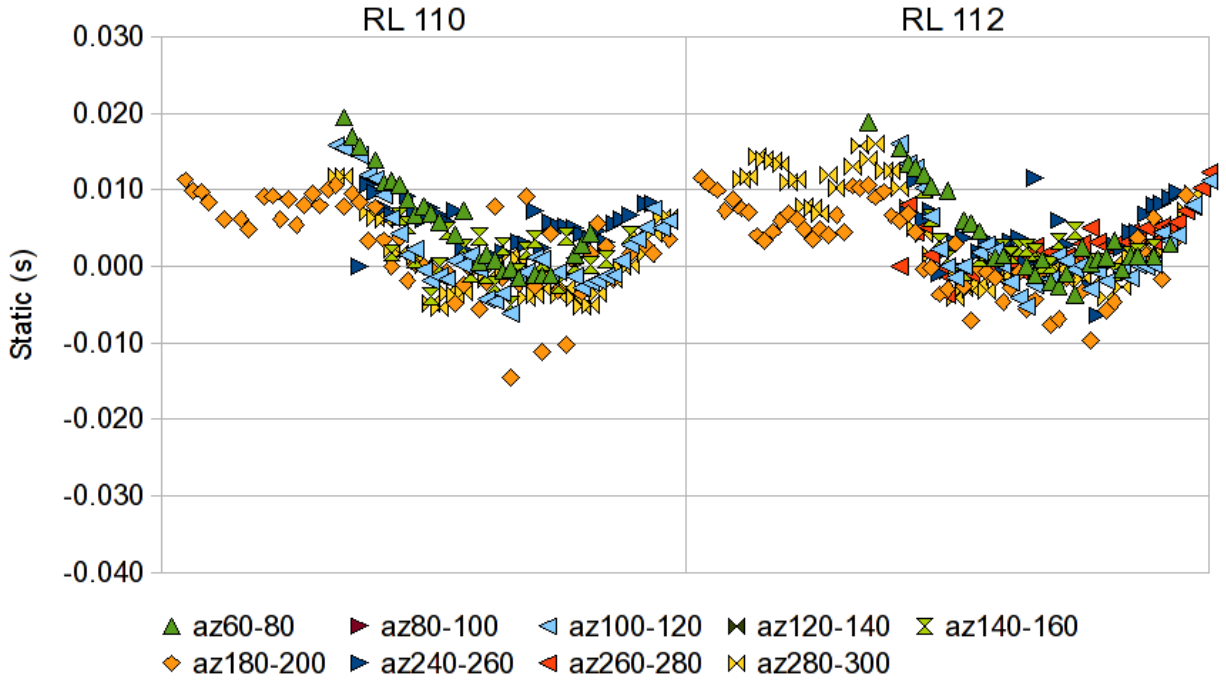

Figure 5.3:9 azimuthally limited residual receiver-statics solutions that display similar properties.

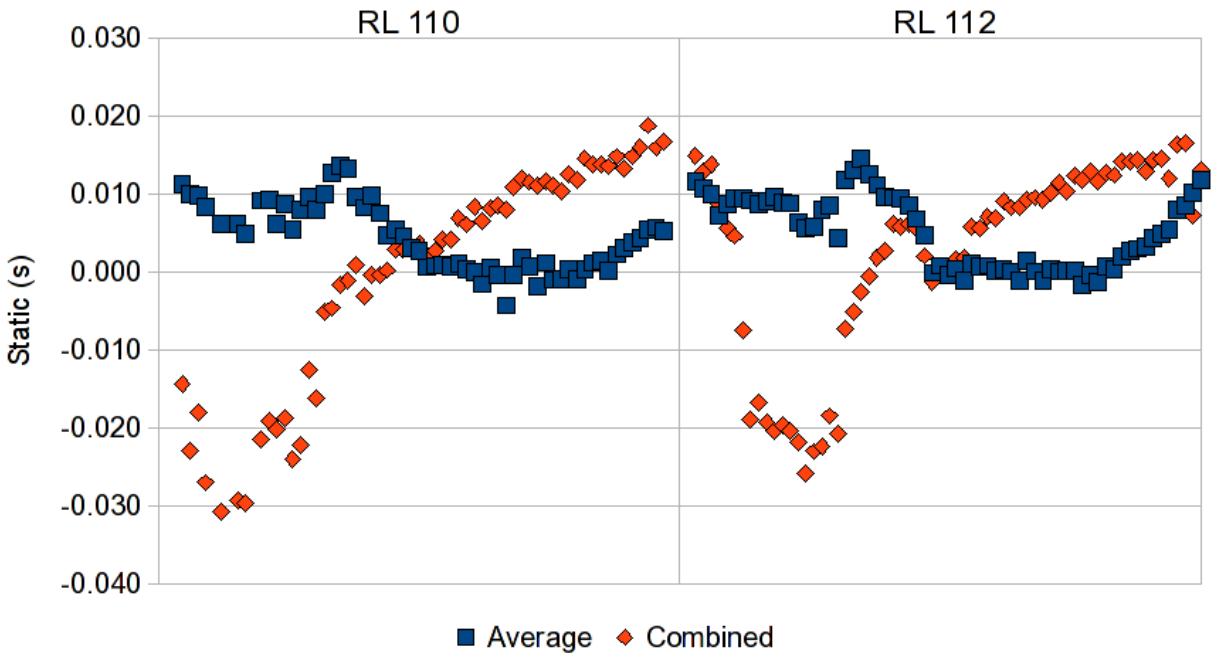

Figure 5.4: Comparison of the average solution from the residual statics in Figure 5.3 versus a solution incorporating all the input data from each of the curves in Figure 5.3. It is expected that these should give similar solutions. However, significant variation is observed due to non-uniqueness and parameter leakage between the CCP and receiver contributions.

5.3 Elevation Statics

When testing new processing methods it is important to compare the results against a reference technique. Figure 5.5 shows two possible choices for such a reference. Figure 5.5(a) shows a section constructed using optimal source statics (from P-wave refraction analysis) but no receiver statics. Figure 5.5(b) shows a second option where elevation statics only, have been applied to both sources and receivers. This approach corrects for lateral variations in surface elevation, but it assumes a constant weathering profile. The elevation-statics correction is easily implemented and can provide reasonable results if the weathering layer is simple with little variation. The elevation statics image in Figure 5.5(b) has a more realistic long wavelength structure and shows reasonable continuity of the target seam. There is a slight reduction in the quality of the reflector on the elevation statics image toward the left side of the line. This corresponds to the black soil region where the elevation statics solution is expected to be poorer. The elevation statics reference will be used in the comparisons to follow.

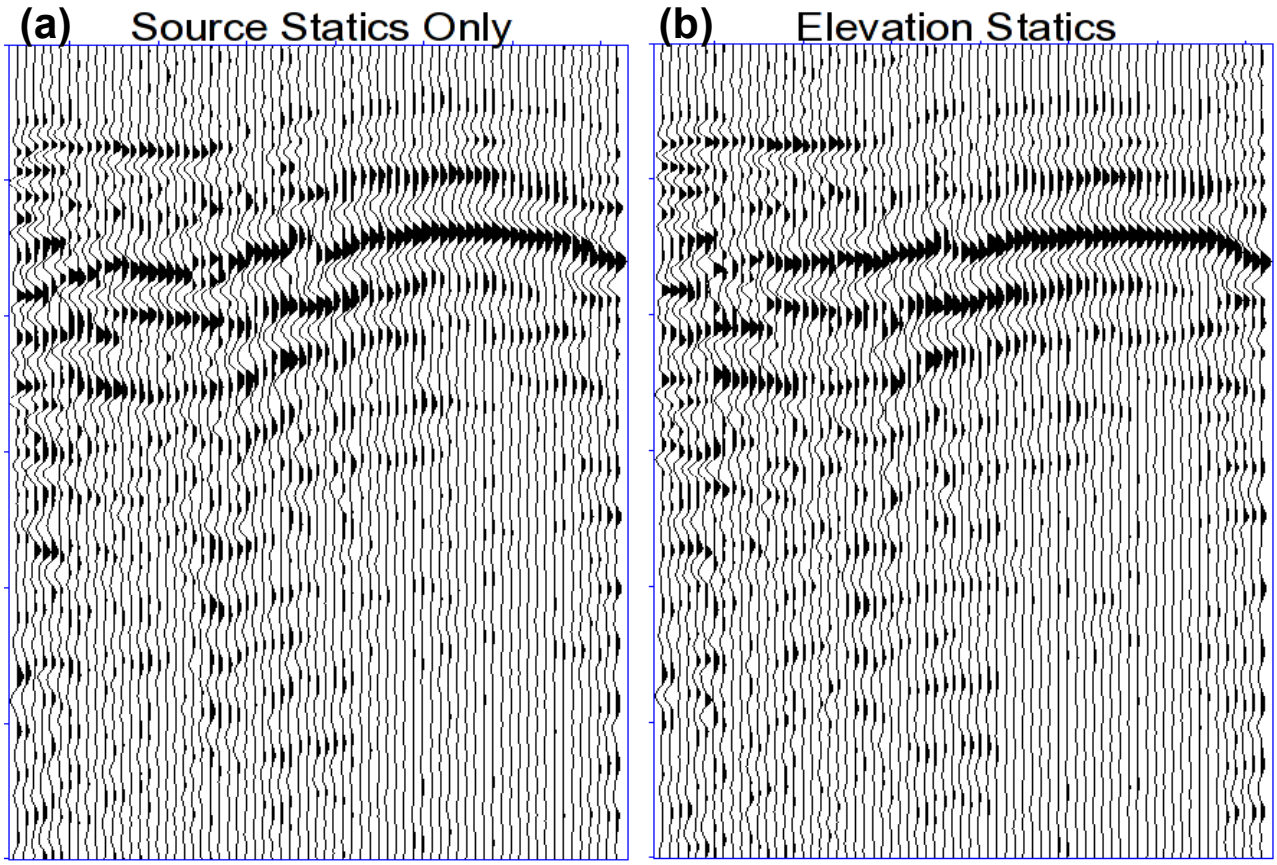

Figure 5.5: Stacked sections from Line 110 for source statics only (a) and elevation statics (b). These simple statics methods produce reasonable images that are useful when comparing more advanced methods. The elevation statics solution will be used as a reference in the following figures, as it has a more realistic long-wavelength structure and good reflector continuity.

5.4 Robust Statics

The so-called robust statics method is a simple processing technique that has been developed for this project. It utilises the receiver-domain horizon-picks that were selected for the residual-statics approach. The aim of this approach is to use robust statistical methods such as median filters and averaging to subtract the long-wavelength components from the picks, leaving the short-wavelength receiver statics. A key assumptions of this process is that short-wavelength structural terms are cancelled out by the averaging process. This tends to be true if the fold of the data is high, and if we err on the side of caution and only extract the short-wavelength data. It is also assumed that the short-wavelength receiver statics are not azimuthally varying which is reasonable for low velocity weathering layers. The long-wavelength component contains both structural and receiver terms which cannot be separated. Therefore, the aim of this approach is to improve the stack quality. It may not give a fully corrected structural image. However, it may be possible to accommodate for

this shortcoming by tying the stacked reflection events to borehole data. Further technical detail on the robust statics algorithm and a synthetic example, are given in the Appendix (Section 11.3.1).

Figure 5.6 compares the stacked section of line 110 for the elevation and robust statics methods. It is clear that the elevation statics solution has better long wavelength character but the robust statics image has improved continuity of the reflector especially toward the left end of the line (black soil region).

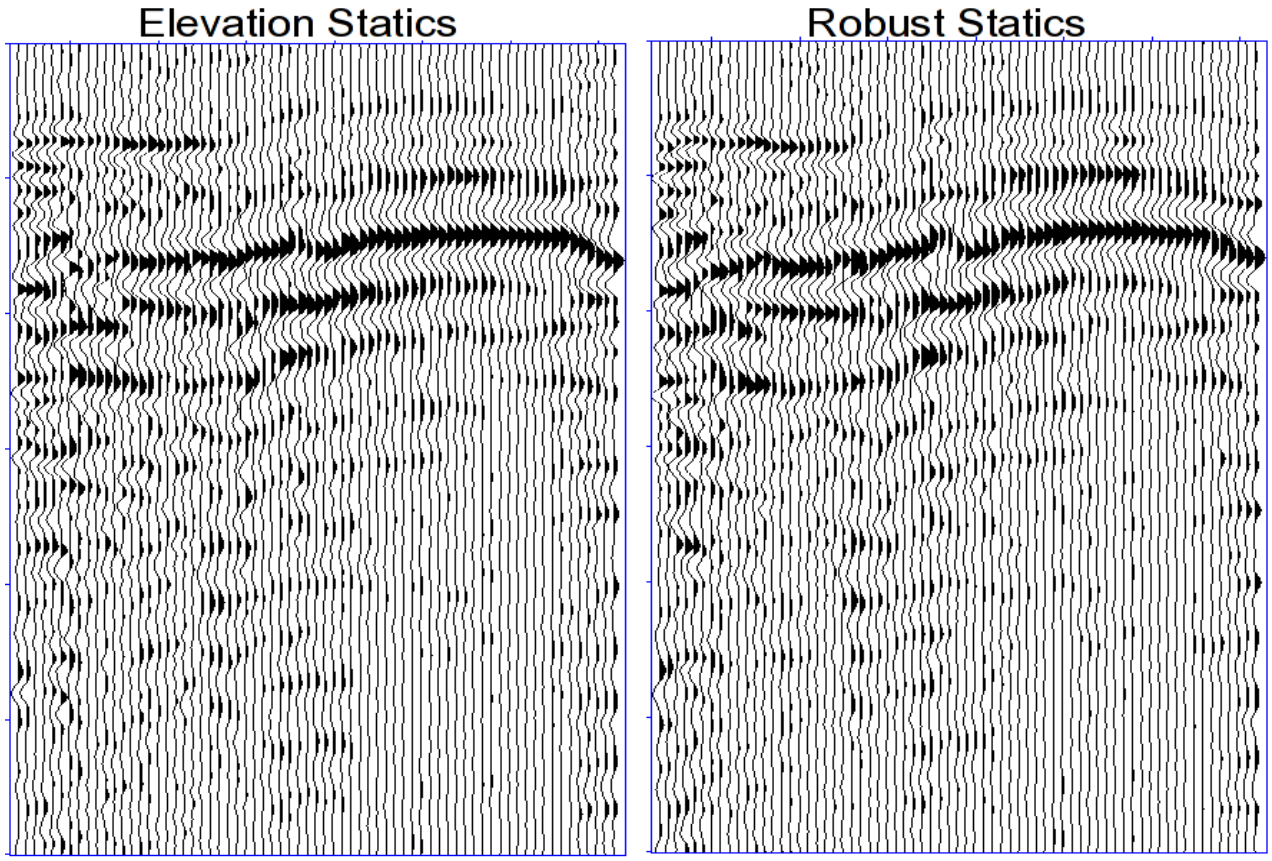

Figure 5.6: Comparison of Line 110 stacked with elevation and robust receiver statics. The elevation statics has better long-wavelength structure. However, the robust method gives better continuity especially toward the left where the weathering conditions are poor.

5.5 PPS Refraction Statics

The standard method for calculating the statics in conventional P-wave processing is to analyse the PPP refraction event (Figure 5.7). A standard reversed-spread refraction interpretation allows source and receiver statics corrections to be determined. For P-wave data this is generally the first arrival and is a quite strong event. For PS data the corresponding concept is to pick the PPS refraction (Hean and Meulenbroek, 2011; Meulenbroek and Hean, 2011). This event is generated

by conversion of the horizontally travelling P headwave to an upward travelling S wave (Figure 5.7). Since the S wave is slower than the P wave, the PPS refraction is generally not the first arrival. In conjunction with this the strength of the PPS refraction can be quite variable. These factors often make the PPS wave difficult to identify.

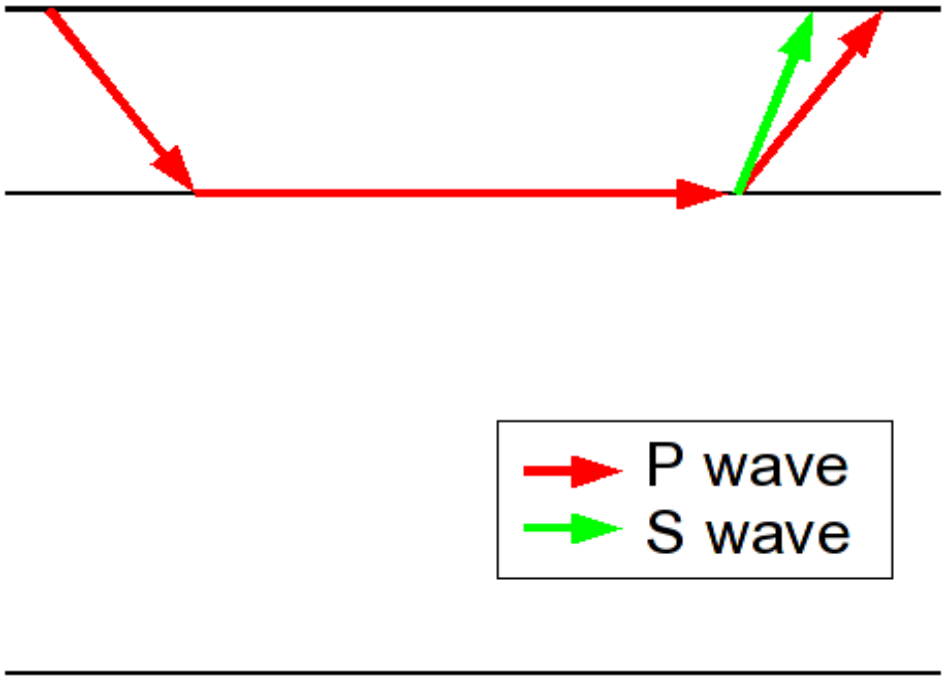

Figure 5.7: Raypath diagram showing the conventional PPP refraction and the PPS refraction

For shallow 2D-PS surveys this technique is generally avoided as there are often not enough picks to give an accurate solution. This is especially true for surface sources where surface waves tend to swamp much of the PPS energy. For high fold 3D surveys there is much more data, so even a small number of picks on each record can lead to a viable number of picks for the statics calculation. Figure 5.8 shows the PPS refraction picks for some representative records. These figures indicate the difficulties in picking the refraction.

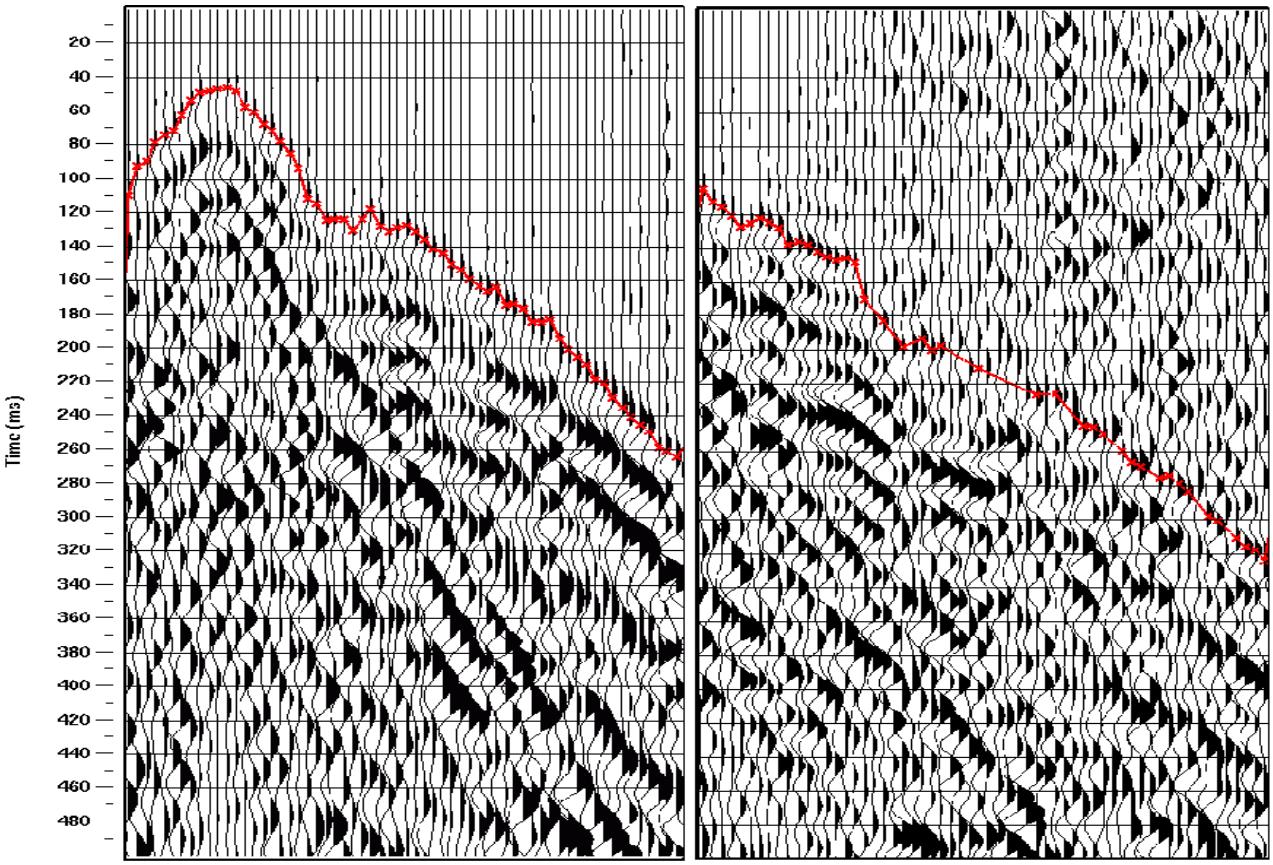

Figure 5.8: Representative source records showing the PPS refraction event. The refraction event is often difficult to pick due to noise and large variations associated with large S-wave receiver statics.

For this investigation we have used the time-term method to extract the receiver statics (Reiter, 1970). This assumes that the time of each refraction pick is a function of a source time (t_s), a receiver time(t_r), and an offset time where the offset time is defined by the distance (d_k) divided by the velocity (v_k) for a number of velocity bins that the ray travels through.

$$t = t_s + t_r + \sum_{k=0}^{n} \frac{d_k}{v_k}$$

Singular value decomposition is used to separate the individual components. Further technical detail is given in the Appendix (Section 11.3.2).

Solving for these times without constraints tends to give some anomalous velocities which create small errors in the receiver responses. The results have been improved by constraining anomalous velocities to the average velocity. An interesting numerical problem that arose was that the distance and velocity values, measured in m and m/s, are much bigger than the other components and were

dominating the solution. To remove this problem it was necessary to normalise the data by using units of km and km/s.

The receiver statics are approximately proportional to a constant multiplied by the receiver time-term. For this investigation the constant has been assumed to be close to one. Therefore, the receiver static is equal to the time-term. The receiver statics shown in Figure 5.9 have been derived for 60x60m velocity bins. The receiver statics appear to be smaller than would be expected for PS data. This suggests that the method may need further constraints or a closer investigation of the relationship between the time-term and the static.

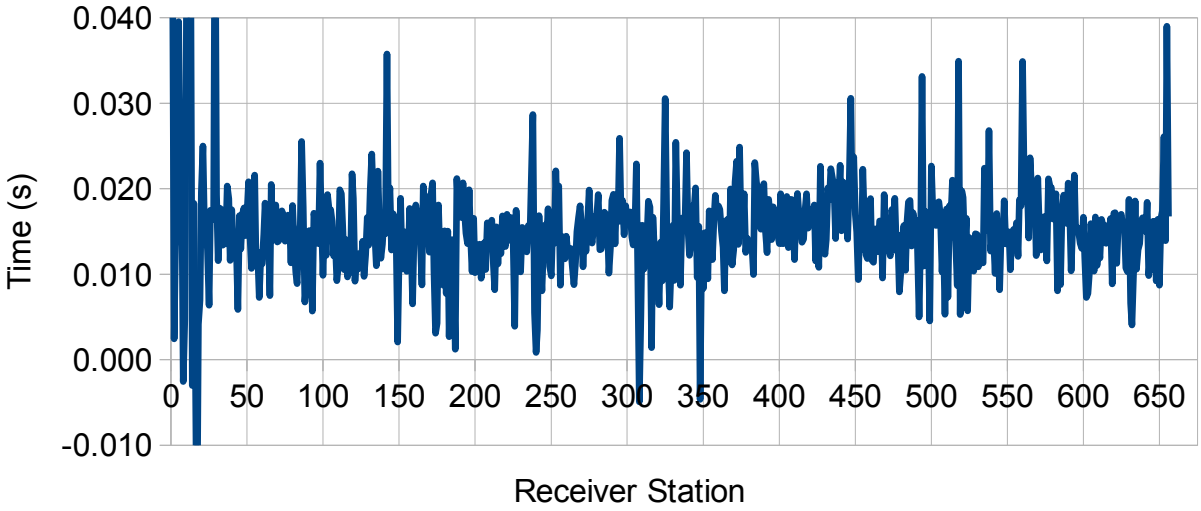

Figure 5.9: The receiver statics solution derived from the time-term refraction method. Generally the statics solution varies between 2ms and 20ms for this dataset.

In Figure 5.10 the time-term receiver statics correction has been applied to the data. The PS refraction solution shows a good long wavelength structural behaviour and generally has a slightly improved reflector continuity over the image with elevation statics correction.

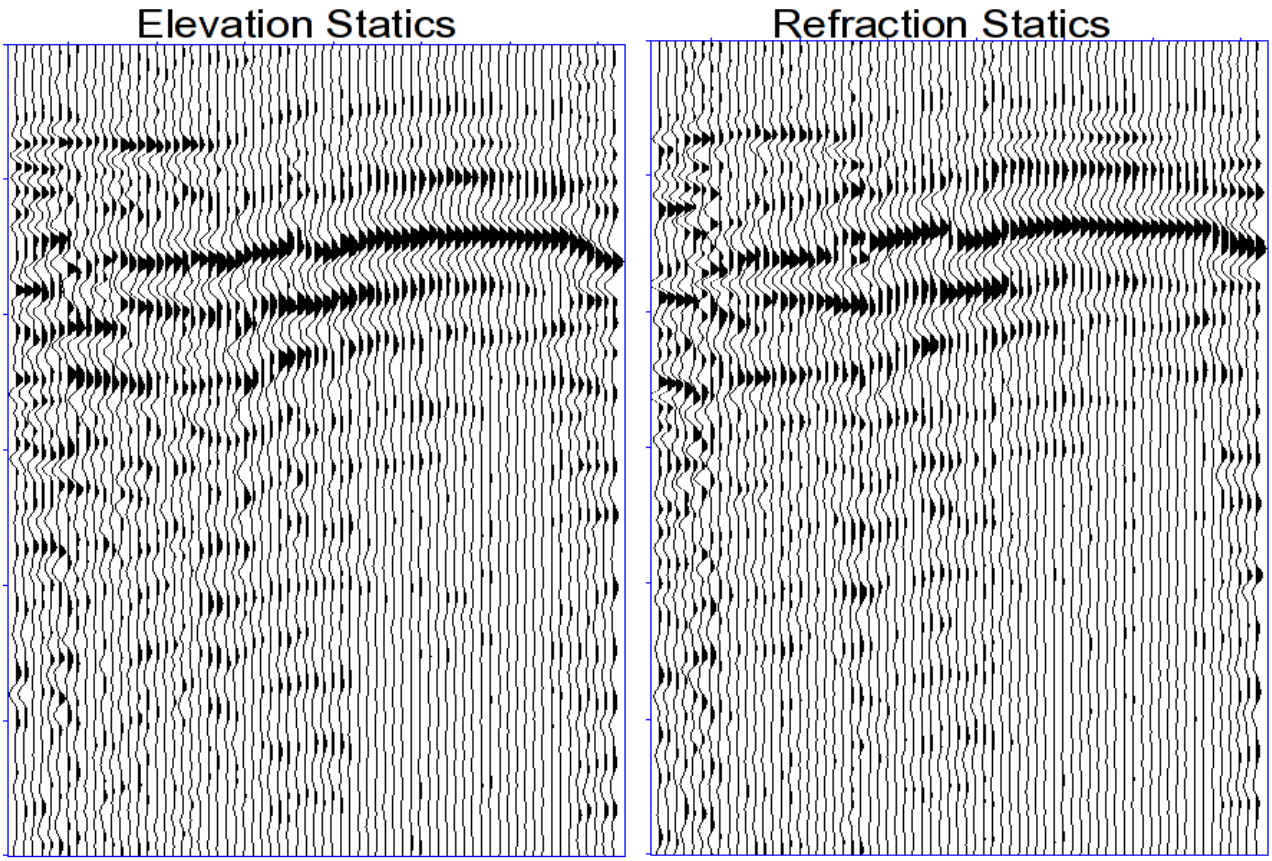

Figure 5.10: Comparison of line 110 stacked with elevation statics and time-term PPS refraction statics. The refraction image has good long-wavelength structures and good seam continuity.

5.6 Discussion

A critical element in PS-wave processing is determination of the S-wave receiver statics. This investigation has shown that under certain conditions the residual statics approach can result in erroneous statics solutions. In such cases elevation, robust statistical, or refraction statics can be used to process the data. Each has its own restrictions and limitations and generally only provides a partial correction to the data.

We have carried out detailed comparisons of the different statics solutions over the full data volume. Based on this, we believe that the PPS refraction statics solution generally provides the most consistent receiver statics. This technique has been implemented for the remainder of the figures in this project.

6 Interpretation

6.1 P and PS Stacked Data Volumes

Figures 6.1-6.4 show inline sections from the final P and PS stacked volumes with the P-wave images at the top and the corresponding PS images at the bottom. There are double the number of P-wave images since the P data were binned using 15x15m bins and the PS data with 15x30m bins. As is standard practice on integrated P+PS presentations, the images have been scaled to show equivalent depth extents. Plotted over the images is the preliminary interpretation showing the target coal seam in green and possible faulting in red.

The P-wave data show a good reflection at the coal-seam with good frequency content. The overall structure tends to dip toward the southerly direction (left of the images). The large reverse fault identified on the earlier 2D P-wave data is present across the entire extent of the survey and the throw of this fault appears to become less significant for the more easterly sections (low inline number). The images also indicate the possibility of further reverse faulting, trending the same direction as the main fault. These become more numerous at the eastern side. This fault behaviour suggests that over the extent of the survey a single large fault plane is becoming more complicated and is breaking up into a number of smaller faults.

As is expected the PS images have higher noise levels especially toward the south of the survey, in the region where the black-soil weathering layer is present. The PS images also have a lower frequency content. This frequency behaviour has been seen in the 2D-PS investigations and has been attributed to higher attenuation effects of the S wave by the earth. Despite these factors the images show quite a good response to the target coal seam. These images compare well with previous 2D-PS coal-data and represent one of the better datasets collected with surface sources.

The PS data have a similar overall structure to P, dipping towards the south. However there may be some error in the long-wavelength character. This may be due to errors in the long-wavelength statics solution. The large fault at the centre of the survey is well defined on the PS data and a smaller one to the north of this on the eastern lines also agrees well with the P data. South of the main fault the interpretations for the P and PS images are slightly different. For the P data the faulting is reverse and upthrown to the south. For the PS data the faulting is also reverse, but it is upthrown to the north. This will be discussed further in the integrated interpretation (Section 6.3).

Figure 6.5 gives a map-view comparison of the horizon picks for the P and PS data. These images tend to confirm the general structure of the stacked sections with the target coal seam dipping toward the south. These images also suggest that the degree of dipping increases for the more easterly lines.

While the horizon images do indicate the region of the main fault, they are generally not ideal for pin-pointing the location of faults. Figure 6.6 displays the map of the gradient attribute. This plots the maximum gradient of the target horizon at each reflection point. These images clearly define the main fault and the secondary one to the north. The PS image is noisier than the P, particularly toward the south. The PS image does, however, provide good confirmation of the P data for these faults.

A more in-depth PS attribute investigation is presented in the next section (Section 6.2).

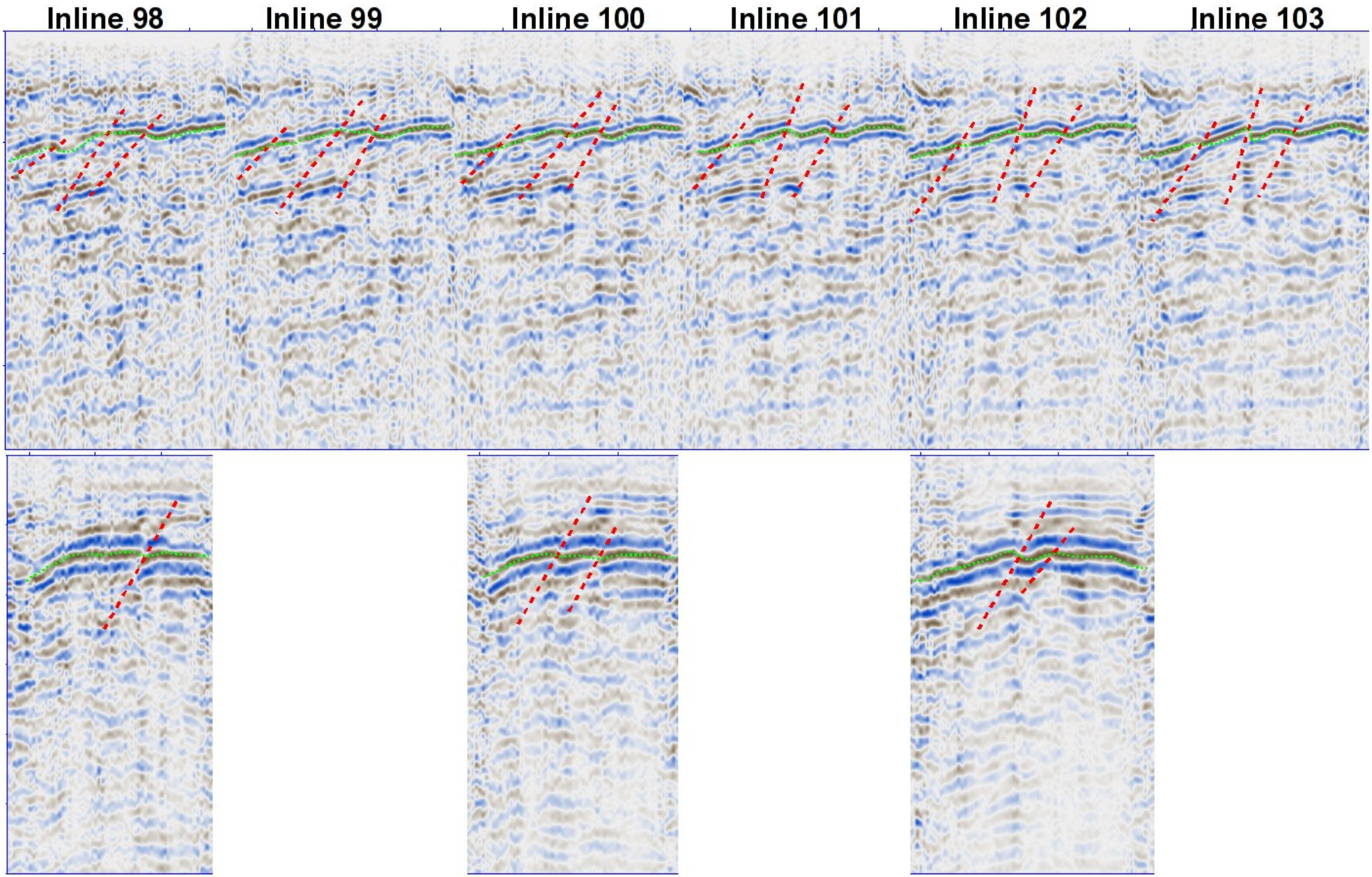

Figure 6.1: Inline sections (lines 98-103) from the P (top) and PS (bottom) volumes. In this and the following figures, the vertical axis is the reflection time, with a total scale of 0.375 s and 0.6s on the P and PS sections respectively. The depth extent is approximately the same on the P and PS sections. The target coal seam interpretation (green) and possible faulting (red) is included. There are fewer PS sections since The P data bin size is 15x15m while the PS bin size is 15x30m. Both volumes have good data quality

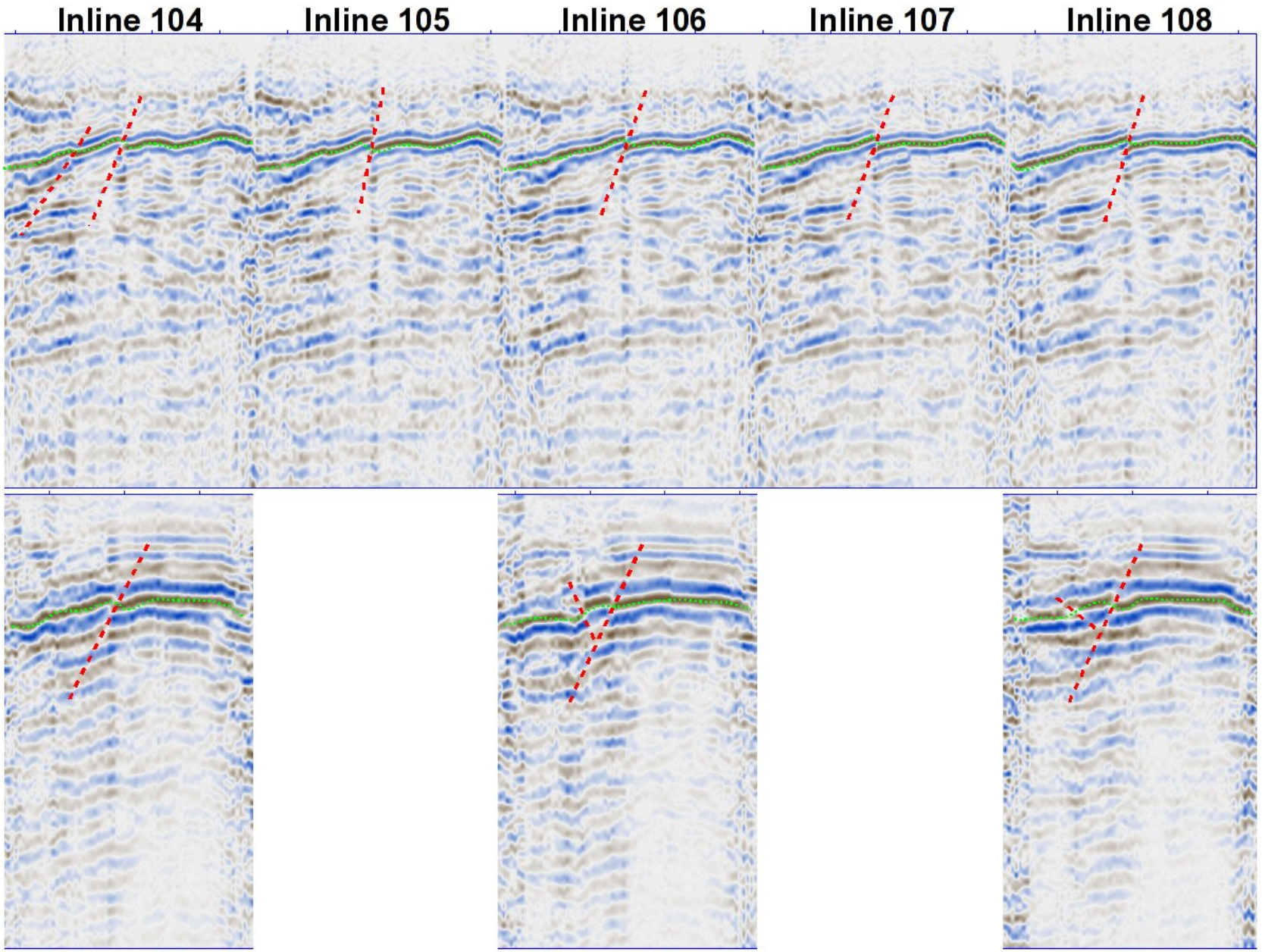

Figure 6.2: Inline sections (lines 104-108) from the P (top) and PS (bottom) volumes. The target coal seam interpretation (green) and possible faulting (red) is included. There are fewer PS sections since The P bin size is 15x15m while the PS bin size is 15x30m. Both volumes have good data quality.

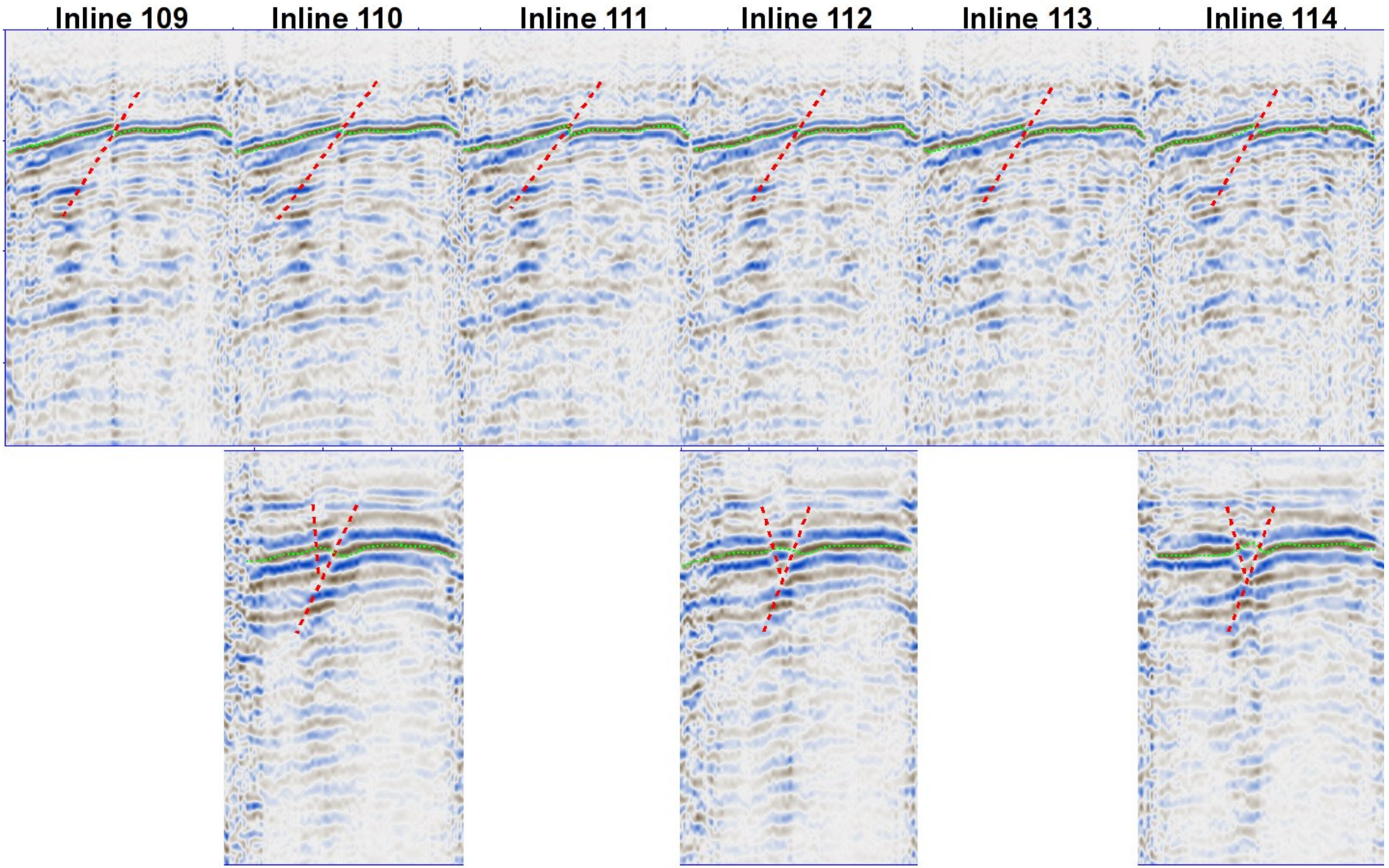

Figure 6.3: Inline sections (lines 109-114) from the P (top) and PS (bottom) volumes. The target coal seam interpretation (green) and possible faulting (red) is included. There are fewer PS sections since The P bin size is 15x15m while the PS bin size is 15x30m. Both volumes have good data quality.

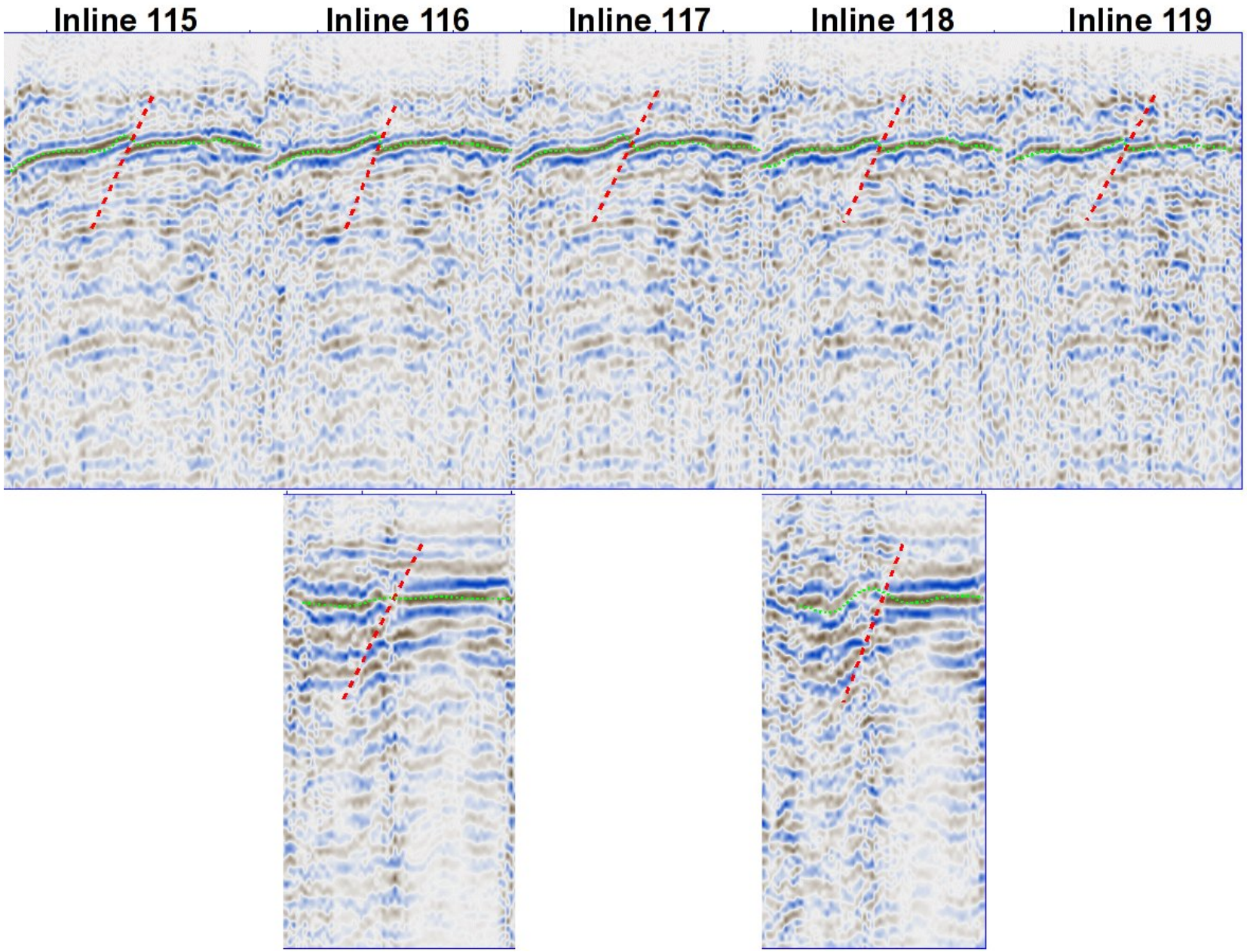

Figure 6.4: Inline sections (lines 115-119) from the P (top) and PS (bottom) volumes. The target coal seam interpretation (green) and possible faulting (red) is included. There are fewer PS sections since The P bin size is 15x15m while the PS bin size is 15x30m. Both volumes have good data quality.

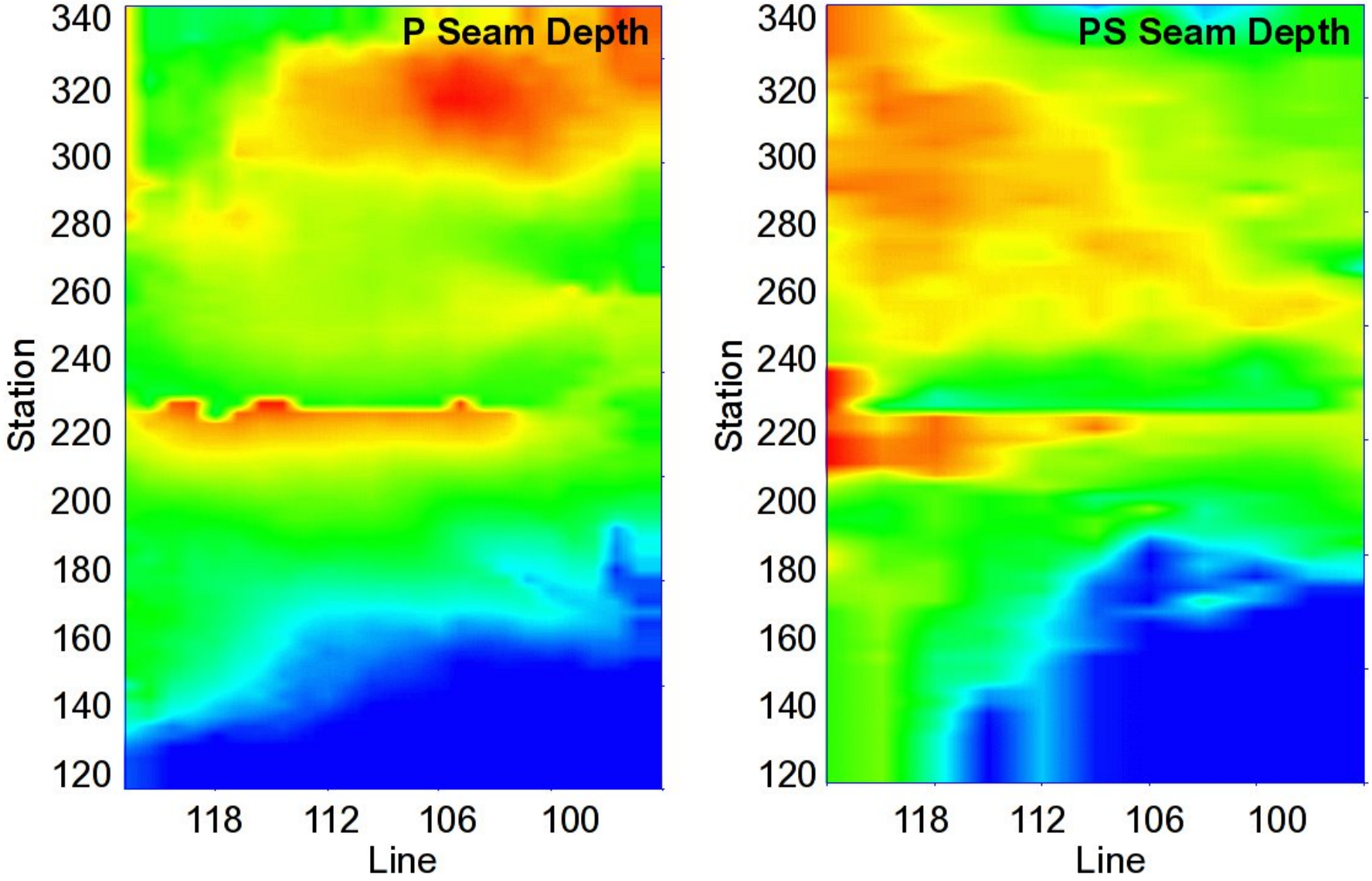

Figure 6.5: Map view of the horizon picks from the target seam for the P and PS data. Red represents shallower data and blue deeper. The variation near Station 225 is due to the large fault that has been interpreted in previous 2D P-wave data.

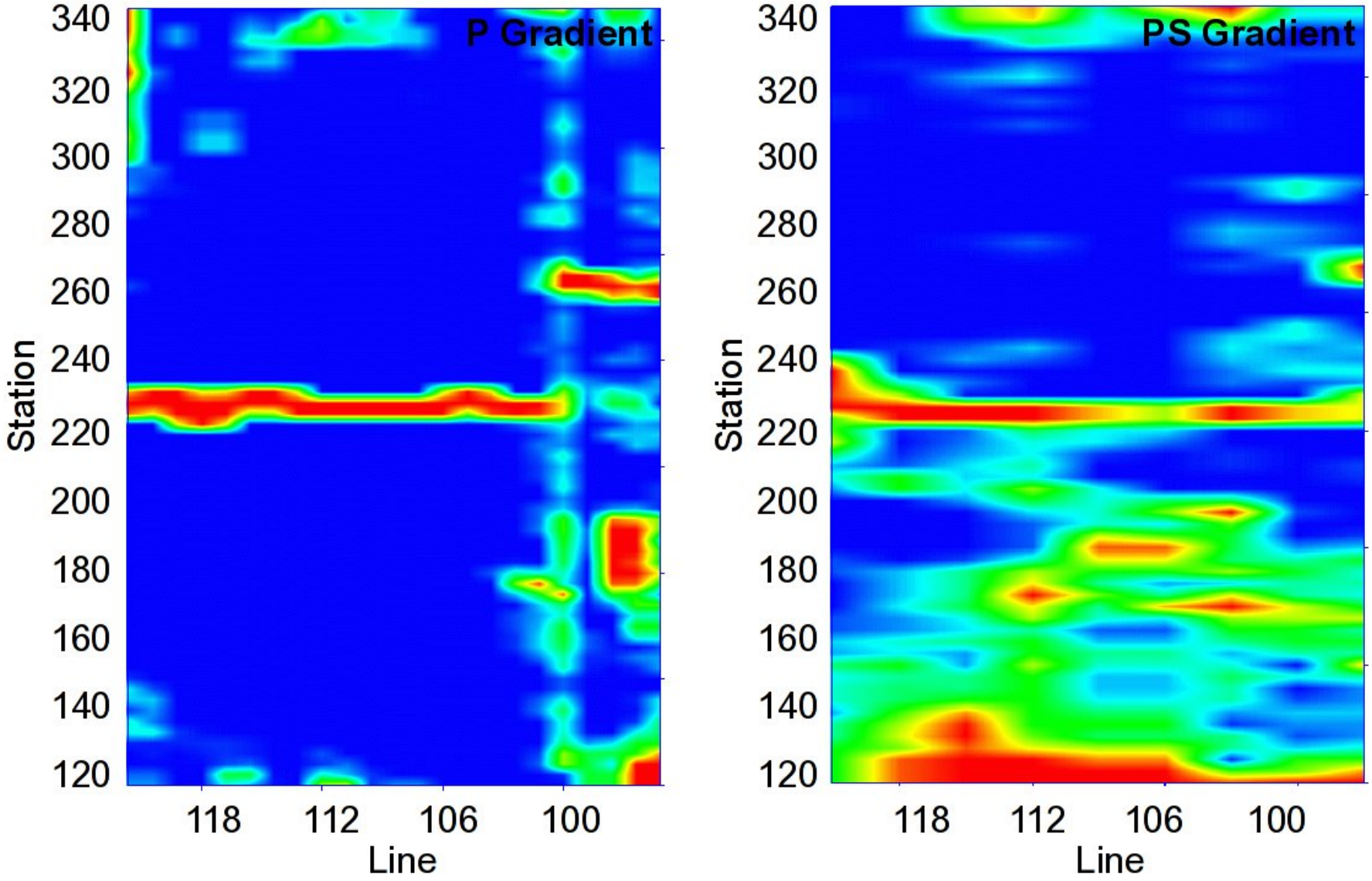

Figure 6.6: Normalised gradient images for the P and PS datasets. High gradient is indicated by red. This attribute strongly identifies the faulting near Stations 225 and 260.

6.2 PS Attribute Analysis

Attribute analysis is a key tool for seismic interpretation, particularly for 3D seismic surveys. Attribute analysis involves isolating properties of the seismic waveform and displaying these to highlight irregularities. These irregularities may correspond to faulting, bed thickness variations, changes in geology, among other things. They may also be caused by noise and other non-geological properties of the seismic image. To determine which anomalies are of geological significance, the analysis is usually conducted for a number of attributes. An event occurring on a single attribute has low probability whereas one occurring on many attributes has higher probability of being real.

For the PS attribute analysis we have examined four attributes. These are the dominant frequency, phase and amplitude of the event, and the maximum gradient of the horizon (introduced in the previous section). The frequency, phase and amplitude attributes have be calculated by finding the instantaneous value of each attribute for each sample in the volume, and then averaging over a 30ms window centred about the target horizon. Figure 6.7 shows the map view image for each of the attributes.

The frequency attribute is plotted with red representing low frequencies (<30Hz) and blue higher frequencies (>55Hz). The image shows quite a change across the main fault with the northern section being dominated by lower frequencies and the southern section by higher frequencies. This is probably due to a greater percentage of high frequency noise contributing to the southern section.

The phase image is quite difficult to interpret and has been used more as a tool to confirm other attributes. There are two faint events. The main is a phase change across the large fault. There is also a region in the southern half of the survey that has a linear nature indicated by the dashed ellipse. If the phase image was to be considered alone then these events would probably have been lost in the noise.

For this survey the gradient and amplitude attributes show the strongest response to the faulting. In Figure 6.7 the amplitude plot has been coloured such that low amplitudes are red and high are blue. The gradient plot has been coloured with high gradient contrasts in red. The purpose of this is to highlight the low amplitude and high gradient properties of the faulting. The main fault at the centre of the survey is well defined for both attributes with a slightly sharper image for the gradient

plot. The northern fault is also present on both although it does have greater extent on the amplitude plot.

There is also a linear region that starts close to the main fault on the western lines and trends toward the south for the eastern lines. This event is almost continuous on the amplitude plot. On the gradient plot it consists of a number of bright spots. In general the amplitude image has lower amplitudes in the southern region. This is probably a result of higher attenuation associated with the black-soil weathering layer.

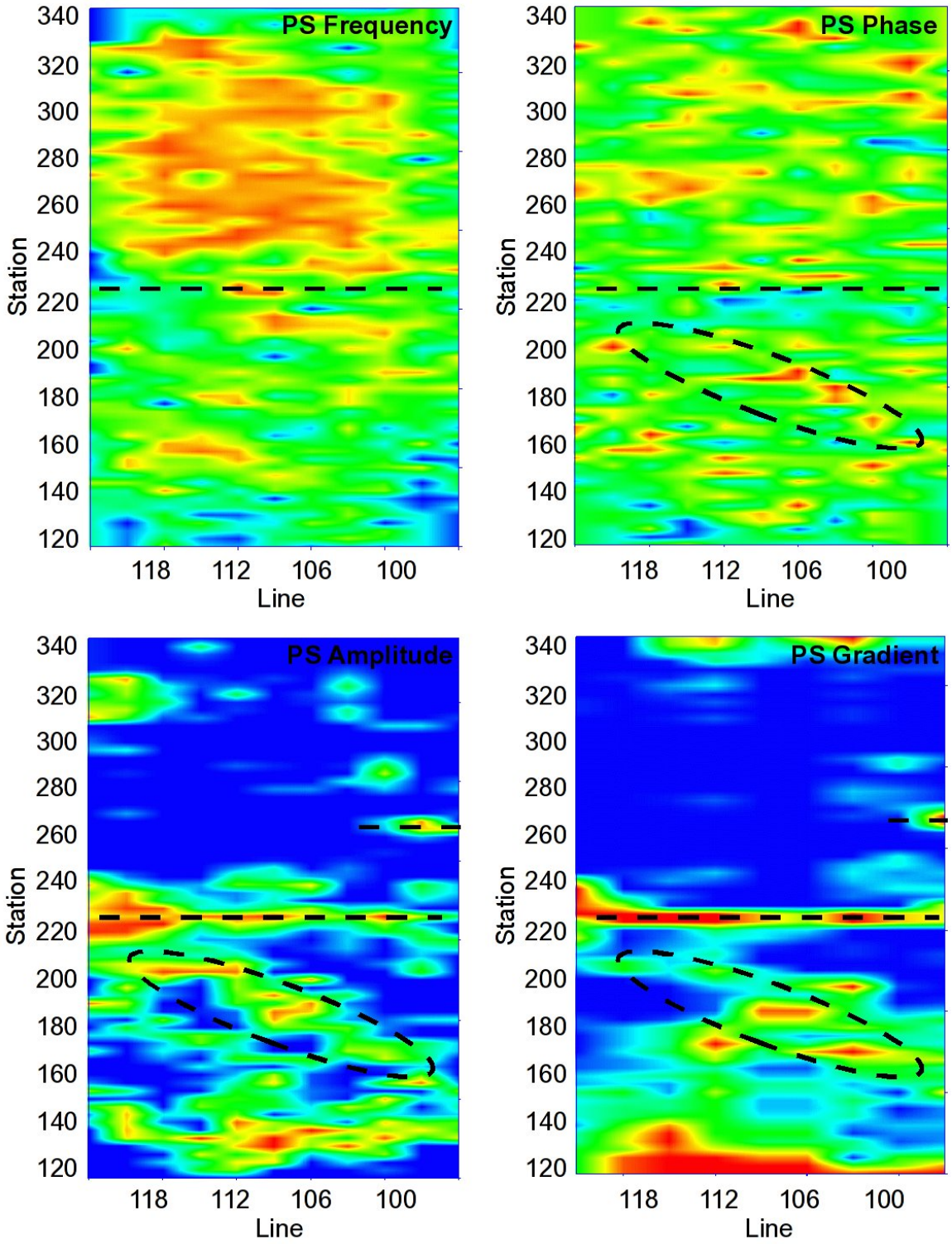

Figure 6.7: PS attribute analysis. Includes seam frequency (red low dominant frequency), seam phase, seam amplitude (red low amplitude) and horizon gradient (red high gradient). The dashed black lines show the possible faulting and the ellipse shows an anomalous attribute zone that may be caused by faulting or some other physical property.

6.3 Integrated Interpretation

In the preceding sections of the chapter we have demonstrated a number of different methods of interpreting the P and PS datasets. For these to be useful it is important to integrate all the different pieces of information into a single interpretation.

Figure 6.8 shows a map view which summarises the preliminary integrated interpretation. This shows the key features that have been identified. These are colour coded according to which data set they have been derived from. Structures found only on the P dataset are plotted in cyan, structures only on the PS dataset are plotted in green and those found on both in red. The location of the faulting has been determined from unmigrated data. Therefore there may be some variation in true lateral position of these. For structures that have been interpreted on both the P and PS data sets, the plotted position of the structure has been determined by averaging the two.

The main fault and the northern one have been identified on both datasets giving high probability that these structures exist. In the south region there is a fault that has only been identified on the PS data and another that has only been found on the P data. These faults tie well with the northern edge of a PS attribute anomaly (dashed ellipse). These faults have a similar bearing and give the impression that they could be part of the same fault line. However, the throw of these faults in in the opposite direction. This implies that either the faults are not the same or they are the same and the faulting has been misinterpreted on one of the data sets. Due to small size of the fault on the P-wave data and the low signal-to-noise ratio of the PS data it is difficult to determine which is more correct.

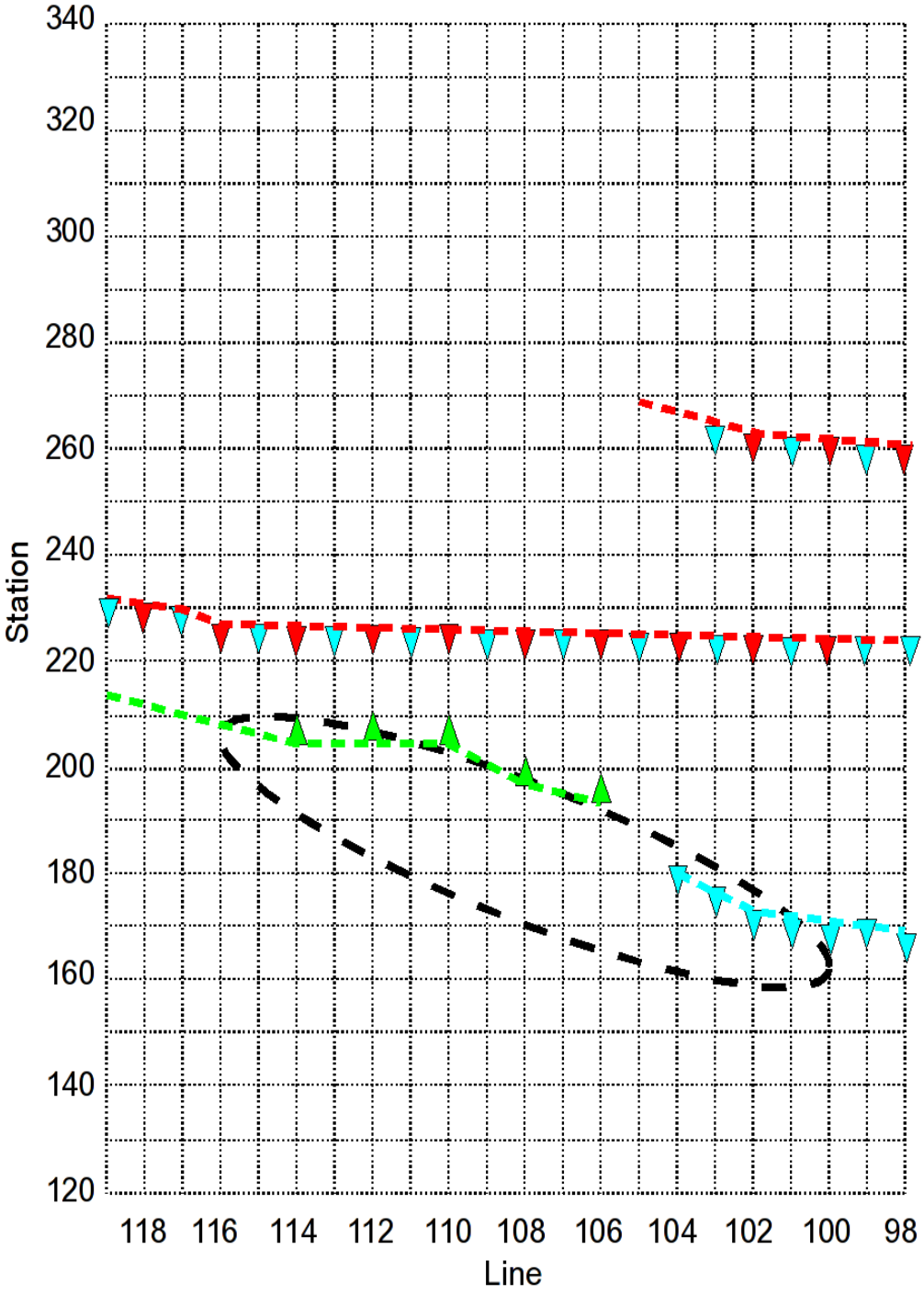

Figure 6.8: Integrated structural interpretation combining the P and PS section interpretation with the attribute analysis. The cyan events are only found on P data (using either horizons, attributes or both) and the green only on PS data. The red events have been confirmed by both datasets. The black ellipse is the anomalous zone from the PS attributes. The northern edge of this matches well with faulting interpreted on the P and PS datasets. The alternating colours along the main fault result from the PS bin spacing being twice that of the P bin spacing.

7 Preliminary Analysis of Azimuthal Anisotropy

7.1 Introduction

As illustrated in Section 1.2.7, previous 2D PS work conducted by Velseis has demonstrated that positive and negative offset data can yield different velocities and structural interpretations. This is an example of apparent azimuthal variation of the geological environment and may be caused by diodic illumination (introduced in Chapter 1), shear-wave splitting or real azimuthal velocity variations that are inherent in the geological layers.

The orientation and amount of azimuthal velocity variation is often related to the localised stress field (Figure 7.1). At the deep petroleum-scale, variation in shear-wave velocity with azimuth is generally on the order of 1-5%. For the shallower coal-scale environment surface-related stresses tend to lead to extensive fracturing, which can produce azimuthal velocity variations in excess of 10% (Crampin, 1997).

While Chapter 6 has demonstrated that a reasonably good interpretation can be achieved by ignoring azimuthal anisotropy it is expected that the results might be improved if this effect could be allowed for. In this chapter we have made a preliminary examination of shear-wave splitting and azimuthal velocity variations to determine if azimuthal anisotropy exists, and to what extent it will affect the stacked volume.

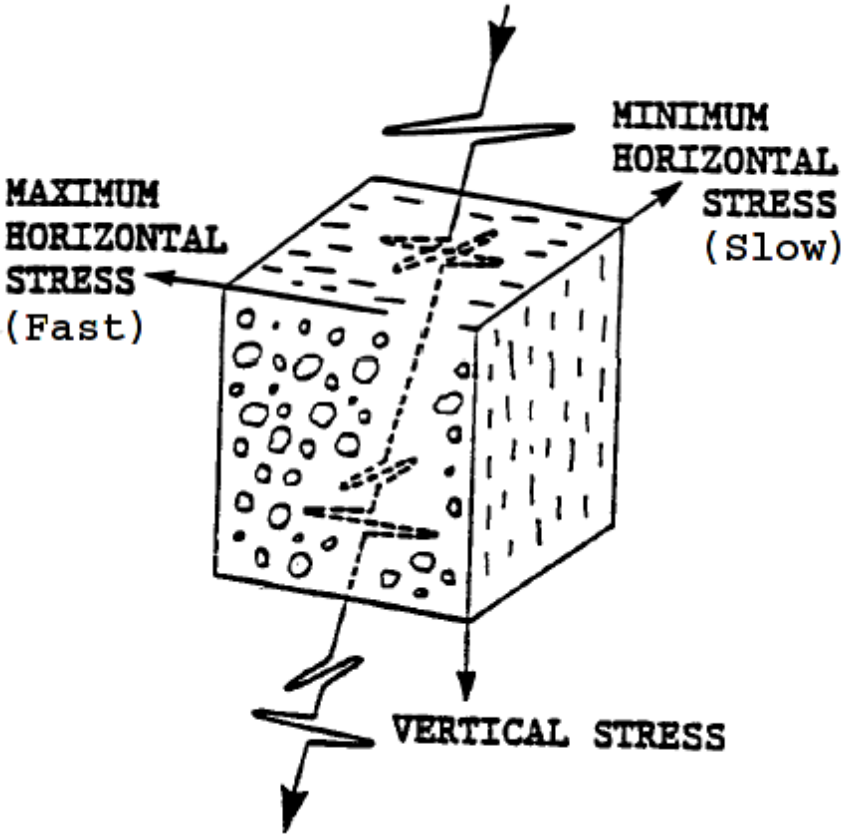

Figure 7.1: This figure comes from the classic paper of Crampin (1997). It demonstrates how an S wave splits into slower and faster components when passing through a fractured medium. It also indicates how the fracturing relates to the local stress field.

7.2 Shear-Wave Splitting Analysis

In the presence of a localised stress field fractures can form in a rock unit. These fractures are generally orientated in the direction of maximum horizontal stress. When a shear wave travels vertically through a fractured medium the shear wave tends to split into a fast wave and a slow wave (Figure 7.1). These waves vibrate in the direction of, and perpendicular to, the direction of fracturing, respectively. Fracturing may be associated with faulting. This was one of the reasons for choosing a trial location with a significant fault. Generally, the S wave must travel a distance of several wavelengths for the splitting to be detectable.

Shear-wave splitting can be observed by comparing the horizontal components. Normally PS reflection energy occurs on the radial horizontal component. If shear-wave splitting has occurred then some of the reflection energy will be rotated onto the transverse component. Figure 7.2 shows the radial and transverse stacked sections for Line 112. This demonstrates that no significant shear-

wave splitting has been detected on this line and is representative of the entire survey. This result is not unexpected. The total path length travelled by the S wave is only of the order of two wavelengths. It is likely that this is insufficient distance for S-wave splitting to be well developed.

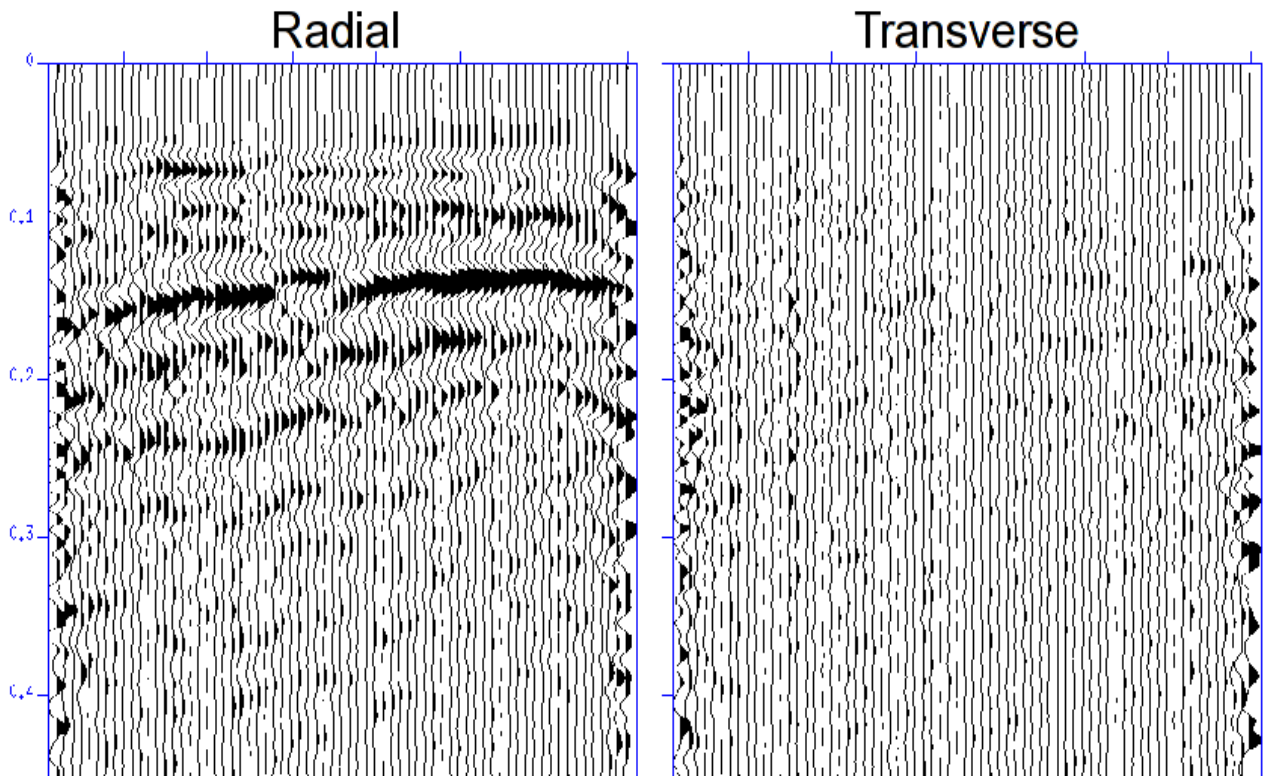

Figure 7.2: Stacked sections from the radial and transverse datasets for Receiver Line 112. Vertical axis is time in seconds. The northerly end of the receiver line is toward the right. This line is representative of the whole volume. The lack of energy on the transverse image suggests that shear-wave splitting is not significant.

7.3 Azimuthal Velocity Analysis

Geological layers are generally not homogeneous and may be formed with an asymmetric nature (e.g. laminar bedding) or may be fractured due to local stress fields. In these environments the velocity of a seismic wave through a layer may be dependent on the wave type and the direction of travel. Another process, unique to converted waves, that also produces an azimuthal velocity effect is diodic illumination. This is caused by inhomogeneities of limited lateral extent occurring above the target reflector. For rays from different directions one ray path may pass through the body as a P wave and the other may pass through it as an S wave. This can result in differing travel times and therefore different moveout velocities (Figure 7.3).

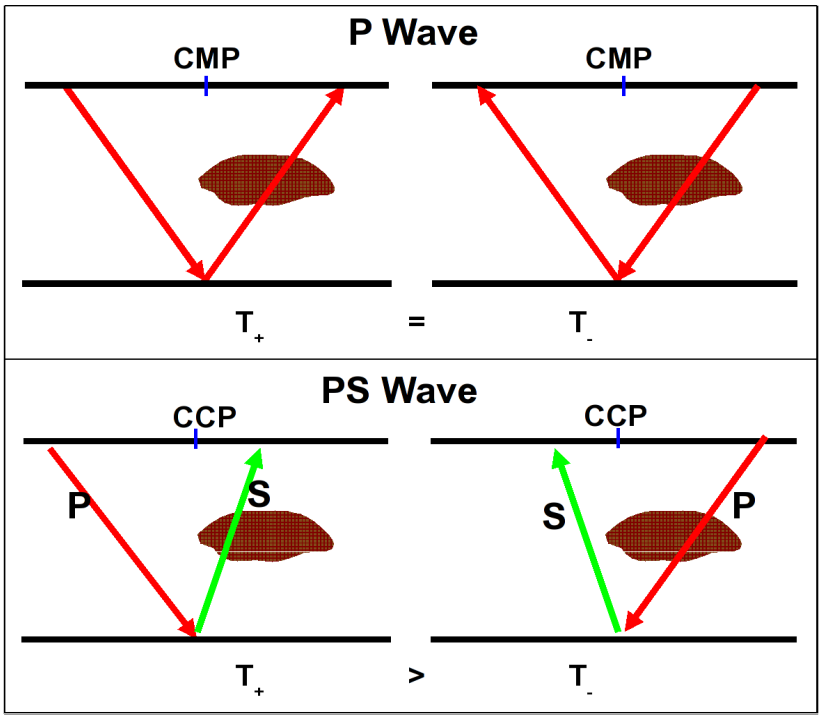

Figure 7.3: 2D example of diodic illumination. If a positive offset P-wave passes through a body of anomalously low seismic velocities it will have the same travel time as the equivalent negative offset ray. For a PS ray an S -wave passes through the anomaly for the positive offset and a P wave for the negative offset. The time delay introduced by the anomalous body would typically be larger for the S wave. Therefore the positive offset ray will have a later arrival time which will result in smearing if the rays are stacked together.

If the subsurface is azimuthally invariant and all static errors have been corrected then we would expect the moveout velocity for all traces contributing to a CCP bin to be the same. Therefore, azimuth-limited stacks should have similar structures to the all-azimuth stack. Figure 7.4 shows the horizon picks of Line 112 for the cases of the all-azimuth stack and 18 azimuth-limited stacks. This demonstrates that there is a significant (on the order of 30ms) variation in the structure with ray azimuth.

To determine if these azimuth effects exhibit orderly behaviour, we have plotted the relative difference in structure at each CCP versus the azimuth (Figure 7.5). There appear to be some strong effects in the vicinity of the large fault. This could be due to fault related diodic effects, or fracture related azimuthal behaviour. However, the errors in picking due to unmigrated diffractions are expected to be significant in this zone causing the degree of true azimuthal anisotropy to be difficult to determine. Away from the fault the image has less structural variation although it is still on the order of +/- 10ms. For a 25Hz wavelet this would correspond to shifts of +/- quarter of a wavelength. This would lead to significant smearing of the target horizon and a consequent reduction in the resolution of the stacked PS volume.

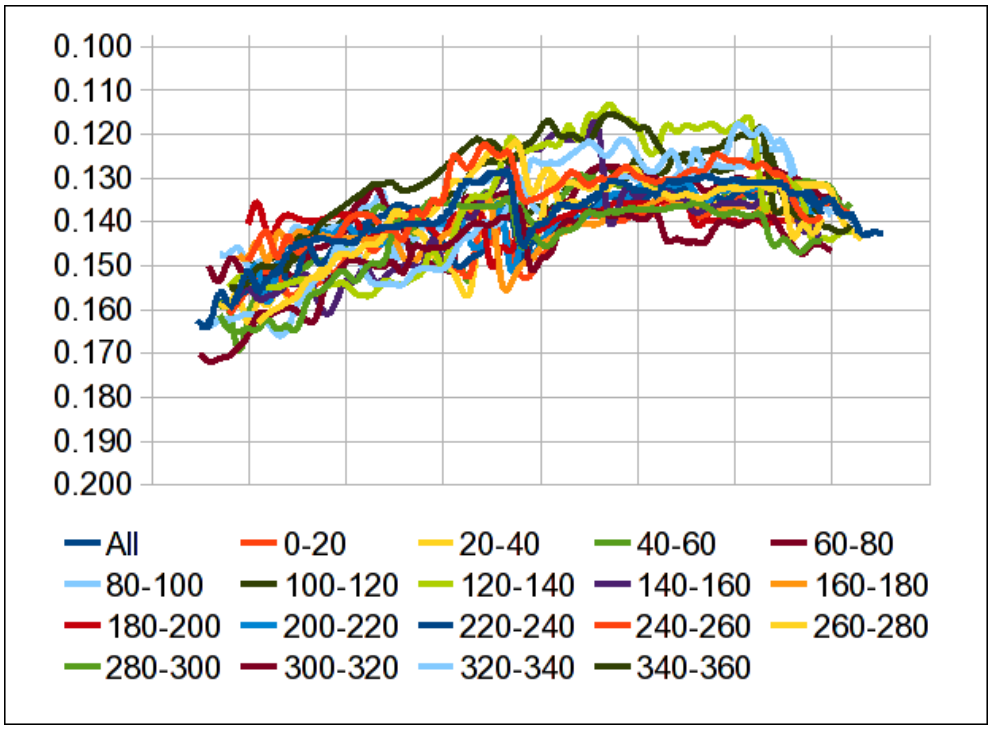

Figure 7.4: Azimuthally limited horizon picks from Line 112 of the PS volume. Vertical axis is the structure time in seconds. The northern end of the receiver line is toward the right. The structure varies with azimuth by up to 30ms.

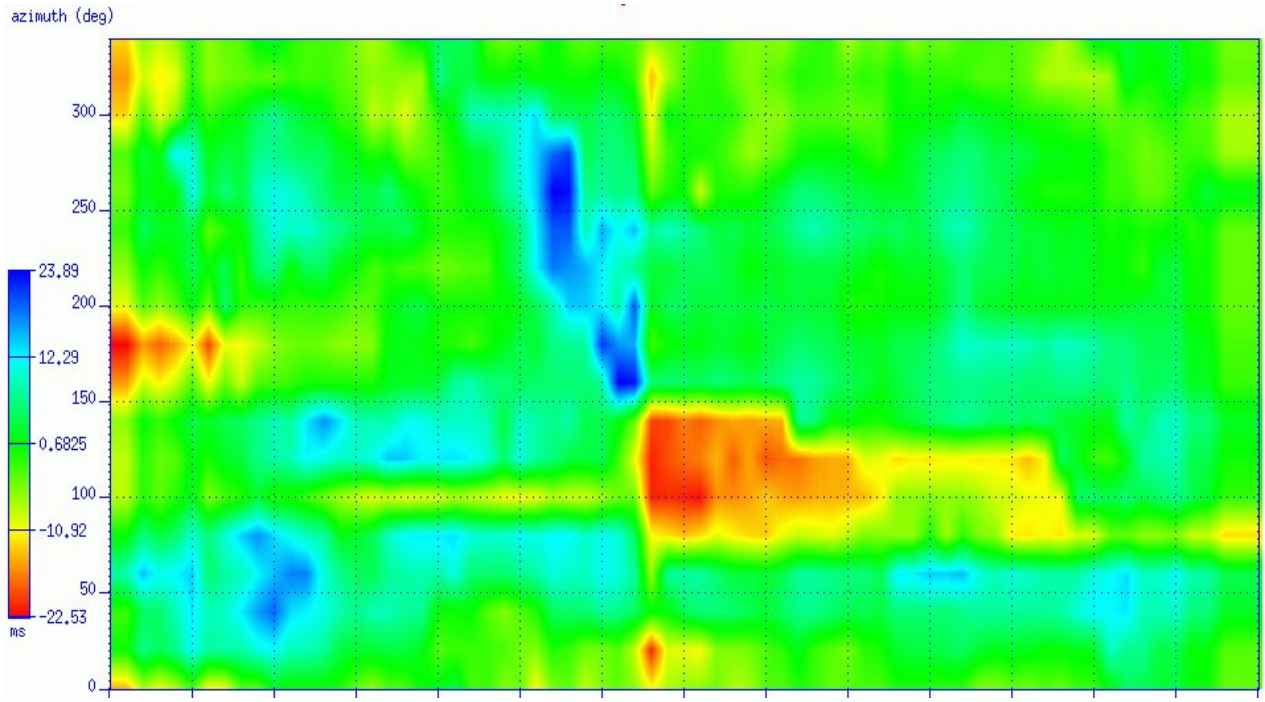

Figure 7.5: Relative difference in horizon time (colour coded), as a function of position along Line 112 (horizontal axis) and ray azimuth (vertical axis). The largest anomalies appear close to the main fault and could be the result of diffraction effects. Ignoring these, the azimuthal variation may be on the order of +/- 10ms.

To ascertain whether this azimuthal analysis on Line 112 is representative of the entire survey, another method has been employed to investigate azimuthal velocity variations. The concept is similar to automatic velocity picking using semblance. For each CCP bin the gathers are sorted into subsets based on azimuth ranges. For each subset a range of PS NMO parameters are trialled to determine which gives the best stack, for a window of data about the target horizon. For this trial a constant P-wave velocity of 3200m/s has been used and γ has been varied between 1.5 and 3.0. Since this is an automated process it tends to generate some anomalous results. These are generally associated with noise and complexities in the shape of the seismic wavelet generated at the target. To improve the probability of a meaningful solution a number of CCP values are averaged. The anomalies often cause the technique to return the maximum or minimum γ values. For the following tests these are considered to be outliers and are removed prior to the averaging process.

Figure 7.6 shows a radial plot of the optimum γ value versus azimuth where all CCP points in the survey have been included. Both the median and mean average values are displayed. For the most part these tend to agree, with low gammas at the 100 and 280 degree azimuths and higher gammas at the 180, 240 and 340 (300 for median) degree azimuths.

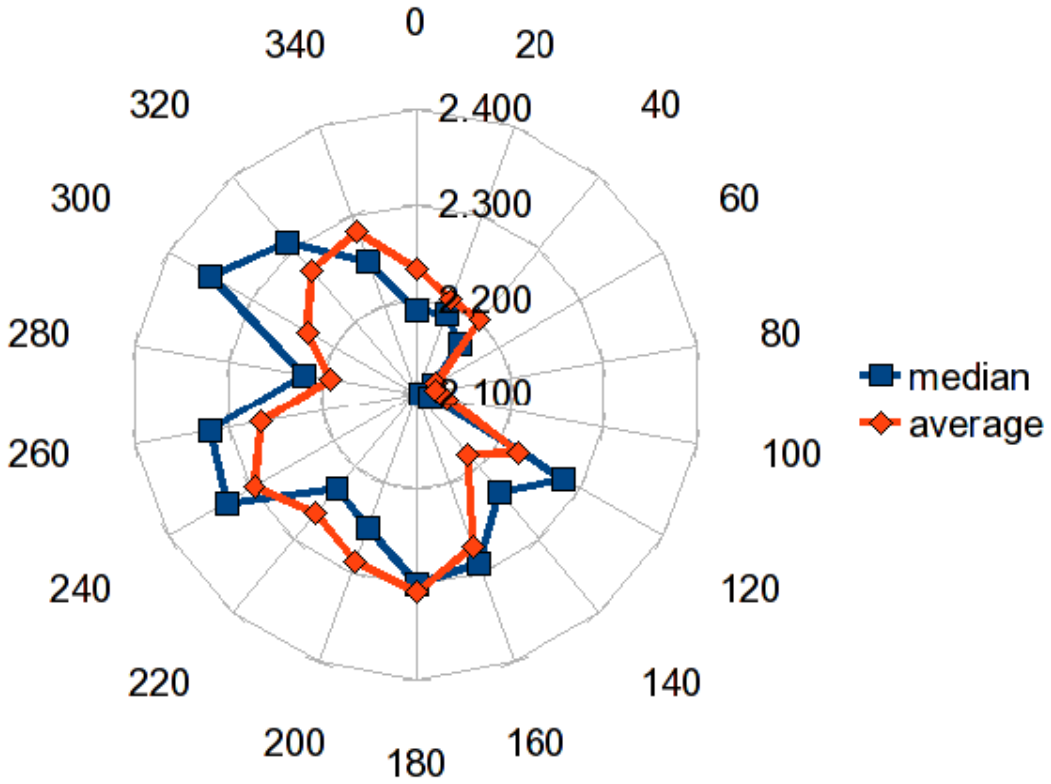

Figure 7.6: Radial plot of the preferred γ value versus the azimuth for the entire survey. This is likely to be a function a number of different properties, not all of them geological.

As noted above (Figure 7.1), there is evidence that seismic velocities may be affected by distribution of stresses in the earth. Based on this concept, we might expect our γ plots to exhibit a dipolar distribution with γ, with large γ values at an azimuth and its polar opposite, and smaller γ values at azimuths that are offset by 90 degrees. There is some evidence of 'elongation' in Figure 7.6. However, the overall variation in γ is quite small (2.1-2.35). This variation is around 1% and seems relatively moderate for a shallow environment. This may suggest that there is minimal azimuthal velocity anisotropy. Alternatively, any azimuthal effects may be more localised, and are being smoothed in the global averaging process.

To explore this second option, we have performed the averaging process over a smaller number of CCP locations. For this test 60x60m bins have been used. Each bin combines 3 CCP locations in the cross-line direction by 5 locations inline, giving a total of 15 CCPs to average. The bins have been selected such that they are less likely to have CCPs with anomalies caused by low fold and edge effects Figure 7.7 displays the centre point of each CCP group, and also includes the interpreted fault locations.

The radial plots corresponding to these individual bins are given in Figure 7.8. The γ values on

these have a greater range then seen in Figure 7.6., covering the full extent of the tested velocities (1.5-3.0) although averaging about 2.25. This suggests that the full-survey analysis shown in Figure 7.6 was indeed suffering from spatial smoothing. The mean and median values show very good correlation (better than for the all-CCP case). This is probably due to more of the contributing CCPs for each group representing similar azimuthal velocities. There are some similarities between some of these figures. For example figures from the second bottom row have a similar shape. The expected dipole direction is difficult to quantify by direct examination, although a number of the figures show some general NW-SE elongation. One way to a more objective interpretation is to fit an ellipse to each of the plots.

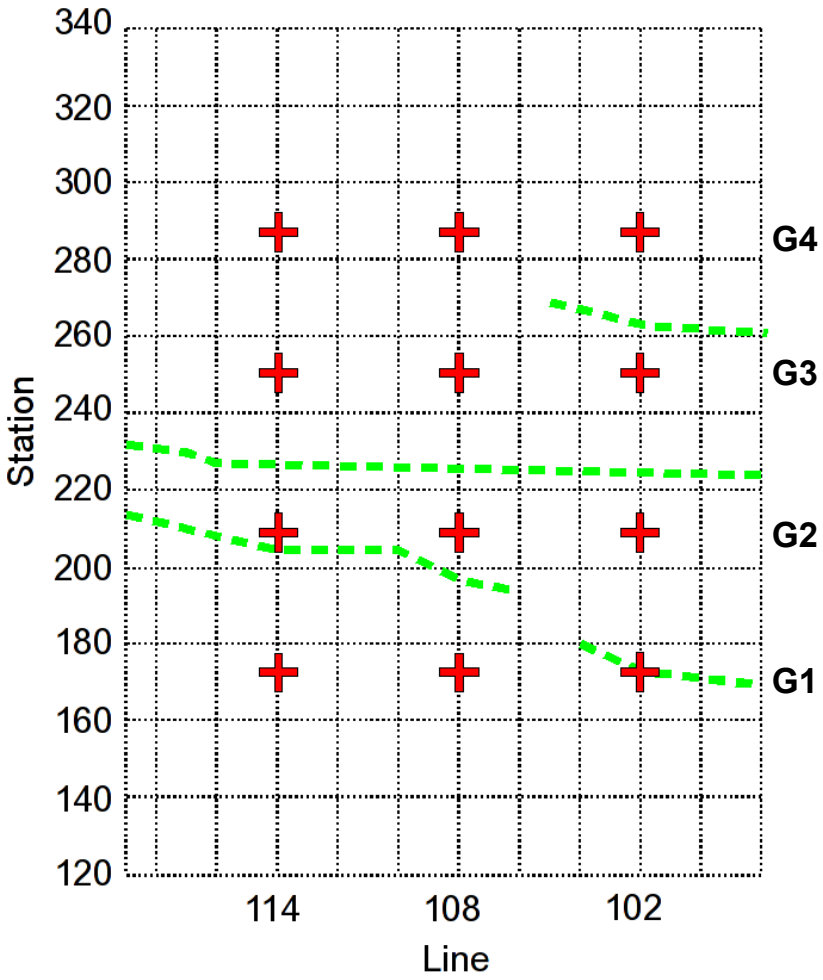

Figure 7.7: Location of the centre points of the CCP groups (red crosses). The possible faulting has been overlain for reference. The annotations on the right allow reference to individual groups in the subsequent figures. For example, L102-G1 refers to the group at the bottom right.

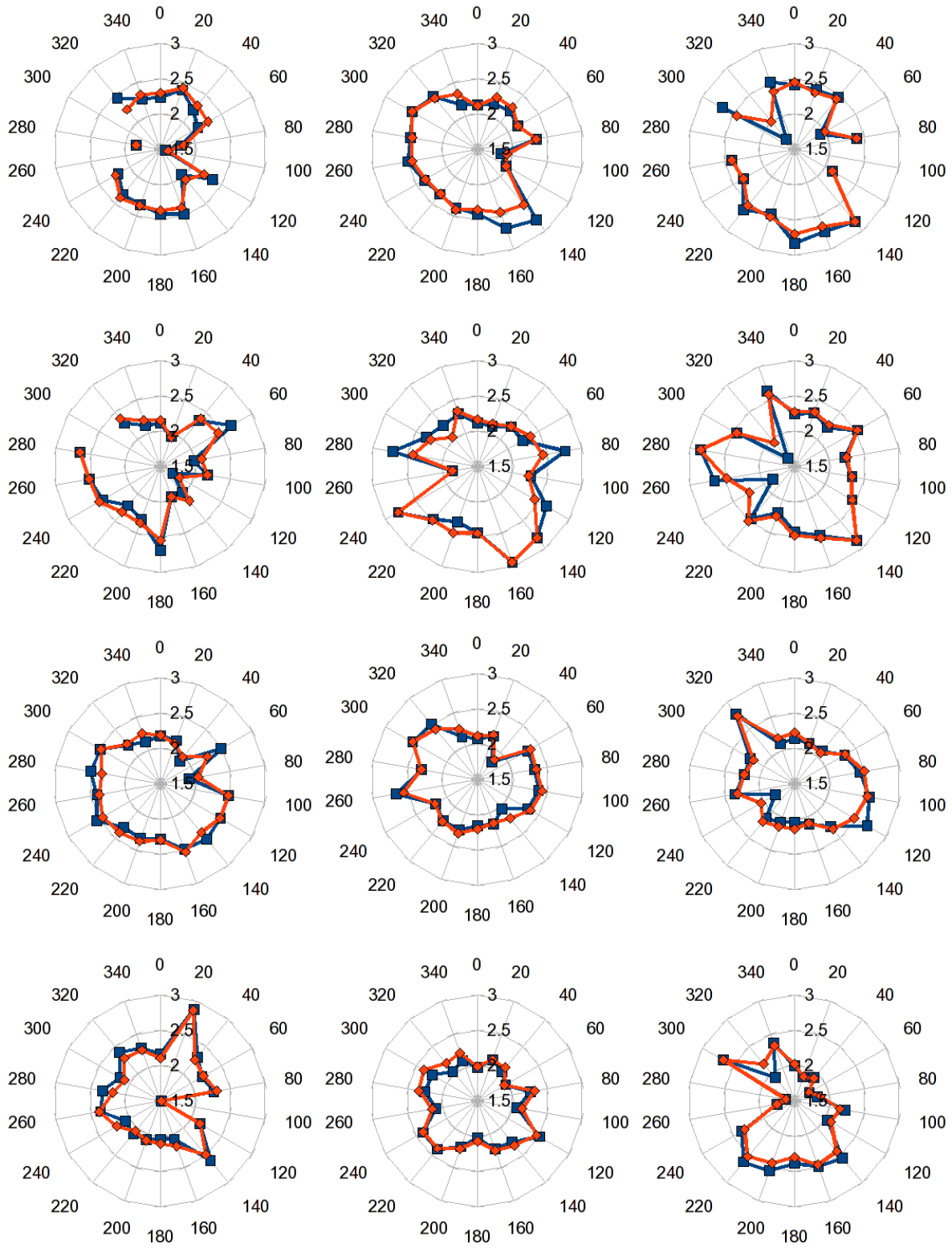

Figure 7.8: Optimum γ (radial axis) versus azimuth corresponding to each of the CCP groups on Figure 7.7. Both the mean (red) and median (blue) values are displayed. Variations in γ are more significant than for the full survey average in Figure 7.6. A number of the locations exhibit general azimuthal trends, although the analysis appears to be contaminated by spurious points.

Figure 7.9 illustrates the concept where one of the analyses from Figure 7.8 (L102-G2; Row 3, Column 3) has been fitted with an ellipse. The nonlinear least-squares algorithm (Gander, et. al., 1994) returns the equation of the ellipse in terms of the ellipse centre, the semi-major axis, the semi-minor axis, and the direction of the semi-major axis. The ratio of the length of the semi-minor and major axes gives an indication of the amount of azimuthal anisotropy (1 = no anisotropy; close to 0 = large anisotropic effect). The flatness of an ellipse is equal to one minus this ratio, and in this case is indicative of the degree of anisotropy. The direction of the semi-major axis is equivalent to the azimuth exhibiting greatest γ.

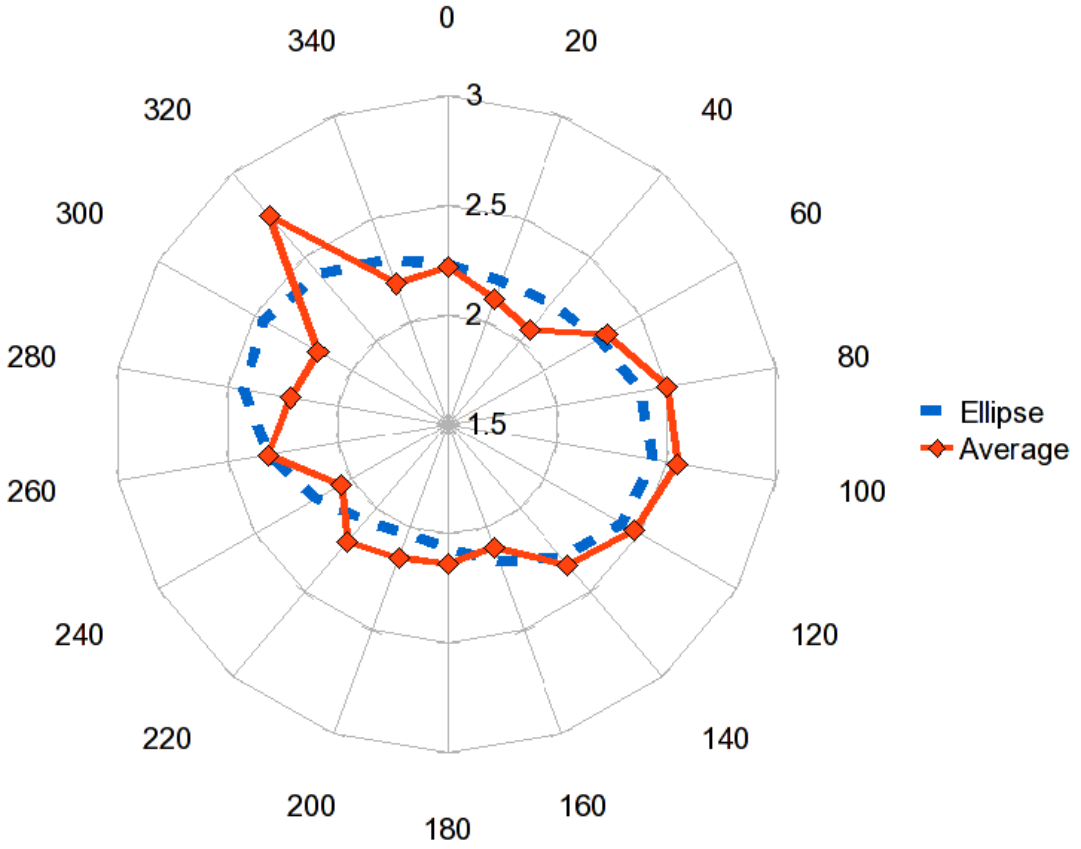

Figure 7.9: Localised stress fields might be expected to produce dipolar azimuthal variations. Fitting an ellipse to γ/azimuth data can give an indication of the most likely direction of any such stress field. This figure shows a representative γ/azimuth image (taken from Figure 7.8) and its corresponding best fit ellipse.

Figure 7.10 summarises the direction and flatness response for each of the CCP groups. Initial investigation of this image alone implies that the angle of the maximum γ value is distributed over many azimuths for the survey. If we also take into account the position of the CCP groups we see that they divide into two main sets. Those more toward the top and bottom of the survey have loose north/south distribution with the maximum gammas occurring in the ranges -20 to 25 and 160 to

205 degrees. The other set consists of CCP groups having a tighter WNW/ESE distribution occurring in the ranges 120 to 135 and 300 to 315 degrees. Figure 7.11 shows that these groups tend to be located in the vicinity of the central faulting. Note also, that the interpreted ellipse major axes tend to be orientated close to the strike of the faulting in this region (Figure 7.11).

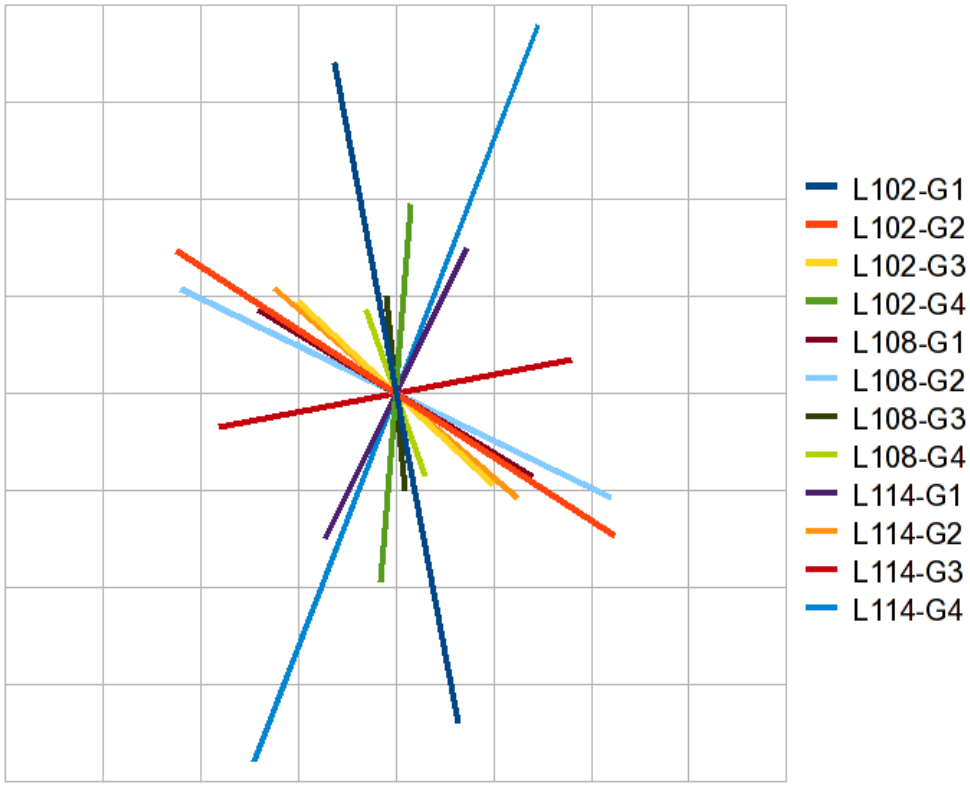

Figure 7.10: Spider plot of the ellipse parameters for each CCP group marked on Figure 7.7. The direction of each line represents the direction of semimajor axis and corresponds to high γ values and therefore lower S-wave velocity. The length of each line indicates the flatness of the ellipse and is proportional to the degree of anisotropy. The lines with directions ranging from 120 to 135 and 300 to 315 degrees are close to the main fault lines and may be indicating zones of fracturing.

High γ (Vp/Vs) values in the strike direction correspond to lower S-wave velocities (Vs) in the strike direction and higher velocities perpendicular to the strike of the faulting. The fact that faulting in this region is reverse does suggest horizontal compressive stress perpendicular to the strike. These observations are consistent with the theoretical velocity stress model introduced in Figure 7.1. That is, the observed azimuthal anisotropy in S-wave velocity near the fault zone is consistent with the expected stress orientation. This suggests that azimuthal analysis of the type described here might provide a tool for prediction of stress and fracture orientation.

We noted above that the degree of anisotropy indicated by the globally averaged analysis was

relatively modest, about 1%. It is of interest to examine the degree of anisotropy suggested by individual localised analyses summarised by Figure 7.10.

The flatness values for all the CCP groups range from 0.05 to 0.2 although those above about 0.13 (L102-G1 and L114-G4) may be irregularities. This suggest that the difference between γ values is generally 5-13%. This matches well with the expected shallow-environment variation given by Crampin (1997). Again, this confirms that our globally averaged analysis suffered from smearing. It also suggests that the size of the analysis zone defined in Figure 7.7 (approx 90m x 90 m) may be more suitable in terms of extracting meaningful azimuthal parameters.

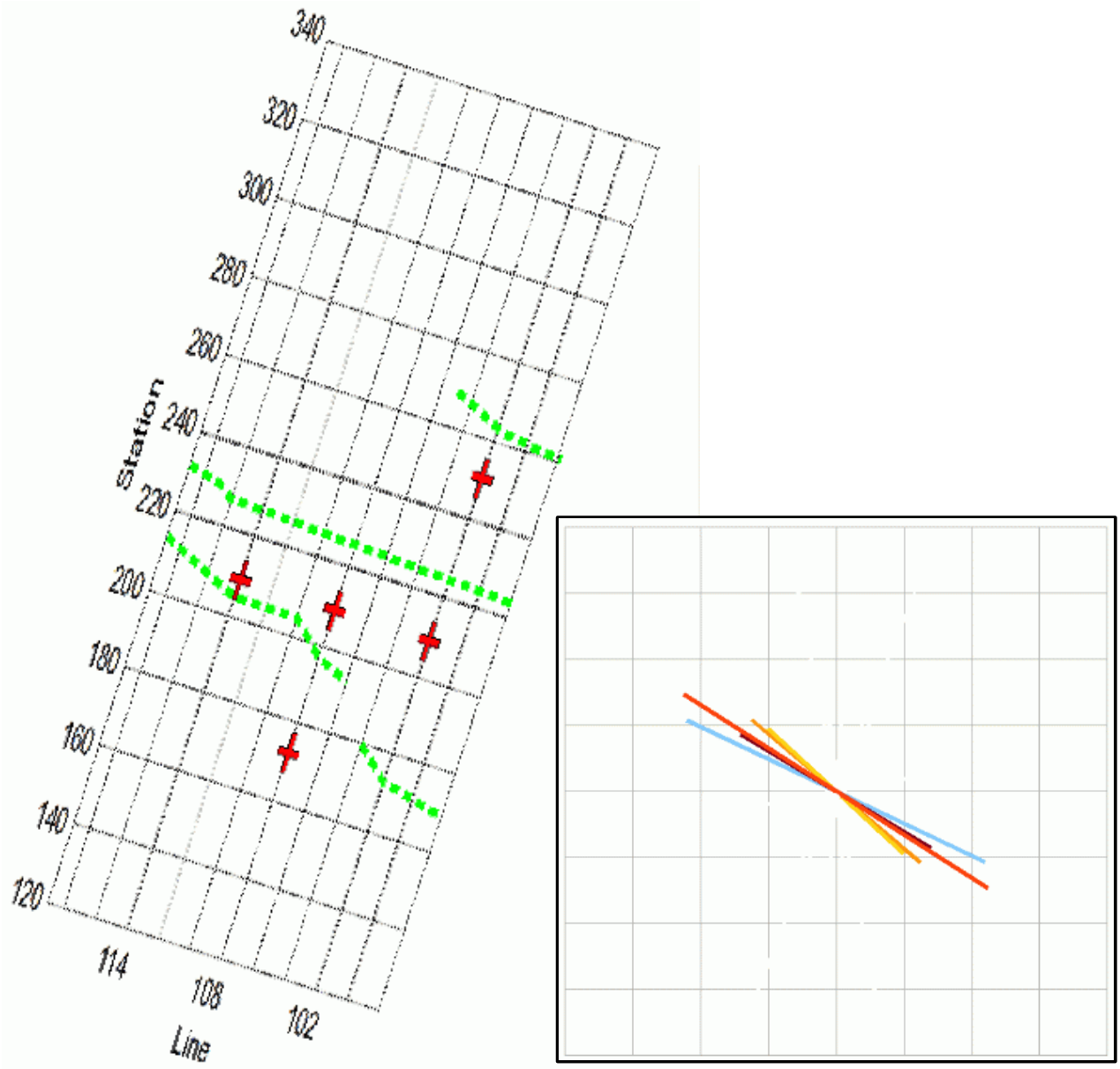

Figure 7.11: Close to the region of faulting the semi-major axes of velocity ellipses tends to align with the strike direction of the faulting. The image on the left gives the ground location of velocity analysis bins, and the image on the right gives the spider plot of the corresponding ellipse response.

7.4 Conclusions

This investigation has demonstrated that for the PS data, both structural horizon-picks and azimuthal velocities appear to have significant variations with azimuth. Based on P-wave analysis, Chapter 5 (Figure 5.1) demonstrated that such azimuthal variations may not be due to true geological properties and can result from errors in the processing flow such as uncorrected static errors. We have also shown that calculating the S receiver statics in-particular is difficult and can

be subject to errors. Nevertheless, the implication that some azimuthal effects appear to be aligned with structures suggests that at least some of the azimuthal effects may be real. In particular our analysis suggests that azimuthal analysis of PS moveout velocities may provide indicators of directions of horizontal stress and associated fracturing. This is a significant result which warrants further investigation.

8 Conclusions and Recommendations

8.1 Motivation for This Research

Seismic reflection has become an important tool for the coal industry and is used for both exploration and mine planning. For conventional P-wave surveys there has been a move from 2D recording geometries to 3D. 3D seismic surveys provide improved resolution, and better cross-line mapping of structures.

Recent ACARP projects (C10020 and C13029), and subsequent commercial surveys, have demonstrated that simultaneously acquiring converted-wave (PS) data can add significantly to geological interpretation, by identifying new fault structures, improving the determination of fault geometries, and providing superior imaging of top-of-coal for shallow targets. These projects have to date been restricted to 2D-PS recordings.

In this project our 2D methodologies and techniques have been extended to examine the feasibility of acquiring coal-scale 3D-PS imagery. This concept has been tested by acquiring, processing, and interpreting a multi-component 3D trial from a location in the Bowen Basin. The acquisition geometry of this trial dataset has been specifically designed to allow an examination of directional imaging complexities, which have been identified in both previous 2D ACARP projects.

The significant conclusions drawn from this research, together with suggestions for future research and development into multi-component coal seismic, are presented in the following sections.

8.2 Summary of Conclusions

8.2.1 Survey Design

It has been found that PS data processed with P-wave binning parameters have unsatisfactory azimuth/offset distributions. The natural bin size for PS data is closely related to the receiver spacing, which suggests that integrated P and PS acquisition programs should be designed with closer receiver spacing than standalone P-wave surveys.

Modelling of the reflection behaviour with offset has shown that phase variations with offset may be more problematic for PS data and could lead to a reduction in usable offsets and a further

reduction in the fold of PS data.

In general this has demonstrated that ray-path properties are more complicated for PS waves than for conventional P waves. Therefore, it is important to include a rigorous quantitative survey-design stage in any 3D-PS seismic acquisition program.

8.2.2 Acquisition

The 3C dataset was acquired using standard Sercel 428 equipment with the traditional vertical geophones replaced by 3C geophones. A Vibroseis source was used. This allowed a very high fold survey to be acquired economically.

Both the P and PS data quality was quite good, although some degradation of the PS data was observed in the southern region, where a black-soil weathering layer occurs.

This project has demonstrated that it is feasible to acquire good quality 3D-PS datasets with relatively minor adjustments to standard equipment and field procedures

8.2.3 Processing

The 2D processing sequence developed during ACARP projects C10020 and C13029, has provided a good basis for processing the 3D-PS dataset. Many of the standard 2D converted-wave processing algorithms have been successfully applied to the 3D dataset without any changes. Others have required small modifications. For example, the PS-NMO algorithm remains essentially the same. The only variation is that the interpolation needed to be changed for 3D.

Processes unique to 3D-PS datasets that have been developed for this project include horizontal coordinate rotation into the radial/transverse directions, and 3D horizon based binning. While the binning algorithm is based on the concept of 2D horizon binning, it has been rewritten to accommodate a 3D coordinate system.

As part of this research a detailed S-wave receiver statics investigation was conducted. It was found that the PS residual-statics method that had been used for the previous 2D PS surveys may produce incorrect solutions in some statics environments. This is caused by errors in the horizon picking stage which in turn leads to parameter leakage between the receiver and structural parameters. Two alternative statics methods have been examined in this project.

The robust statistics approach uses the horizon picks from the residual statics method and uses averaging methods to determine the short-wavelength component of the S-wave receiver statics. This produces reasonable event continuity, but the lack of long-wavelength correction can produce errors in structural interpretation.

The second alternative is a time-term method, based on refraction statics. This method produced the best statics solution for this dataset but it requires good PPS refraction events and high fold. These may not be possible for all datasets.

This project has demonstrated that a 3D-PS processing flow can successfully generate a stacked 3D volume that can be interpreted for faults and other structural morphology.

8.2.4 Interpretation

The stacked P and PS volumes have reasonable data quality, with the P-wave data having slightly better resolution. Inline sections from the P and PS datasets have been interpreted. These generally depict a single seam dipping toward the southern end of the survey. The faulting is dominated by reverse faults with strike almost perpendicular to the inline direction. Generally the upthrown side is to the south.

Attribute analysis was applied to the PS data. Mean phase, frequency, amplitude, and maximum-gradient properties were examined. The amplitude and gradient images showed the strongest response, indicating the main fault, a secondary one to the north and a zone of amplitude anomaly to the south. The gradient attribute was also examined for the P-wave data. This also indicated the faulting.

The interpreted results from the P and PS sections and the attribute analysis have been integrated into a single fault map. The large fault and the northern fault are confirmed by all of these. The P and PS images tend to highlight different features in the south. However both sets tend to tie with the PS attribute anomaly.

Both the P and PS datasets have identified extra structures to the earlier 2D P-wave dataset. This demonstrates the need for 3D seismic when a more detailed interpretation is sought. The PS volume has been shown to be a useful tool for confirming the P-wave data, and can also give an indication of additional faulting.

This investigation has also included an analysis of the dependence on ray-azimuth. It has been

shown that both interpreted structures and moveout velocities appear to vary based on the azimuth of the seismic rays. In the vicinity of the faults, the velocity analysis appears to suggest a faster S-wave velocity perpendicular to the faulting. This could be an indication of local fracturing. These results are very interesting. It is worth noting, however, that a brief analysis of P-wave data has shown that error in processing may also result in pseudo-azimuthal effects. Clearly further research is needed on the question of azimuthal anisotropy.

8.3 Future Research and Development

8.3.1 Acquisition

The method used to acquire the data was quite effective. However a static grid was used for this survey. For larger surveys it would be necessary to use a rolling grid. The use of standard equipment resulted in 3 recording units at each station. To ensure these were connected correctly a multiple pass QC process was initiated. For a rolling grid more staff may be required to ensure that this QC process is time efficient. Another alternative is to utilise specialised 3C cables and boxes where all three channels are connected to a three channel box through a single connection. This would reduce the amount of equipment in the field and reduce the chance of errors occurring.

8.3.2 Processing

For this project FK-filtering was used to remove the ground-roll noise. An alternative method which uses downward continuation to project the data below the ground-roll noise has shown promise for ground roll removal on 2D data. This might be expected to produce similar results in 3D PS data and could be very useful in environments where large amounts of surface noise are generated.

In conventional P-wave processing, residual statics are usually calculated after the refraction statics correction has been applied. The residual statics correction provides secondary adjustment to the refraction statics solution. It would be interesting to trial the PS refraction and residual methods in this same way to see if an improved statics solution can be achieved.

For our latest 2D-PS datasets dynamic binning has been used to bin each sample of a trace into the required CCP locations. This is essential for multi-seam environments and will need to be developed for 3D-PS processing if optimal images are required in these environments.

In this investigation no migration has been applied. Migration is important for determining the nature and lateral location of faults and other structures. A number of different migration approaches should be tested on the PS data to ascertain which is most appropriate. Of particular interest is the equivalent-offset gathering and migration technique (Bancroft and Wang, 1994). This has the advantage that it produces hyperbolic high-density gathers to which standard P-wave processing algorithms can be applied. The azimuthal dependences identified in Chapter 7 will be introducing smearing into the all azimuthal images. A complete migration solution will need to account for such anisotropic effects

The processing sequence applied to the PS data in this trial has been presented as a basic approach to 3D-PS surveying and may not be the optimal approach. There are additional processing steps that could be considered for 3D-PS processing (e.g. 3D-PS trim statics, deconvolution etc.).

8.3.3 Interpretation

It is known that certain physical properties of the earth (e.g. Vp/Vs, Poisson's ratio, porosity) can influence P and S waves differently. Therefore, integrated P+PS attributes may give an improved characterisation of the geology. This has shown some application in the petroleum industry. At the coal-scale we have applied such analysis to 2D-PS data, where the resolution tends to be insufficient to achieve useful results. However, 3D-PS data has the potential to have higher resolution and by nature it is easier to observe cross-line variations with 3D data. Therefore, it may be possible to derive improved geological information from such integrated 3D P+PS attribute analysis.

The azimuthal analysis described in Chapter 7 has suggested interesting possibilities relating to fracture detection. Too confirm if the results observed are indeed meaningful the data should be re-examined after migration has been applied. If the azimuthal affects are related to diodic geology it may be possible to use an integrated P and PS inversion algorithm to delineate zones of high and low velocity (e.g. Chang and McMechan, 2009).

8.4 Conclusion

The overall objective of this project has been to investigate the feasibility of acquiring, processing and interpreting 3D-PS (converted-wave) data from coal targets. Prior to this study the majority of

the 3D converted-wave surveys conducted were designed to image deep petroleum scale targets. At the shallower coal-scale, PS seismic reflection surveys have been restricted to 2D geometries.

The results from this survey have clearly demonstrated that a 3D-PS dataset can be acquired and processed to generate a good quality stacked volume. The interpretation of the P and PS volumes indicates that the PS data makes an important contribution to the structural interpretation of the area, by supporting the P interpretation and providing additional information.

The PS data have exhibited significant azimuthal variation, which partially degrades the stacked volume if ignored. This variation is likely to be due to a combination of processing errors and geology. The geological aspect has the potential to provide extra information such as fracture detection.

This project has shown that 3D-PS surveying for coal targets has significant potential. Future research in the areas of lithological identification, azimuthal fracture detection and processing optimisation are likely to further increase this potential.

9 References

ALLEN S.J. 1980. Seismic Method. *Geophysics*. 45 (11), 1619-1633.

BANCROFT J.C.,WANG S., 1994, Converted-wave prestack migration and velocity analysis by equivalent offsets and CCP gathers. *CREWES Research Report*, **6 (28)**.

BERTEUSSEN K.A., LANGHAMMER J., ANDREASSEN K., SOGNNES H.I., HENNEBERG K., 1999, Multicomponent sea bottom data in gas hydrate exploration, *EAGE 61st Conference and Technical Exhibition – Expanded Abstracts*, **1,** 6-20

BRZOSTOWSKI M., ZHU X., ALTAN S., THOMSEN L., BARKVED O., ROSLAND B. 1999. 3D Converted-Wave Processing over the Valhall field. *SEG Expanded Abstracts*, **18**, 695-698

CHANG H., McMECHAN G. 2009. 3D 3-C full-wavefield elastic inversion for estimating anisotropic parameters: A feasibility study with synthetic data. *Geophysics* **74 (6)**, WWC159-WWC175.

CHERRY J.T., WATERS K.H. 1968. Shear wave recording using continuous signal methods: Part I – early development. *Geophysics,* **33 (2)**, 229-239.

CRAMPIN S., EVANS R., UCER B., DOYLE M., DAVIS J.P., YEGORKINA G.V., MILLER A. 1980. Observations of dilatancy-induced polarisation anomalies and earthquake prediction. *Nature*, **286**, 874-877.

CRAMPIN S., LOVWELL J. H. 1991. A decade of shear-wave splitting in the Earth's crust: What does it mean? What use can we make of it? And what should we do next? *Geophys J. Internat*, **107**, 387-407.

CRAMPIN S., 1997. Going APE: I - Modeling the inherent anisotropy of intact rock. *SEG Expanded Abstracts*, **16**, 952-955.

DUFOUR J., SQUIRES J., GOODWAY W. N., EDMUNDS A., SHOOK I. 2002. Integrated geological and geophysical interpretation case study, and Lamé rock parameter extractions using AVO analysis on the Blackfoot 3C-3D seismic data, southern Alberta, Canada. *Geophysics,* **67**, 27-37.

GAISER J.E, STRUDLEY A. 2005. Acquisition and application of multicomponent vector wavefields: are they practical? *First Break,* **23**, 61-67.

GALBRAITH M., 1994, Land 3-D survey design by computer, *Exploration Geophysics*, **25**, 71-77

GANDER W., GOLUB G.H., STREBEL R., 1994, Least-Squares Fitting of Circles and Ellipses, BIT Numerical Mathematics, Springer

GAROTTA R., GRANGER P.Y. 1988. Acquisition and processing of 3C x 3D data using converted waves. *SEG Expanded Abstracts*, **7**, 995-997.

GAROTTA R. 1999. Shear Waves from Acquisition to Interpretation. *Distinguished Instructor Series – Number 3*. Society of Exploration Geophysics, Tulsa.

GUY E.D. 2004. Evaluation of near-surface converted-mode seismic reflection imaging. *Electronic Journal of geotechnical Engineering,* **9 (D)**.

HANSON R., MACLEOD M., BELL C., THOMPSON C., SOMOD J. 1999. Multi-Component seismic interpretation: data integration issues, Alba field, North Sea. *SEG Expanded Abstracts,* **18**, 808-811

HATHERLEY P., POOLE G., MASON I., ZHOU B., BASSINGTHWAIGHTE, H. 1998. 3D seismic surveying for coal mine applications at Appin Colliery, NSW. *Exploration Geophysics*, **29 (4),** 407-409.

HEARN S.J. 2004. Shallow high-resolution converted-wave seismology for coal exploration. *Extended Abstracts, ASEG 17th Geophysical Conference and Exhibition, Sydney 2004.*

HEARN S., MEULENBROEK A. 2011. Ray-path concepts for converted-wave seismic refraction: in press *Exploration Geophysics* 2011.

HELBIG K., MESDAG C.S., 1982, The potential of shear-wave observations, *Geophysical Prospecting*, **30**, 413-431.

HOFFE B.H., STEWART R.R., BLAND H.C., GALLANT E.V., BERTRAM M.B. 1998. The Blackfoot high-resolution 3-C seismic survey: design and initial results. *SEG Expanded Abstracts*, **17**, 103-106**.**

HOFFMANN J., 2001, Illumination, resolution and imaging quality of PP- and PS-waves for survey planning, The Leading Edge, **20 (9)**, 1008-1014

LAMBOURNE A.N., EVANS B.J., HATHERLY P.J. 1989. Application of the 3D seismic surveying technique to coal seam imaging – case history from the Arckaringa and Sydney basins.

Exploration Geophysics, **20 (2)**, 137-141.

LI X., DAI H., MUELLER M.C., BARKVED O.I. 2001. Compensating for the effects of gas clouds on C-wave imaging: A case study from Valhall. *The Leading Edge*, **20**, 1022-1028.

LU H., MARGRAVE G.F. 1998. Reprocessing the Blackfoot 3C-3D seismic data. *CREWES Research Report*, **10 (31)**.

MACLEOD M., HANSON R., HADLEY M., REYNOLDS K., LUMLEY D., MCHUGO S., PROBERT T. 1999. The Alba field OBC seismic survey. *SEG Expanded Abstracts,* **18**, 725-727.

MEULENBROEK A., HEARN S. 2011. Analysis of converted-refractions for shear statics and near surface characterisation: in press *Exploration Geophysics* 2011.

OLOFSSON B., PROBERT T., KOMMEDAL J.H., BARKVED O.I. 2003. Azimuthal Anisotropy from the Valhall 4C 3D survey. *The Leading Edge*, **22**, 1228-1235.

PACKHAM G. H., EMERSON D. W. 1975. Upper Permian coal measures of Central Sydney basin, N.S.W – seismic data analysis and drilling results. *Bulletin of Australian Society of Exploration Geophysics*, **6(1)**, 4-13.

REITER L., 1970, An investigation into the time term method in refraction seismology, *Bulletin of the Seismological Society of America*, **60 (1)**, 1853-1854.

RUTTER H., HARMAN P. 1979. Seismic reflection techniques in coal exploration. *Bulletin of Australian Society of Exploration Geophysics,* **10 (3)**, 220-221.

SIMIN V., HARRISON M.P., LORENTZ G.A. 1996. Processing the Blackfoot 3C-3D seismic survey. *CREWES Research Report,* **8 (39)**.

STEWART R.R., GAISER J.E., BROWN J., LAWNTON D.C. 2002. Tutorial: Converted-wave seismic exploration: Methods. *Geophysics*, **67**, 1348 – 1363.

STRONG S. HEARN S., 2008, Multi-component seismic-resolution analysis using finite-difference acquisition modelling, *Exploration Geophysics*,, **39**, 189–197

SUTHERS B., HEARN S. 1997. Shear-wave splitting analysis of multi-offset coal VSPs in the Bowen Basin. *Exploration Geophysics*, **28**, 363-368.

TURNER B., HEARN S. 1995. Shear-wave splitting analysis using a single-source, dynamite VSP in the Otway Basin. *Exploration Geophysics*, **26**, 519-526.

VELSEIS. 2003. Final Report - #C10020: Converted-wave seismic reflection for improved resolution of coal structures. *ACARP Report*, **C10020**

VELSEIS. 2007. Final Report - #C13029: Integrated P/PS seismic imaging for improved geological characterisation of coal environments. ACARP Report, **C13029**

WHITE J.E., HEAPS S.N., LAWRENCE P.L. 1956. Seismic waves from a horizontal force. *Geophysics,* **21 (3),** 715-723.

WHITE J.E., SENGBUSH R.L. 1963. Shear waves from explosive sources. *Geophysics,* **28 (6)**, 1001-1019.

10 Glossary

This glossary contains explanations of technical terms and acronyms commonly used to describe multi-component seismic processing and interpretation.

2D	two-dimensional
3D	three-dimensional
3C	three-component; typically refers to the vertical and two orthogonal horizontal components of ground motion recorded by a 3-C geophone
AGC	automatic gain control; data-dependent scaling designed to normalise trace amplitude within a running time window
anisotropy	variation of seismic velocity depending on the direction in which it is measured; a sequence of sedimentary bedding produces polar anisotropy (where seismic velocities are symmetric about axis perpendicular to the bedding); non-horizontal fracturing and microcracks produces azimuthal anisotropy
angle of incidence	the angle (with respect to the normal) at which seismic energy arrives at a geological boundary
bandpass filtering	attenuation of seismic energy outside of a user-defined frequency bandwidth
binning	the process by which all traces sharing the same sub-surface reflection point are grouped together; typically referred to as CMP binning for conventional P data, and CCP binning for PS data
CCP stacking	the summation of all traces within a CCP gather
CMP stacking	the summation of all traces within a CMP gather
common conversion point (CCP) gather	a collection of (usually horizontal component) seismic traces sharing the same sub-surface P-to-S conversion point; the location of the wavefield conversion point is a function of Vp/Vs and the depth of the boundary at which the conversion occurs
common midpoint (CMP) gather	the set of (usually vertical component) seismic traces that share the same midpoint between their sources and receivers

common receiver gather (CRG)	a collection of seismic traces recorded at the same geophone (receiver) location, generated by sources at a variety of locations
converted waves	seismic waves that travel down to a geological boundary as a P wave, get partially converted to S energy at the boundary, and then travel back to the surface as an S wave; also referred to as PS waves
CRG stack	the resultant seismic section produced by summing all traces within each CRG, and displaying the summed traces in receiver-location order
crossline component	seismic energy recorded using a geophone that measures the horizontal component of ground motion perpendicular to the line of recording
diodic illumination	variations in a PS seismic image with ray azimuth due to ray-path effects.
dominant frequency	the predominant frequency of a seismic dataset determined by measuring the time between successive peaks or troughs of the recorded seismic pulse, and taking the reciprocal
dominant wavelength	the seismic wavelength associated with the dominant frequency; for P waves, equivalent to Vp divided by the dominant frequency; for S waves a more complicated expression involving both Vp and Vs, and P- and S-wave dominant frequencies is required
fk filtering	removal of energy from data that has been transformed into the frequency-wavenumber domain; used to remove slow coherent noise
frequency	the repetition rate of a periodic waveform, measured in ‘cycles per second’ or Hertz (Hz)
frequency bandwidth	range of frequencies over which the recorded seismic signal has significant power
gamma	See Vp/Vs
geophone	the recording device or receiver used to transform seismic energy into an electrical voltage for input into the seismic recording system; a single vertically-oriented geophone is used for conventional seismic acquisition; three mutually orthogonal geophones are used when recording 3-C data
groundroll	a type of seismic wave that travels near the surface of the ground; characterised by relatively low velocity, low frequency and high amplitude; seen as a steeply dipping, linear event on a seismic shot record

inline component	horizontal component of ground motion parallel to the line of recording
Lithological interpretation	used here to describe efforts to extract more detailed geological character in terms of lithology, fluids and fractures etc
magnitude spectrum	amplitude of seismic recording as a function of frequency
Multi-component recording	seismic recording that measures both the vertical and horizontal components of ground motion at the receiver; also referred to as 3-C recording
mute	elimination of unwanted energy from seismic traces; typically used over certain time intervals to remove groundroll or noise bursts out of the final stack
normal moveout (NMO)	the variation of the arrival time of reflection energy with offset; NMO corrections compensate for this variation in traveltime so that reflection energy from each geological boundary is properly aligned prior to stacking; for horizontal reflectors, P-wave NMO can be described as hyperbolic; the NMO for PS-waves is always non-hyperbolic
offset	the distance from the source point to the receiver location
P waves	longitudinal or compressional seismic waves; characterised by particle motion in the direction of travel; acquired using conventional (single component) seismic acquisition surveys
radial component	horizontal component of ground motion parallel to the source to receiver direction; mathematically derived from the recorded horizontal components; generally only used for 3D data; equivalent to the 2D inline component
residual static corrections	corrective time shifts applied to the data to compensate for remnant statics associated with incomplete weathering-static corrections
resolution	the ability to separate two features which are very close together
resolution limit	for discrete seismic reflectors, the minimum separation so that one can ascertain that more than one interface is involved; the commonly used Rayleigh resolution limit is defined as one quarter the dominant wavelength; the Widess limit is defined as one eighth the dominant wavelength
S waves	transverse or shear seismic waves; characterised by particle motion perpendicular to the direction of travel; acquired using multi-component (3-C) seismic acquisition

seismic waves	sound waves that propagate through the earth
seismic modelling	generation of a synthetic seismic record based on an assumed earth model
seismic reflection	a geophysical method to image the sub-surface using artificially-generated sound waves; typically the arrival times of various seismic waves are used to map sub-surface structure
seismic source	a device that releases energy or seismic waves into the ground; typical coal-seismic sources include small dynamite explosions, MiniSOSIE and Vibroseis
seismic velocity	the propagation rate of a seismic wave through a particular material
source record	a collection of seismic traces recorded from the release of seismic energy at a single source location; also called shot record
signal-to-noise ratio (S/N)	the ratio of desired signal to all other recorded energy (noise) in a seismic recording; difficult to determine in practice
single-component recording	conventional seismic acquisition that records only the vertical component of ground motion at the receiver
spherical divergence correction	a scaling correction to compensate for decrease in wave strength with distance as a result of geometric spreading
stacking	process by which a set of seismic traces are summed
static corrections	corrective time shifts applied to seismic data to compensate for the effects of variations in elevation, weathering thickness, weathering velocity or reference to datum; the objective is to determine the arrival times which would have been observed if all measurements had been made on a flat plane with no weathering or low-velocity material present
structural interpretation	the mapping of geological interfaces and discontinuities (such as faults)
transverse component	horizontal component of ground motion perpendicular to the source to receiver direction; mathematically derived from the recorded horizontal components; generally only used for 3D data; equivalent to the 2D crossline component
trim statics	corrective time shifts applied to NMO-corrected CMP or CCP gathers prior to stacking; designed to optimally align flattened reflection events

TWT	two-way traveltime; refers to the time it takes for seismic energy to travel from the seismic source, down to a reflector, and back to the surface receiver
vector processing	simultaneous use of two or more components of multi-component seismic data to separate P and S energy
velocity analysis	calculation of a velocity that will accurately compensate for the effects of NMO; typically involves flattening reflection events in a CMP or CCP gather
vertical component	the seismic energy recorded using a geophone that measures the vertical component of ground motion
Vp	P-wave seismic velocity
Vs	S-wave seismic velocity
Vp/Vs	ratio of P-wave to S-wave seismic velocity; also referred to as gamma (γ); Poisson's Ratio can be derived from gamma
wavelength	the distance (in metres) between similar points on successive cycles of a seismic wave, measured perpendicular to the wave front; often represented by the symbol λ
wavenumber	spatial frequency i.e. waves per unit distance; often representated by the symbol k

11 Appendix

11.1 Envirovibe Energy Source

Velseis Pty Ltd has used 'Envirovibe' Vibroseis sources since January 2008, for coal, coal seam gas (CSG), and shallow petroleum work. These are very compact units, each with a total mass of about 17,000 lbs. They are mounted on articulated buggies for high manoeuvrability and they have a small circular baseplate, with minimal environmental footprint. Noise levels are much lower than those associated with larger vibrators.

Envirovibe electronics are SSC Force-Two, which employ latest generation phase and force control and a complete suite of sweep options.

Transport of these units is simple and economical, with two units being transportable on one low loader, or three on a B-double.

A primary overseas application for these units has been in situations where conventional, larger vibrators cannot be used for environmental or access reasons. It has been found that despite having a peak force and a hold down mass about one-third that of conventional units, the Envirovibe has consistently performed competitively in the CSG and shallow petroleum arena. Where deeper targets are involved and access for larger Vibrators is not possible, up to four Envirovibes have been used in order to ensure penetration and to provide data previously unobtainable due to access being denied to large vibrators.

In January 2008 the Envirovibe performance was tested on a prospect having CSG-depth coal seams as well as a petroleum target. The raw field records were of excellent quality with well-defined reflectors. The first-arrival events are very well defined by Vibroseis standards. This may partially relate to the compact base-plate design. The quality of these first-arrivals is critical for the calculation of refraction statics.

11.2 S-Wave Residual Receiver-Static Corrections

Our S-wave residual statics algorithm was introduced in ACARP # C13029 and is presented here for convenience. (The term “residual statics” is derived from a conceptually similar P-wave technique.) Near-surface lateral velocity variations and topographical changes cause time

anomalies in seismic reflection events that can be approximated as surface-consistent static time shifts. Consider a particular trace at source = i, receiver = j, CCP = k, and offset = l. The total static time shift of this trace, δt_{ijkl}, can be described by the surface-consistent model:

$$\delta t_{ijkl} \approx \delta t_i + \delta t_j + \delta t_k + \delta t_l , \qquad \text{(A-1)}$$

where δt_i is the time anomaly associated with the near-surface at the source, δt_j is the time anomaly associated with the near-surface at the receiver, δt_k is the time anomaly associated with the CCP (i.e. a time anomaly associated with structure along the line), and δt_l is the time anomaly associated with the offset (i.e. a time anomaly associated with the normal-moveout of the reflection event). The inequality suggests that the observed δt_{ijkl} will usually be subject to error.

Equation (A-1) can be re-written in matrix form as:

$$\boldsymbol{t} \approx \boldsymbol{A}\boldsymbol{s} \quad \text{or}$$

$$\begin{pmatrix} \delta t_{1111} \\ \delta t_{2111} \\ \vdots \\ \delta t_{1211} \\ \vdots \\ \delta t_{1111} \\ \vdots \end{pmatrix} \approx \begin{pmatrix} 1 & 0 & 0 & \cdots & 1 & 0 & 0 & \cdots & 1 & 0 & 0 & \cdots & 1 & 0 & 0 & \cdots \\ 0 & 1 & 0 & \cdots & 1 & 0 & 0 & \cdots & 1 & 0 & 0 & \cdots & 1 & 0 & 0 & \cdots \\ \vdots & \vdots & \vdots & \vdots & \vdots & \vdots & \vdots & \vdots & \vdots & \vdots & \vdots & \vdots & \vdots & \vdots & \vdots & \vdots \\ 1 & 0 & 0 & \cdots & 0 & 1 & 0 & \cdots & 1 & 0 & 0 & \cdots & 1 & 0 & 0 & \cdots \\ \vdots & \vdots & \vdots & \vdots & \vdots & \vdots & \vdots & \vdots & \vdots & \vdots & \vdots & \vdots & \vdots & \vdots & \vdots & \vdots \\ 1 & 0 & 0 & \cdots & 0 & 0 & 1 & \cdots & 1 & 0 & 0 & \cdots & 1 & 0 & 0 & \cdots \\ \vdots & \vdots & \vdots & \vdots & \vdots & \vdots & \vdots & \vdots & \vdots & \vdots & \vdots & \vdots & \vdots & \vdots & \vdots & \vdots \end{pmatrix} \begin{matrix} \delta t_{SRC1} \\ \delta t_{SRC3} \\ \delta t_{SRC3} \\ \vdots \\ \delta t_{REC1} \\ \delta t_{REC2} \\ \delta t_{REC3} \\ \vdots \\ \delta t_{CCP1} \\ \delta t_{CCP2} \\ \delta t_{CCP3} \\ \vdots \\ \delta t_{OFF1} \\ \delta t_{OFF1} \\ \delta t_{OFF1} \\ \vdots \end{matrix} \qquad \text{(A-2)}$$

Here, **t** is the vector of total observed time shifts for each trace in the seismic dataset, and **s** is the vector of static shifts associated with individual sources, receivers, CCPs and offsets. Provided the above set of linear equations is over-determined (i.e. there are more observations in **t** than unknowns in **s**), the individual timing anomalies associated with the sources, receivers, CCPs and offsets can be solved for in a least-squares sense. In practice, a least-squares technique such as, singular value decomposition (SVD) is used to solve for the unknown vector s in equation (A-2).

(Care must be taken to ensure the system of equations is over-determined since SVD will still yield a solution for an underdetermined set of equations that may or may not be physically meaningful.) Note that in the case of computing S-wave receiver static corrections for converted-wave seismic data, we assume that $\delta t_{SRC1} = \delta t_{SRC2} = \ldots = \delta t_{SRCN} = 0$ (i.e. $\delta t_i = 0$ for all sources), since the P-wave source static corrections can be computed independently from the P-wave data and applied prior to computing the S-wave receiver statics. This reduces the number of unknowns in equation (A-2), and hence reduces the non-uniqueness of the solution. Any variations in the observed time shifts associated with structure and normal moveout (and error in the source static corrections) will dominate the δt_k and δt_l terms when we solve equation A-2. The desired S-wave receiver static correction is derived from the recovered receiver term δt_j.

In practice, our S-wave statics method determines the observed time shifts for each trace by picking the two-way traveltime (TWT) for a selected PS reflection event on every possible trace on every common-offset receiver section, and computing the difference between this TWT and some reference time. This approach to measuring δt_{ijkl} takes advantage of the fact that we expect very strong P-to-S conversion from the top of a coal seam, and can therefore consistently identify PS reflection events on raw common-offset receiver sections.

11.3 Alternative Static-Correction Methods

We have shown that the residual-static method may produce errors when the weathering conditions are highly variable. As such, in this investigation we have investigated some alternative approaches for deriving the receiver static corrections.

11.3.1 Robust Statistical Method

The so called robust statistical method utilises statistical averaging to separate the short-wavelength S-wave receiver statics. For this approach the P-wave source statics are applied to the data and, as with the residual method described above, the timing of a dominant event is picked on limited-offset receiver stacks. That is, the dataset used for the robust statistical method is the same as that used for the residual approach. Thus, this method can be tested alongside the residual method with a minimal amount of extra effort.

Figures 11.1 through 11.4 present a synthetic representation of each stage of the robust statistical method. As discussed in the previous section the time of each horizon pick is a combination of the

receiver static, a velocity (or offset) term and a structural term (assuming source corrections have already been applied). The aim of this approach is to separate the receiver static term, in particular, the short-wavelength component in order to improve the final stacked section.

The first step in the robust statistical approach is to remove the bulk offset term. This is achieved by subtracting the average for each offset group (Figure 11.2). The remaining effects should then be due to the structural and receiver terms. At this stage it may be difficult to separate the structural terms from the receiver terms for the same reasons that the residual method had errors (i.e. complex near surface environment and geometry issues associated with the asymmetric reflection of PS data). However, if the long-wavelength component is removed (Figure 11.3) the short-wavelength structural and receiver terms can be separated. The receiver term is extracted by sorting the data by receiver location. Then for each location a median filter is applied to get the average (Figure 11.4).

The short-wavelength receiver-static corrections acquired from the robust statistical approach can improve the reflector continuity on the final stacked images. However, long-wavelength errors will still remain in the structural interpretation.

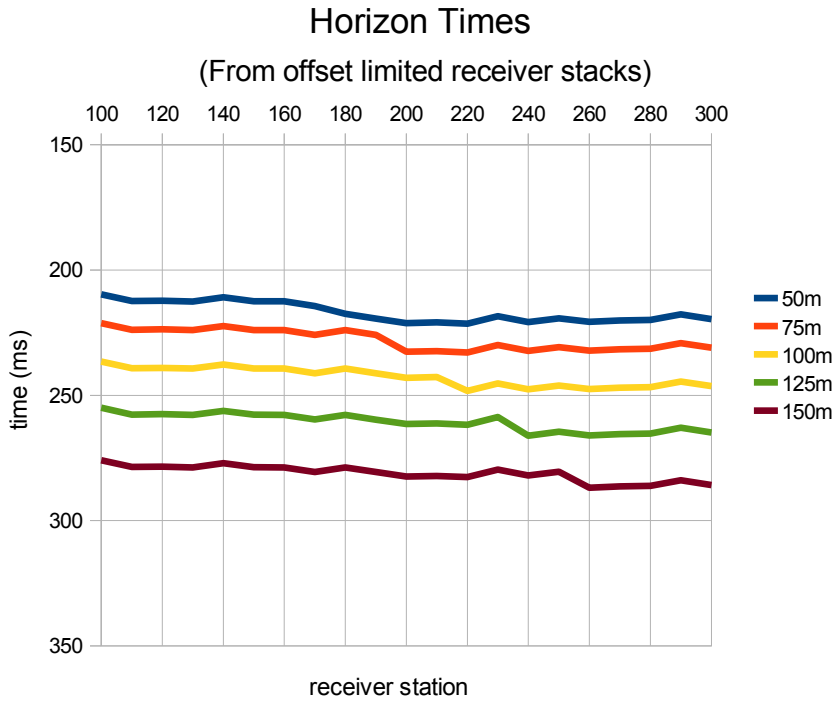

Figure 11.1: Horizon picks from limited-offset receiver picks. These can be used in either the residual-static or the robust statistical methods.

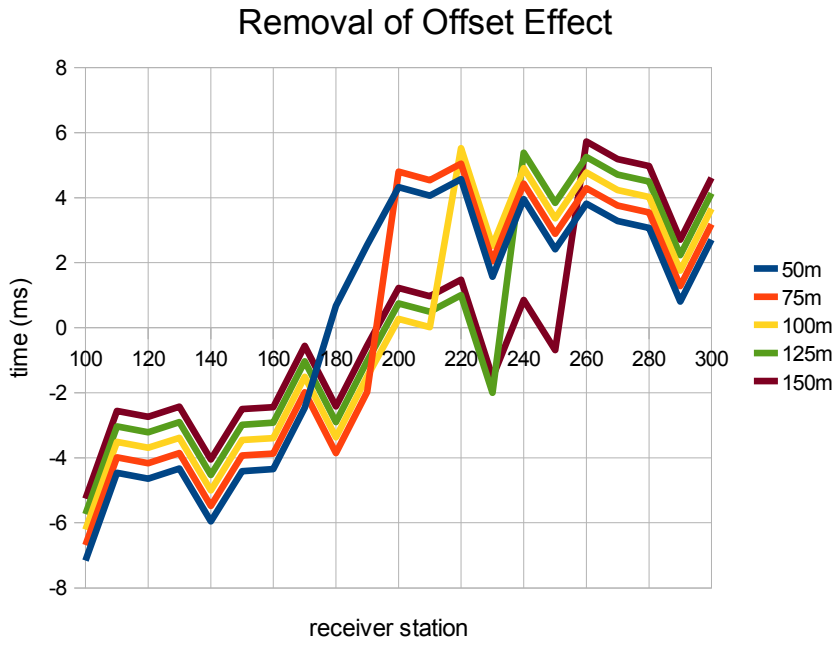

Figure 11.2: Horizon picks from Figure 11.1 after removal of the offset term

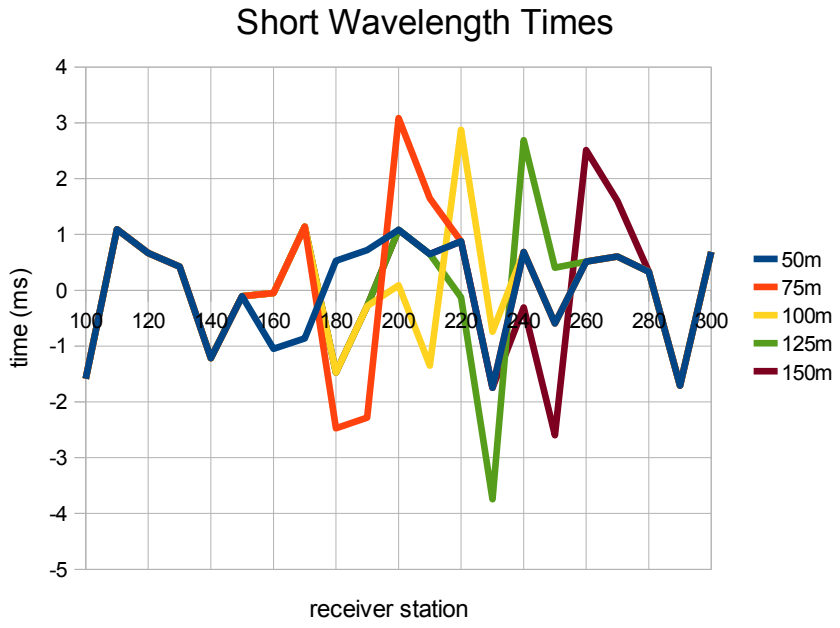

Figure 11.3: Short wavelength component of the horizon times in Figure 11.2

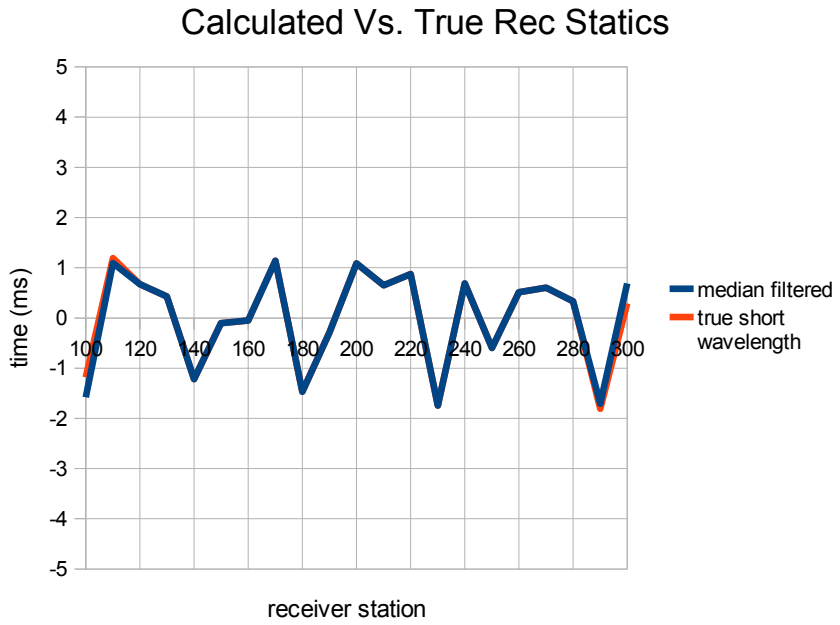

Figure 11.4: Comparison of the true short-wavelength receiver static and the curve generated by applying a median filter to the points in Figure 11.3.

11.3.2 Time-term analysis of PPS refractions

For conventional P-wave surveys one standard technique for calculating source and receiver statics utilises the PPP refraction wave. The advantage of this is that it is the first arrival on a seismic record and is primarily dependant on the weathering layer. It is therefore unaffected by deeper geological variations.

For converted waves the equivalent concept is to examine the PPS refraction, where the energy travels from the source and along the base of weathering as a P-wave, and then converts to an S head wave and travels back through the weathering layer to a receiver at the surface (Figure 11.5). This has the advantage of traversing the weathering layer at the source and receiver with the same wave types as the PS reflection, therefore providing a good indication of the surface related statics. The disadvantage with the PPS refraction is that it is usually quite weak and often exhibits significant lateral variation in time. This results in it being difficult to pick. In 2D coal-scale surveys the number of picks that can be selected is generally not enough to give a stable solution from any refraction method. However, the higher fold of 3D surveys suggests that there may be some potential for using refraction based methods.

In this project we have examined one such PPS refraction technique, where the refraction picks

have been analysed with the time-term algorithm. The time for each refraction pick is assumed to be a linear combination of the time to traverse the weathering layer at the source (t_s), the receiver (t_r)and the time to travel from the source to the receiver (Figure 11.5). This can be written as,

$$t \approx t_s + t_r + \sum_{k=0}^{n} \frac{d_k}{Vp_k} \qquad \text{(A-3)}$$

where the path between the source and the receiver is divided into a number of bins of constant velocity (Vp) and d is the distance travelled through each bin. This method assumes that the rays are near vertical and will only give appropriate Vp values when the weathering layer velocity is much less than the sub-weathering layer.

Similar to the residual method, the full set of time-term equations (A-3) can be written in matrix form,

$\boldsymbol{t} \approx \boldsymbol{A}\,\boldsymbol{s}$ or

$$\begin{pmatrix} t_{11} \\ t_{21} \\ \vdots \\ t_{12} \\ \vdots \end{pmatrix} \approx \begin{pmatrix} 1 & 0 & 0 & \cdots & 1 & 0 & 0 & \cdots & d1_{11} & d2_{11} & d3_{11} & \cdots \\ 0 & 1 & 0 & \cdots & 1 & 0 & 0 & \cdots & d1_{21} & d2_{21} & d3_{21} & \cdots \\ \vdots & \vdots & \vdots & \vdots & \vdots & \vdots & \vdots & \vdots & \vdots & \vdots & \vdots & \vdots \\ 1 & 0 & 0 & \cdots & 0 & 1 & 0 & \cdots & d1_{12} & d2_{12} & d3_{12} & \cdots \\ \vdots & \vdots & \vdots & \vdots & \vdots & \vdots & \vdots & \vdots & \vdots & \vdots & \vdots & \vdots \end{pmatrix} \begin{pmatrix} t_{SRC1} \\ t_{SRC3} \\ t_{SRC3} \\ \vdots \\ t_{REC1} \\ t_{REC2} \\ t_{REC3} \\ \vdots \\ Vp_1^{-1} \\ Vp_2^{-1} \\ Vp_3^{-1} \\ \vdots \end{pmatrix} . \qquad \text{(A-4)}$$

This can be inverted to separate the individual components. For this project the singular-value decomposition (SVD) algorithm has been used.

It is important to note that, when using the SVD algorithm data must be well conditioned. That is if the distances are given in meters, these may dominate the **A** matrix and skew the solution. We have found that defining the distances in km and the velocities in km/s gives more balanced results. We have examined various sizes for the velocity bins and have found that, while there is little difference for this area, 60mX60m bins appeared to produce the best results.

Inversion of this type of problem can often result in non-unique solutions. In particular, we have found that the average level of the derived source and receiver terms may be poorly controlled. To reduce this we have implemented extra boundary conditions to the SVD algorithm that ensure that the average source term for the PPP and PPS refractions are the same, and that these are also the same as the average of the PPP receiver terms for a surface source. The velocity terms have also been restricted to a range between 1km/s and 5km/s. These conditions have significantly improved the reliability of this method.

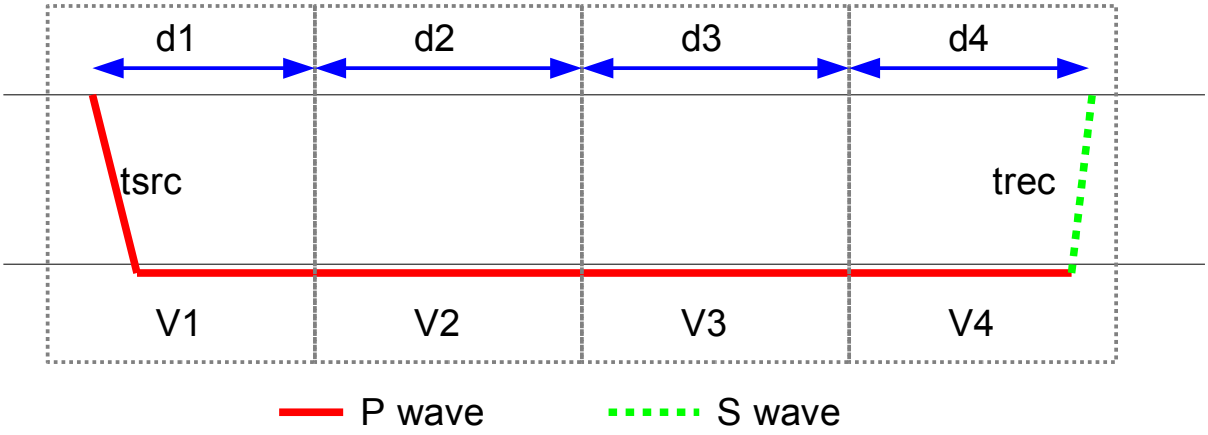

Figure 11.5: A 2D representation of the PPS refraction wave. The source and receiver components of the total time are indicated by the downward and upward travelling waves. The offset component has been divided into 4 bins of constant velocity and the approximate horizontal distance travelled in each bin is shown by the blue lines. In this project we have implemented a 3D version of the algorithm.